TECHNISCHE UNIVERSITÄT WIEN
Vienna University of Technology

DIPLOMARBEIT

Quantum memory and quantum amnesia -

coherent exchange of excitations between a NV^- spin ensemble and a superconducting resonator

ausgeführt am Atominstitut
der Technischen Universität Wien

unter der Anleitung von
Univ.Prof. Dipl.-Ing. Dr. techn. Hannes-Jörg Schmiedmayer
Dr. Johannes Majer

durch
Andreas Maier
Darwingasse 26
1020 Wien

Wien, Juni 2013 Andreas Maier

To whom it may concern

Zusammenfassung

Die vorliegende Arbeit beschäftigt sich mit der Möglichkeit Quanteninformation in einem Ensemble von Stickstoff Fehlstellen (NV^-) Zentren in Diamant zu speichern. Solche Quantenspeicher aus Ensembles mikroskopischer Objekte sind Teil eines Konzeptes hybrider Quantensysteme, das im Kontext der sogenannten circuit QED entwickelt wurde. Supraleitende Mikrowellenresonatoren in solchen hybriden Systemen sorgen für die Übertragung von Quanteninformation. Vorraussetzung dafür ist, dass die Kopplung des Ensembles von NV^- Zentren an das elektromagnetische Feld des Resonators stark genug ist, d.h. größer ist als die jeweiligen Zerfallsraten der beteiligten Systeme. Zwei unterschiedliche Typen von Resonatoren kamen in den Experimenten zur Anwendung, einerseits bewährte koplanare Wellenleiter-Resonatoren und andererseits für uns neue, diskrete Schwingkreise. Die Verwendung diskreter Schwingkreise war unter anderem dadurch motiviert, dass ihr Modenvolumen kleiner als das der Wellenleiter-Resonatoren gemacht werden kann, was die Möglichkeit eröffnet, an weniger NV^- Zentren zu koppeln ohne Verluste in der effektiven Kopplungsstärke hinnehmen zu müssen. Die ersten Versuche dahingehend sind Teil dieser Arbeit, wobei es uns unseres Wissens zum ersten mal gelungen ist, eine starke Kopplung zwischen einem diskreten Schwingkreis und einem Ensemble von NV^- Zentren zu erreichen.

Weitere wichtige Aspekte der Arbeit sind spektroskopische und zeitabhängige Vermessungen der Phänomene der starken Kopplung, also die Modenteilung einerseits und die Rabi-Oszillationen andererseits. Experimentell stellte sich heraus, dass, obwohl im Bereich der starken Kopplung, die Verlustmechanismen ebenfalls relativ stark waren. Die Vermutung, dass die wesentlichen Verluste von der inhomogenen Verbreiterung des Ensembles herrühren, hat sich in der Analyse der spektroskopischen als auch der zeitabhängigen Messungen bestätigt. Dafür wurden verschiedene Modelle bemüht, die sich im Wesentlichen in der Komplexität der Beschreibung der Verteilung des Ensembles von NV^- Zentren unterschieden.

Abstract

The present work deals with the possibility to store quantum information in an ensemble of nitrogen-vacancy (NV^-) centres in diamond. Such a quantum memory is part of a concept of hybrid quantum systems that has been developed in the context of circuit QED. Superconducting microwave resonators ensure that the quantum information is transferred between the components of such a hybrid systems. In order to do so, the ensemble of NV^- centres has to be coupled strong enough to the electromagnetic field of the resonator, i.e. that the coupling strength must exceed the loss rates of the involved systems. Two different types of resonators have been used, already approved coplanar transmission line (TL) resonators on the one hand and lumped element resonators (LER), that were new for us, on the other hand. The use of LERs is based, amongst others, on the fact, that their mode volume can be reduced to dimensions much smaller than those of TL resonators. This opens up the possibility to couple to less NV^- centres without weakening the effective coupling strength. To our knowledge the first strong coupling experiment with a LER and an ensemble of NV^- centres has been carried out. Other important aspects of this work concern the measuring of strong coupling phenomena spectroscopically (mode splitting) as well as in time domain (Rabi oscillations). Experimentally we found, although we have reached the strong coupling regime, that the losses have been remarkable high.

The analysis of the measurements in frequency and time domain confirmed our presumption, that the main losses were caused by inhomogeneous broadening of the NV^- ensemble. We used different models for the analysis of the data, whereupon they differed basically in the level of complexity with which the distribution of a NV^- ensemble was described.

Contents

List of Figures

List of Tables

1. Introduction

The first electronic digital computers from the 1940s were the size of a large room. While the size of the computers continuously shrunk with time the computer power increased more and more. In 1965 Gordon Moore predicted that the number of transistors in a computer and thereby the computer power itself will double roughly every two years [Moo65]. Although this trend was predicted *for at least ten years* it has continued now for more than 50 years and is known as *Moore's law*. During these decades the sizes of the electronic devices have become smaller and smaller and in meantime approaching dimensions where quantum effects begin to interfere in their functioning [Nie07].

Quantum computation Amongst others this future scenario brought scientists at the beginning of the 1980s to investigate the fundamental physical limits of classical computation. In 1982 Richard Feynman has pointed out that with classical computers the simulation of a quantum mechanical system would not be possible. He postulated, that essential difficulties that classical computation implicates and that only allows the imitation of quantum mechanics, would be overcome by the use of a new kind of computer that is based on the principles of quantum mechanics, a so-called quantum computer [Fey82]. Three years later David Deutsch suggested in [Deu85] that quantum computers have in principle computational power exceeding those of classical computers.
One might think that the challenge of quantum computation lies mostly in the construction of a quantum mechanical system that can act as a quantum computer. However, in order that a quantum computer can solve problems more efficiently than a classical computer appropriate quantum algorithms, that make use of truly quantum aspects of quantum mechanics, are necessary but very hard to design.

Compared to the 1940s, today's computational centres are still filling rooms or even buildings but instead of a single computer they consist of several thousands of interconnected computers in order to allow amongst others classical parallel computation.
In [Deu92] a first quantum algorithm for certain classes of problems was published that was based on *quantum parallelism* (refers to a key feature of quantum physics namely the ability of a quantum system to exist in multiple states at the same time: quantum superposition), a term that was coined by David Deutsch, so as to distinguish it from classical parallel computation, and that in principle could solve the problems in exponentially less time than any classical deterministic computation.

Qubit In the concept of classical computation the basic unit of information is the *bit*. The quantum mechanical analogue in the idea of quantum computation is the quantum bit (a so-called qubit). A classical bit can either have the value 0 or 1 while the corresponding states for a qubit are $|0\rangle$ and $|1\rangle$. The crucial difference between a bit and a qubit is that a qubit can be in any superposition of the two states. However, a measurement, according to fundamental postulates of quantum mechanics, leads to a collapse of the superposition state in either $|0\rangle$ or $|1\rangle$ with appropriate probabilities. Therefore the information about the state of a qubit that can be obtained with a single measurement is one bit (0 or 1). Hence the power of quantum computation is based on the information that is represented by a qubit *that is not measured*! This kind of extra but *hidden information* is, what makes quantum information processing so complex but also so powerful [Nie07].
A qubit is basically a quantum mechanical two-level system. The minimal requirements for such a quantum system to be a quantum computer have been proposed by David DiVincenzo in [DiV96]. The requirements are very challenging for a quantum mechanical system and some of them even opposing each other. In order to obtain long coherence times the qubits must be to a high degree decoupled from any environment, however, to perform quantum computation the qubits have to be inter-coupled and for the write, read-out and control processes they have to be coupled strong enough to an external apparatus.

In the past decades physicists studied the quantum mechanical properties of a wealth of physical systems that in principle could be used for implementing a quantum computer, including atoms [Mon02], liquids [Cor00], and solids such as superconductors [Mar04], semiconductors [Los98][Han08] and ion-doped insulators [Ber07].

Cavity QED Fundamental studies with respect to the quantum mechanics of light (electromagnetic radiation) matter interaction have been carried out in the field of cavity *quantum electrodynamics* (QED), whereupon *cavity* refers to an optical or microwave resonator and QED implies the interaction of some matter (usually atomic) with the electromagnetic field (photons) inside the cavity. While the photons are confined in the cavity the atom is basically falling through it, allowing the interaction to take place.
The finite volume of the cavity, defined by the mirrors, provides the quantization of the electromagnetic field that appears in a discrete set of modes [Ber82]. In addition, the cavity insulates the atom-photon system from decohering influences from its environment, allowing it to maintain quantum coherence over an important time scales [Mab02].
Furthermore, the size of the cavity determines the maximum photon wave length that can be confined, thus it acts as a filter that suppresses all modes except one. But that is not all: the cavity provides also a solution for the general problem that the interaction between a single atom and a single photon in free space would be too small to be observed. The confinement of a photon in a cavity leads on the one hand to a small mode volume which in turn increases the energy density and on the other hand gives the photon many chances to interact with the atom since it is reflected by the mirrors many times. These properties of an electromagnetic cavity enhances the effective interaction strength [Sch07].
Finally the coupling regime depends on the relation of the coupling strength to the two main loss channels: on the one hand the leakage of photons through one of the mirrors and on the other hand spontaneous emission from the atom into modes other than the cavity. The regime of strong coupling is reached when the coupling strength exceeds the loss rates of both the atom and the cavity, otherwise the regime is called weak coupling. Strong coupling provides a regime where coherent exchange of a single excitation between

the atom and the cavity becomes possible. Having access to the strong coupling regime therefore is a necessary requirement for the implementation of quantum computation [Mil05]. Since the matter in cavity QED mainly consists of a single atom or rather a single atomic dipole moment $\vec{d}$ that is coupled to the cavity field $\vec{E}$ by the dipol interaction $\vec{d} \cdot \vec{E}$, the strong coupling regime is usually hard to reach.

Circuit QED In [Bla04] a new concept was introduced that opened new possibilities for studying the strong coupling regime of light matter interaction: circuit QED. The idea of circuit QED is to replace the microscopic natural atoms used in cavity QED by macroscopic artificial atoms made of superconducting quantum circuits. The toolbox of superconducting circuit elements contains basically capacitors, inductors and the Josephson element [Dev04]. The Josephson junction allows the engineering of non-linear behaving circuits which is a crucial requirement in order to fabricate superconducting two-level systems that can represent a qubit. The *cavity* in circuit QED is a one-dimensional superconducting on-chip transmission line resonator made of inductors and capacitors.
The superconducting qubits can be well integrated in the chip architecture (quantum integrated circuits), that means they do not move around and do not have to be trapped. Therefore they are less decoupled from their environment than falling atoms in a three-dimensional cavity. As a consequence the coherence time of a superconducting qubit is usually much shorter than that of a single natural and well isolated atom. But as future prospects of superconducting qubits depend strongly on the coherence time of Josephson junctions great efforts are being made to improve their isolation from their environment [Pai11].
Due to the use of superconducting material in circuit QED that is necessary for the operation of Josephson elements and to keep dissipative losses as low as possible, the circuits have to be operated at cryogenic temperature. The concept of circuit QED aims mainly on achieving the strong coupling regime: the employment of a one-dimensional cavity leads to a reduced mode volume compared to a three-dimensional cavity and as a consequence increases the energy per photon whereas the usage of superconducting artificial atoms lead to a large effective dipole moment (or rather electromagnetic cross-section)

that can exceed the single dipol moment of a natural atom on the orders of four magnitudes [Wal04]. Both steps lead to an enhancement of the coupling strength and facilitate essentially the achievement of the strong coupling regime in circuit QED.

Hybrid quantum systems As already mentioned the requirements for a quantum mechanical system to be used as a quantum computer are quite challenging and even opposing in some aspects. The coherence times of superconducting qubits are still not competitive with those e.g. of single trapped ions [Roo04]. In [Rab06] the concept of a *hybrid* quantum circuit is proposed that aims at the combination of the relative advantages of various implementations of quantum systems. That basically means to make use of the strong coupling of superconducting qubits to the electromagnetic field (with moderate coherence times) on the one hand and of the long coherence times of microscopic quantum systems (with weak coupling) on the other hand. Therefore the former is suitable for the implementation of quantum gates and for readout processes [Dev04] whereas an ensemble of the latter is a promising candidate for performing quantum memory tasks. An ensemble of N microscopic quantum entities (ensemble qubit) enhance the single coupling strength by the factor $\sqrt{N}$ and therefore allows to reach the required strong coupling regime if the size of the ensemble is adequate.
The resonator in such a hybrid system can be used as a *quantum bus* between the ensemble and the superconducting qubit.

Organisation of the thesis Chapter 2 introduces the different kinds of superconducting resonators that were used in the experiments that are covered in this thesis. Chapter 3 is concerned with important properties of a single spin system in a diamond crystal on the one hand and the behaviour of an ensemble of such spin entities in an external magnetic field on the other hand. In chapter 4 a theoretical description of the coupling of the spin ensemble to the electromagnetic field of a resonator is given. Chapter 5 contains the whole experimental part. Firstly spectroscopic measurements are presented, including the effects of external magnetic fields on the resonator properties, strong coupling experiments

and the influence of the probing power on the mode splitting. The second part of this chapter refers to measurements in time domain. Coherent exchange of excitations between the resonator and the spin-system are shown. Chapter 6 lists the different approaches we have used to model the data from the coupling experiments in time domain. The results are evaluated in chapter 7.

2. Superconducting microwave resonators

Electromagnetic resonators or rather cavities facilitate the study of interaction between light and matter due to their properties to produce very large electromagnetic fields in a narrow band of frequencies and in a small spatial volume. Resonators are filters that can be used to block all except for a narrow band of requested frequencies. A narrow resonance linewidth indicates a good confinement of the photon and a long decay time. In other words, the resonator traps the photon in a compact mode volume by the mechanism of high internal reflections. As a consequence, photons of the specific (resonant) frequencies of light have several chances to interact with the matter before they leak out of the resonator. This kind of amplification together with the facts that the more compact the mode volume the stronger the photon field and therefore the stronger the coupling strength, allows to study the interaction of light and matter on the single photon level [Mil05].

The task of a superconducting microwave resonator within the hybrid approach in circuit QED is the transfer of quantum information between the superconducting qubit (processor) and the ensemble of microscopic quantum systems (memory). The carriers of quantum information are microwave photons. In [Maj07] they report on the successful implementation of such a „quantum bus“ that can be used to couple two superconducting qubits that are beyond the reach of the local interaction.

The resonator itself, provided that it behaves linearly, does not comply with the DiVincenzo criteria and therefore is not suited to be used as a qubit.

In order to be able to carry out its role as a quantum bus, a coherent exchange of quantum information with the ensemble of microscopic quantum systems (NV^- centres) is

necessary. With respect to the resonator, this means that any losses and any population of thermal photons have to be minimized. To accomplish both conditions the resonators are made of superconducting material and used under cryogenic temperatures.
In the following section general properties of microwave resonators will be introduced. Subsequently two different types of microwave resonator will be discussed and at the end of this chapter a few aspects of the fabrication of the resonators are briefly mentioned.

2.1. General properties of microwave resonators

There are two different kind of resonator types we work with: distributed and discrete devices with respect to the inductance L and the capacitance C. In the following general properties of resonant electromagnetic circuits will be introduced on the basis of discrete L and C. However, since the distributed resonators close to resonance can be approximated by an equivalent circuit of discrete L and C elements, the following description holds for both types of resonator.

Energy Energy in a RCL circuit can be stored in the electric field of the capacitor and in the magnetic field of the inductor. In a resonant circuit energy sloshes back and forth between the inductor and the capacitor. In the case of a parallel RLC circuit the averaged values for the electric and magnetic energy can be written as [Poz05]

$$W_{\mathrm{e}} = \frac{1}{4}|V|^2 C, \tag{2.1a}$$

$$W_{\mathrm{m}} = \frac{1}{4}|V|^2 \frac{1}{\omega^2 L} \tag{2.1b}$$

with the voltage V (see Fig. 2.1) and the angular frequency ω.

Impedance In a parallel AC circuit the input impedance Z_{in} (see Fig. 2.1), which is the complex ratio of the total voltage and current V/I [1] can be written as [Poz05]

[1] As this thesis will mainly be read by physicist I stick on the tradition to label the imaginary parts of complex expressions with i instead of using j which is common among electrical engineers

$$Z_{\mathrm{in}}(\omega) = (\frac{1}{R} + \frac{1}{\mathrm{i}\omega L} + \mathrm{i}\omega C)^{-1}. \tag{2.2}$$

Using Eqs. 2.1a,b and the fact that the power dissipated by the resistor $P_{\mathrm{loss}} = |V|^2/(2R)$, Eq. 2.2 becomes

$$Z_{\mathrm{in}}(\omega) = \frac{P_{\mathrm{loss}} + 2\mathrm{i}\omega(W_{\mathrm{m}} - W_{\mathrm{e}})}{\frac{1}{2}|I|^2}. \tag{2.3}$$

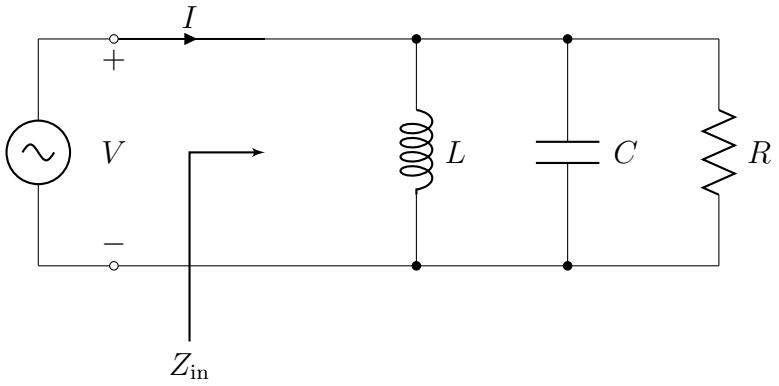

Figure 2.1.: A parallel RLC circuit with the input impedance Z_{in} that denotes the equivalent impedance of an electrical network "seen" by a power source connected to that network.

Circuits whose impedances exhibit distinct minima or maxima are resonant circuits. One can see from Eq. 2.3 that Z_{in} becomes real and a minimum when W_{m} equals W_{e}:

$$Z_{\mathrm{in}}|_{\omega=\omega_0} = R. \tag{2.4}$$

So, the input impedance Z_{in} at resonance is limited by the ohmic resistance R of the circuit. Therefore our resonators are made of a superconducting material in order to keep the ohmic losses as low as possible.

Resonance frequency From the resonance condition $W_{\mathrm{m}} = W_{\mathrm{e}}$ one can directly derive an equation for the angular resonance frequency ω_0:

$$W_{\mathrm{m}} = W_{\mathrm{e}} \rightarrow \omega_0 = \frac{1}{\sqrt{LC}}. \tag{2.5}$$

From Eq. 2.1a one can see that the mean electric energy W_e does not depend on the frequency ω while the magnetic energy W_m decreases quadratically with increasing ω. Therefore the reactance of $Z_\mathrm{in}(\omega)$ (see Eq. 2.3) is inductive for $\omega < \omega_0$ and capacitive for $\omega > \omega_0$.

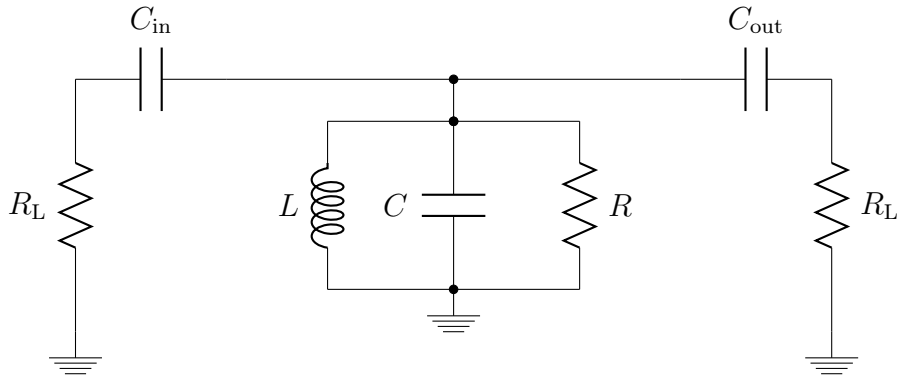

Figure 2.2.: A parallel RCL circuit that is coupled to an input and output line (represented by R_L) via the coupling capacitors $C_\mathrm{in/out}$.

Resonator loading In any transmission measurement, the RCL circuit has to be coupled to an input and output line which is represented by R_L in Fig. 2.2. This can be achieved by using coupling capacitors $C_\mathrm{in/out}$. If the coupling capacitors are different then the resonator is called *asymmetrically* coupled, else *symmetrically* coupled. If e.g. $C_\mathrm{out} > C_\mathrm{in}$ the probability that a photon, once in the resonator, leaves via C_out is accordingly enhanced.

Capacitive coupling of the resonator to an external circuit increases the total stored electric energy W_e respectively the total capacitance C. In order to match the condition $W_\mathrm{e} = W_\mathrm{m}$, the resonance frequency ω_0 has to shift slightly to smaller frequencies. Similar arguments hold for any increase of C or L as one can from Eq. 2.5.

Transmission Close to resonance the transmission $T = \frac{P_\mathrm{out}}{P_\mathrm{in}}$ of a resonator can be well described by a Lorentzian curve (see Fig. 2.3). In general, the transmission at resonance T_res will always be smaller than unity and exhibit a finite width. The former is due to

existing ohmic resistance and the latter mainly due to intrinsic dielectric losses of the resonator since radiative losses can be neglected [Goe08]. In practice the width of the resonance curve depends on the total losses, that will be introduced in the following.

Quality factor The dimensionless Q factor is an important measure to characterise the losses of a resonator. The Q factor can also be seen as a measure of the quality of the photon confinement in the resonator, thus a measure of how often the photon is reflected by the coupling capacitors $C_{\text{in/out}}$ before it is lost. A valid expression for high Q resonators ($Q > 1/2$) is the following:

$$Q = \frac{\omega_0}{\Delta\omega} = \frac{f_0}{\Delta f}, \tag{2.6}$$

where $\Delta\omega$ and Δf are the respective full width at half maximum (FWHM) of the transmission signal (see Fig. 2.3). Note that the Q factor is not generally fixed, there exists various definitions that deviate from each other.

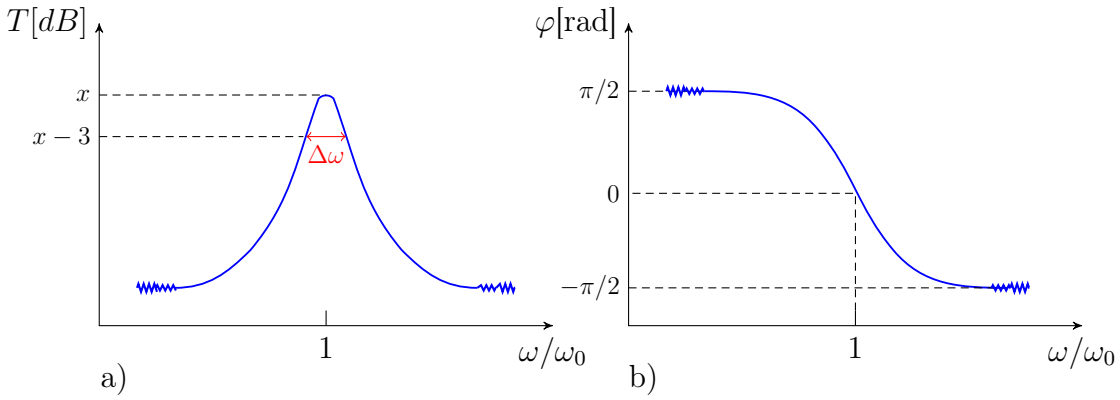

Figure 2.3.: Close to resonance the transmission of a resonator exhibits a Lorentzian line shape. (a) The transmission T in a logarithmic scale: $T[dB] = 10\log_{10}\frac{P_{out}}{P_{in}}$. The FWHM denoted as $\Delta\omega$ represents the distance between the two points in the frequency domain at which the magnitude of the signal is equal to half of its maximum value (corresponding to a decay of -3 dB in log. scale). (b) The relative phase φ between current and voltage shows a jump of π around the resonance frequency.

The total Q factor of a circuit Q_L (a so called loaded quality factor), can be separated

into at least two parts, Q_{int} and Q_{ext}, that are summed up as follows:

$$\frac{1}{Q_{\text{L}}} = \frac{1}{Q_{\text{int}}} + \frac{1}{Q_{\text{ext}}}. \tag{2.7}$$

Q_{int} accounts mainly for dissipative and radiative losses while Q_{ext} is governed by the coupling to external circuitry which is in our case given by the input and output capacitors C_{in} and C_{out}. Coupling reduces therefore Q_{L} as it reduces the property of the circuit to store energy. Q_{L} is always limited by the smaller value of Q_{ext} and Q_{int}. Therefore there are basically two regimes and one special case, depending on the coupling-factor $g = Q_{\text{int}}/Q_{\text{ext}}$.

- $g \gg 1$ ($Q_{\text{int}} > Q_{\text{ext}}$): the resonator is called *over-coupled* and is limited by Q_{ext} which leads usually to a low quality factor Q_{L}. This is the requirement in order to perform fast measurements.

- $g \ll 1$ ($Q_{\text{int}} < Q_{\text{ext}}$): the resonator is *under-coupled* and governed by Q_{int} which leads usually to a large quality factor Q_{L}. As a consequence the photon storage time in the resonator becomes relatively large.

- $g = 1$ ($Q_{\text{int}} = Q_{\text{ext}}$): the resonator is said to be *critically* coupled. If $\omega = \omega_0$, the resonator is matched to the feed line and therefore a maximum of power is transferred.

Q_{L} can be directly determined from the width of the Lorentzian line shape. Experimentally one can obtain values for Q_{int} and Q_{ext} if one can also measure the transmission of the pure line (without resonator). This is not possible for half wave resonators since they transmit only on resonance. In the case of a LER, which will be discussed in one of the following subsections, one can distinguish between the internal and the external losses experimentally since they behave like a through line if they are probed far off-resonance.

Loss rate Another related measure to the quality factor is the resonator decay rate κ:

$$\kappa = 2\pi\frac{\Delta f}{2} = \frac{\Delta\omega}{2}. \tag{2.8}$$

In the above equation κ is related to $\Delta f/2$, the half width at half maximum (HWHM). Note that there are different used definitions of κ circulating. We choose a relation to HWHM because then κ is directly related to the energy loss of the resonator: at time $t = 1/\kappa$ the magnitude of the exponential decay has become 1/e.

Mean lifetime From the inverse of κ one gets the mean lifetime τ of a photon in a resonator:

$$\tau = \frac{1}{\kappa}. \tag{2.9}$$

The above mentioned properties (κ, ω_0, Q_L) of a resonant circuit can be determined from the transmission amplitude that is usually a Lorentzian curve around the resonance frequency (see Fig. 2.3a). However, these informations reside also in the relative phase between the current I and the voltage V in the circuit.

Phase In a circuit which only consists of ohmic resistors, current and voltage are in phase with each other, which basically means that the peak voltage is reached at the same instant as the peak current. The situation is different when circuits have capacitive and inductive components.
For a capacitive circuit the current leads the voltage by 90° while an inductive circuit the current lags behind the voltage by 90°. Hence, the phase of the transmission signal below(above) the resonance frequency has inductive(capacitive) characteristics. Exactly at resonance the inductive and capacitive impedance cancel each other so that only the ohmic resistance remains and the phase difference is zero. This change in impedance causes a phase shift of π around resonance (see Fig. 2.3b)

2.2. Half wave transmission line resonators

The half wave transmission line (TL) resonator we used is a quasi one-dimensional, open terminated transmission line of a certain length l that defines the wavelength λ of the fundamental mode and the resonance frequency ω_0, respectively. For a given λ the appropriate length l of the transmission line is the eponymous half wave. At resonance

a standing wave is formed along the resonator length. Since the wavelength is on the order of the length of the device one has to use a distributed element model for a general description of the circuit.

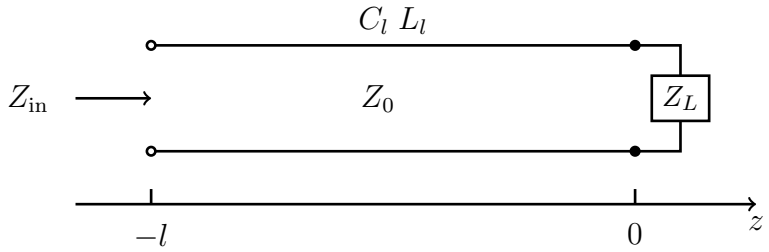

Figure 2.4.: With a load impedance Z_L terminated transmission line. The characteristic impedance Z_0 refers to the transmission line, C_l and L_l are per unit length

In transmission line theory the inductance L and the capacitance C that are necessary to build an electromagnetic resonator are assumed to be spatially distributed along the length l of the transmission line. That means the capacitance and inductance can't be separated into lumped capacitors and inductors as is possible in the regime where Kirchhoff's rules apply. Therefore one introduces L_l and C_l, the inductance and capacitance per unit length for a complete description of the resonator.

Resonance frequency Relations between the essential parameters are as follows (see e.g. [Che97], [Poz05]):

$$l = \frac{\lambda}{2} = \frac{v_{\text{ph}}\pi}{\omega_0} = \frac{c_0\ \pi}{\omega_0\sqrt{\epsilon_{\text{eff}}}} = \frac{\pi}{\omega_0\sqrt{L_l C_l}} \tag{2.10}$$

with the phase velocity v_{ph}, the vacuum speed of light c_0 and the effective dielectric constant ϵ_{eff}. Using Eq. 2.10 an explicit expression for the resonance frequency becomes

$$\omega_0 = \frac{\pi}{l\sqrt{L_l C_l}}. \tag{2.11}$$

At resonance the incoming and the reflected waves interfere constructively and form a standing wave along the resonator length l.

Near resonance there exist equivalent lumped element circuits for the description of distributed resonators as already used in the previous section. The equivalent lumped element circuit for an open-terminated transmission line ($Z_L = \infty$) is a parallel RCL resonator (see Fig. 2.1).

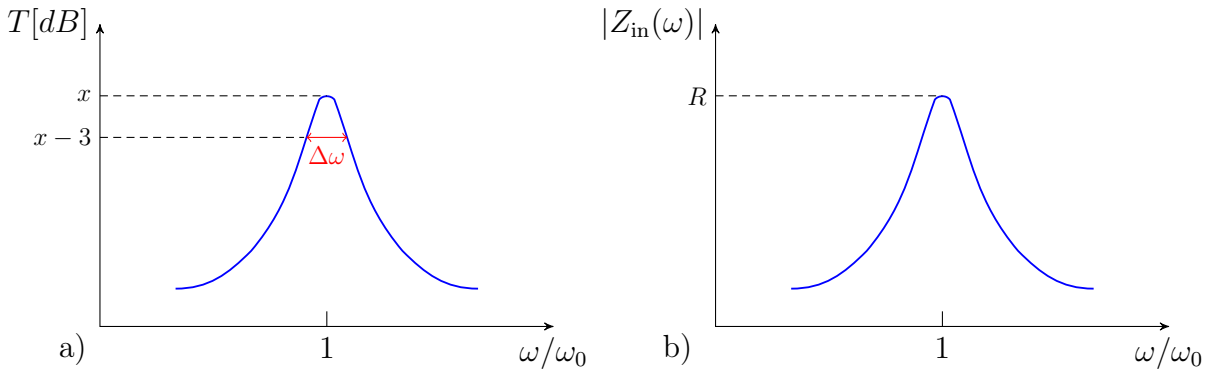

Figure 2.5.: The magnitudes of the transmission (a) and input impedance (b) are Lorentzian-like close to the resonance frequency ω_0. Z_{in} at resonance is real and equal to the ohmic resistance R.

Input impedance Z_{in} For a travelling wave on a transmission line the impedance is called *characteristic impedance* Z_0 and is given by

$$Z_0 = \sqrt{\frac{L_l}{C_l}}. \tag{2.12}$$

So, Z_0 is characteristic for the line alone. Another important characteristic measure of the whole system, including lines and loads, is the already mentioned input impedance Z_{in} of the line. Thus the input impedance Z_{in} changes when the transmission line is terminated by a load impedance Z_L and becomes spatially dependent. A general expression for the input impedance Z_{in} at a distance l from the load can be written as [Poz05]

$$Z_{\text{in}} = \frac{V}{I}\Big|_{z=-l} = Z_0 \frac{Z_L + Z_0 \tanh(\gamma l)}{Z_0 + Z_L \tanh(\gamma l)}, \tag{2.13}$$

with the complex propagation constant $\gamma = \alpha + \mathrm{i}\beta$, the attenuation constant $\alpha = R\sqrt{C_l/L_l}$ and the phase constant $\gamma = 2\pi/\lambda$. As we are working with superconduct-

ing transmission lines resonators, the ohmic resistance R is very small and therefore $\alpha \ll 1$. If we consider now an open-terminated transmission line resonator Z_L becomes ∞ and the right-hand side of Eq. 2.13 becomes

$$Z_{\text{in}}|_{Z_L \to \infty} \xrightarrow{l'Hopital} Z_0 \coth(\gamma l) = Z_0 \coth((\alpha + \mathrm{i}\beta)l). \tag{2.14}$$

If we further assume that $\lambda = 2l$ at $\omega = \omega_0$, the right side of Eq. 2.14 can be expanded close to resonance with $\omega = \omega_0 + \Delta\omega$ [Poz05]

$$Z_{\text{in}} = \frac{Z_0}{\alpha l + \mathrm{i}(\Delta\omega\pi/\omega_0)}. \tag{2.15}$$

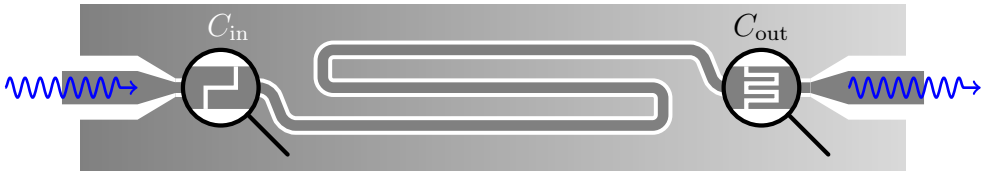

Figure 2.6.: An asymmetrically coupled ($C_{\text{in}} \neq C_{\text{out}}$) triple pass half wave TL resonator.The term triple pass refers to the fact that the feed line passes the centre of the resonator three times. This resonator design is already optimized with respect to magnetically coupling since the magnetic field of the electromagnetic mode is maximum in the centre.

Z_{in} as well as the transmission T as a function of ω are Lorentzian curves around ω_0 (see Fig. 2.5).

Transmission Near resonance a simple expression for the magnitude of the complex transmission parameter S_{21} (see Chap. A) of a loaded half wave resonator is a Lorentzian lineshape [Goe08]

$$|S_{21}(\omega)|^2 = \frac{|A|^2}{1 + 4Q_{\text{L}}^2(\frac{\omega-\omega_{\text{r}}}{\omega_{\text{r}}})^2} \tag{2.16}$$

with the complex amplitude A at resonance, the total quality factor Q_{L} and the resonance frequency ω_{r}. The corresponding complex amplitude is

$$S_{21}(\omega) = \frac{A}{1 + 2\mathrm{i}Q_{\mathrm{L}}(\frac{\omega-\omega_{\mathrm{r}}}{\omega_{\mathrm{r}}})}. \tag{2.17}$$

Instead of fitting the magnitude on the basis of Eq. 2.16 one can also fit the frequency dependent phase

$$\varphi = \arctan\Big(\frac{\mathrm{Im}(S_{21})}{\mathrm{Re}(S_{21})}\Big) \tag{2.18}$$

which leads to the following expression using Eq. 2.17:

$$\varphi(\omega) = \arctan(2Q_{\mathrm{L}}(\frac{\omega - \omega_{\mathrm{r}}}{\omega_{\mathrm{r}}})). \tag{2.19}$$

2.3. Lumped element resonators

The lumped element resonators (LER) we use are „lumped“ in the sense that the wavelength λ of the resonance frequency is much larger than the dimension of the resonator structure. They are lumped also in the sense that the electric and magnetic fields are more or less separated (see Fig. 2.7b). It is a resonant structure fed by a coplanar transmission line that we therefore also sometimes call „feed line“. The coupling to a feed line can be achieved capacitively as well as inductively. The equivalent circuit of a capacitively coupled LER is shown in Fig. 2.7 and is the same as for a distributed TL resonator described in the previous section: a parallel RLC circuit. As the coupling is parallel to a

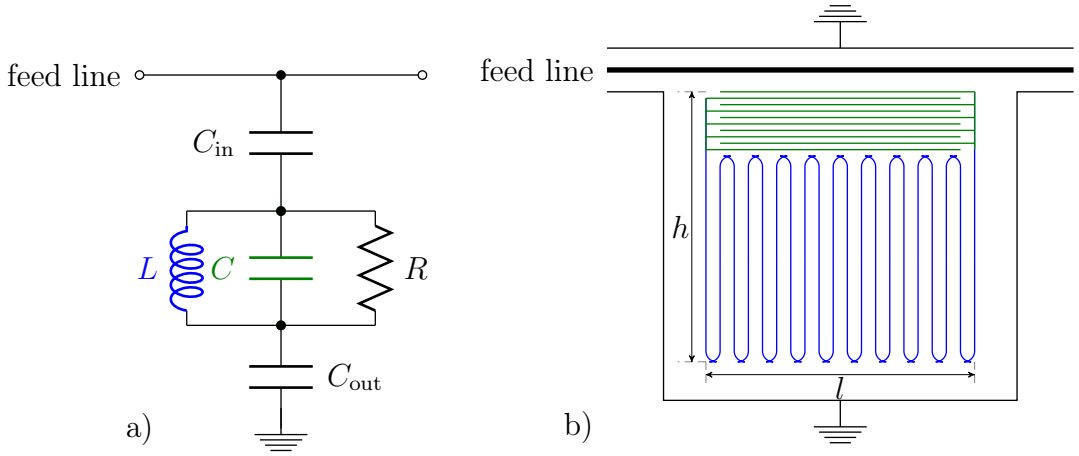

Figure 2.7.: (a) Equivalent circuit for a capacitively coupled LER. (b) The real circuit. h and l are in the range of 100 μm.

feed line, the transmission close to resonance becomes an inverse Lorentzian shape. (see

Fig. 2.8). There are several differences compared to a TL resonator that makes a LER an interesting alternative. The size of the resonant structure in principle can be shrunk in all dimensions as long as the proper values for L and C are maintained (one is not tight to the length $l = \lambda/2$ as it is the case for the half wave resonator). A reduced mode volume V_{mod} increases the field strength (see Eq. 2.26) that enhances the coupling to other resonant systems (see Chap. 4). The separation of the electric and the magnetic field for example is a feature that might allow to distinguish electric and magnetic effects on the resonators properties.

Resonators that are designed to have a resonance frequencies in the range of several

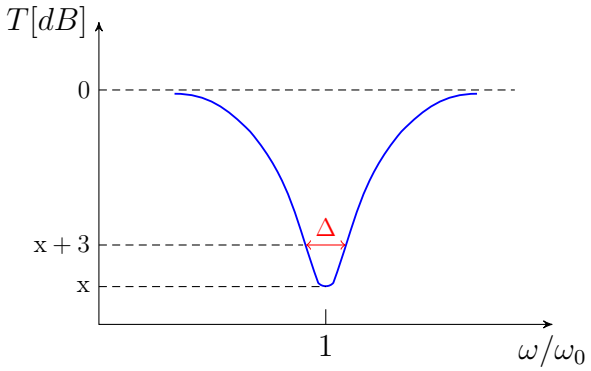

Figure 2.8.: Transmission T close to resonance is an inverse Lorentzian.

GHz are not realizable with standard macroscopic L and C components due to stray capacitances and inductances that would make such a device uncontrollable. However, microfabricating capacitive and inductive structures on a single substrate circumvents these problems. Moreover, radiation losses are expected to be small due to the fact that size of the resonant structure is much smaller than the resonant wavelength [Doy08].

LER are coupled once to the feed line and once to the ground. The coupling to ground is needed as otherwise no current could run through the resonator and would be decoupled from the feed line [Kol12]. As the uncoupled resonator is a parallel RCL structure, the impedance Z_{in} is the same as described in Eq. 2.15 for an open terminated TL resonator. The angular resonant frequency for a LER is given as

$$\omega_0 = \frac{\pi}{\sqrt{LC}}, \tag{2.20}$$

	LER	TL resonator
Coupling to external circuit	parallel	serial
coupling modus	capacitively/inductively	capacitively
transmission near resonance	inverse Lorentzian	Lorentzian
equivalent circuit	parallel RLC	parallel RLC
C, L	separable	not separable
constraints of mode volume	fabrication	wavelength λ

Table 2.1.: Comparison of a few properties between LER and TL resonator.

thus independent from the wavelength no harmonics are supported. As shown in Fig. 2.8b transmission near resonance for LER is an inverse Lorentzian curve. On resonance the transmission of an ideal LER is zero. Off-resonance the signal is transmitted undisturbed and thus a LER acts as a mere through-line. Therefore Q_{int} and Q_{ext} can be determined separately.

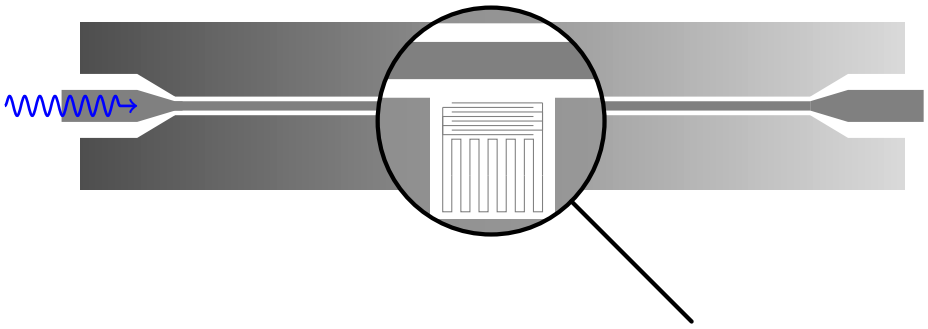

Figure 2.9.: The figure schematically shows a LER that is fed by a coplanar transmission line and emphasizes the different length scales involved.

2.4. Quantum mechanical description of an electromagnetic resonator

A distributed resonator e.g. a transmission line (TL) resonator can be modelled as a chain of uncoupled LC oscillators. The chain of LC elements models the fact that a TL

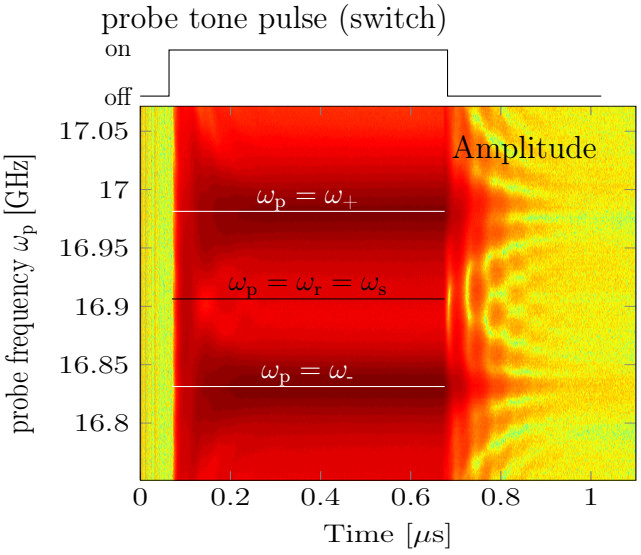

Figure 2.10.: The figure schematically shows a LER that is fed by a coplanar transmission line and emphasizes the different length scales involved.

resonator can support harmonics of the fundamental mode whereas a LER only supports the fundamental mode. If one is interested in a small range of a specific mode of a TL resonator, one can neglect contributions resulting from other modes and can end up with the lumped element model.

The total averaged energy of a LC oscillator is

$$E = \frac{1}{2}LI^2 + \frac{1}{2}CV^2. \tag{2.21}$$

Quantization of the electromagnetic circuit can be achieved via deriving an expression for the classical Hamiltonian $H(\Phi, q)$ as a function of the flux Φ stored in the inductor and the charge q stored in the capacitor as the corresponding conjugate variables. With the relations $V = q/C$ and $I = \Phi/L$ one obtains the corresponding Hamiltonian [Fin10]

$$H(\Phi, q) = q^2/2C + \Phi^2/2L. \tag{2.22}$$

This Hamiltonian has already the form of a classical mechanical harmonic oscillator if the electromagnetic values are replaced by their corresponding mechanical counterparts : mass $m \rightarrow$ inductance L, elongation $x \rightarrow$ charge q, spring constant $k \rightarrow$ inverse charge C^{-1} and momentum $p \rightarrow$ flux Φ. Quantisation leads to the well known harmonic oscillator Hamiltonian $H = \hbar\omega_r(a^\dagger a + 1/2)$.

Instead of circuit quantisation one can quantise the electric and magnetic fields that correspond to the capacitance C and inductance L to achieve the same quantum mechanical description. With the coulomb gauge the electromagnetic field components $\mathbf{B}$ and $\mathbf{E}$ can be expressed in terms of the vector potential $\mathbf{A}$ only:

$$\mathbf{B} = \nabla \times \mathbf{A}, \tag{2.23a}$$

$$\mathbf{E} = -\frac{\partial \mathbf{A}}{\partial t}. \tag{2.23b}$$

Making use of the well known Maxwell equations a wave equation for $\mathbf{A}$ in a region free of charges and currents can be obtained:

$$\nabla^2 \mathbf{A} - \frac{1}{c^2}\frac{\partial^2 \mathbf{A}}{\partial t^2} = 0. \tag{2.24}$$

After separation of time and spacial variables, the use of periodic boundary conditions and a bit of luck the final expression of $\mathbf{A}$ for plane waves is [Ors07]

$$\mathbf{A}(\mathbf{r},t) = \sum_m \sqrt{\frac{\hbar}{2\omega_\mathrm{m}\varepsilon_0 V_\mathrm{mod}}}\mathbf{e}_\mathrm{m}\{a_\mathrm{m}\exp[\mathrm{i}(\mathbf{k}_\mathrm{m}\cdot\mathbf{r}-\omega_\mathrm{m}t)] + a_\mathrm{m}^\dagger \exp[-\mathrm{i}(\mathbf{k}_\mathrm{m}\cdot\mathbf{r}-\omega_\mathrm{m}t)]\}. \tag{2.25}$$

The sum index m denotes the mode, V_mod the mode volume, a_m and $a_\mathrm{m}^\dagger$ are complex coefficients of the time dependent terms and $\mathbf{e}_\mathrm{m}$ is the polarization vector. In Eq. 2.25 one can see already the inverse dependency of the vector potential $\mathbf{A}(\mathbf{r},t)$ from the mode volume V_mod within the factor $\sqrt{\frac{\hbar}{2\omega_\mathrm{m}\varepsilon_0 V_\mathrm{mod}}}$. The same dependence will also hold for the electric and magnetic field, derived from $\mathbf{A}(\mathbf{r},t)$. Following the instructions of Eqs. 2.23 and using the relation $c^{-1} = \sqrt{\mu_0\epsilon_0}$ the electric and magnetic field in vacuum become [Ors07]

$$\mathbf{B}(\mathbf{r},t) = -\mathrm{i}\sum_m \sqrt{\frac{\mu_0\hbar\omega_\mathrm{m}}{2V_\mathrm{mod}}}\mathbf{e}_\mathrm{m}\times\mathbf{k}_\mathrm{m}\{a_\mathrm{m}\exp[\mathrm{i}(\mathbf{k}_\mathrm{m}\cdot\mathbf{r}-\omega_\mathrm{m}t)] + a_\mathrm{m}^\dagger\exp[-\mathrm{i}(\mathbf{k}_\mathrm{m}\cdot\mathbf{r}-\omega_\mathrm{m}t)]\}, \tag{2.26a}$$

$$\mathbf{E}(\mathbf{r},t) = \mathrm{i}\sum_m \sqrt{\frac{\hbar\omega_\mathrm{m}}{2\epsilon_0 V_\mathrm{mod}}}\mathbf{e}_\mathrm{m}\{a_\mathrm{m}\exp[\mathrm{i}(\mathbf{k}_\mathrm{m}\cdot\mathbf{r}-\omega_\mathrm{m}t)] + a_\mathrm{m}^\dagger\exp[-\mathrm{i}(\mathbf{k}_\mathrm{m}\cdot\mathbf{r}-\omega_\mathrm{m}t)]\}. \tag{2.26b}$$

The total energy of the multimode radiation field is given by

$$H = \frac{1}{2}\int_{V_{\mathrm{mod}}} (\epsilon_0 \mathbf{E}^2(\mathbf{r},t) + \frac{1}{\mu_0}\mathbf{H}^2(\mathbf{r},t))\mathrm{d}^3\mathrm{r}. \tag{2.27}$$

Inserting Eqs. 2.26 in the expression above and making use of the orthogonality relations of the spacial mode functions (= plane waves in this case) one finally may end up with the following expression [Ors07]:

$$H = \sum_m \hbar\omega_{\mathrm{m}}(a_{\mathrm{m}}^\dagger a_{\mathrm{m}} + \frac{1}{2}) \tag{2.28}$$

with $a_{\mathrm{m}}^\dagger, a_{\mathrm{m}}$ representing already the bosonic ladder operators. Eq. 2.28 holds for linear superconducting resonators. For resonant structures made of lumped element devices we have to drop the sum over the modes because they do not support any harmonics. In the case of CPW resonators of length l modes at frequencies $\omega_{\mathrm{m}} = (\mathrm{m}+1)\pi c/l$ (c being the speed of light in the TL) are supported. But even in this case the sum over the modes can be dropped if the quality factor Q is high, or rather the width of the transmission signal so narrow that only the mode closest in frequency to the system we are interested to interact with, has to be considered. Therefore

$$H = \hbar\omega_{\mathrm{r}}(a^\dagger a + \frac{1}{2}) \tag{2.29}$$

is a valid description for the distributed as well as for the lumped element resonators as far as they behave linearly. As we are working with resonant structures made of superconducting material they behave linear if they are operated well below the crucial parameters T_{C}, ω_{C}. But if the input power P_{in} is too high, strongly inhomogeneous current distributions in the structures predominantly at edges can cause non-linear effects too.

2.5. Fabrication and field distribution in a resonator

In the following the main fabrication steps of superconducting resonators that we built in the cleanroom at the ZNMS will be briefly discussed. (for a detailed description see [Kol12]). A cross-section of a transmission line resonator is shown in Fig. 2.11. The

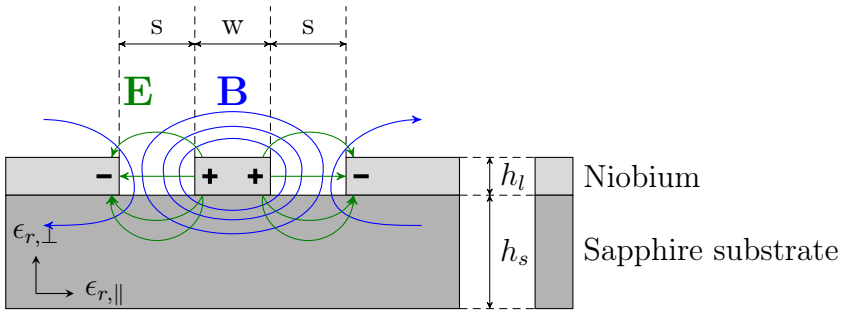

Figure 2.11.: Cross-section of a transmission line resonator, $s = 20\,\mu m$, $w = 8.3\,\mu m$, $h_s = 330\,\mu m$, $h_l = 200\,nm$

insulating substrate is made out of sapphire, a crystalline form of Al_2O_3. The main advantages of using sapphire are its low loss tangent and low thermal expansion coefficient that is necessary to keep the niobium structure on top when switching between a few mK temperature and room temperature. The dielectric constant ϵ_r is anisotropic and its value perpendicular (9.3) to the surface is slightly smaller than parallel (11.5) to it. To achieve high values for Q_{int} or rather to keep the resistive losses as small as possible the material used for the superconducting resonator structure is niobium that is sputtered on a sapphire substrate. If a resonator is operated well below critical temperature T_c of the superconductor and below the frequency of the superconducting gap radiation and resistive losses are expected to be small [Goe08]. In order to meet these needs a high critical temperature T_c is necessary. Niobium has the highest T_c of the elemental superconductors which is around 9.2 K. Since the boiling point of niobium is quite high (5017 K) sputtering the niobium is prioritised to evaporative deposition.

The thickness of the metal films is the same for both, a LER and a half wave TL resonator, while the feature size of the first is by a factor of 10 smaller. LERs that are designated to work in the GHz regime have to be microfabricated. Additional (stray) capacitances and inductances resulting from the usage of conventional lumped L and C components would be too big [Kol12]. From Fig. 2.11 one can see that the fields are predominantly concentrated in the gaps between the conductor and the ground planes. To provide well defined boundary conditions the resonator is put into a sample box made of copper (for a picture see Fig. B.1.

3. NV^- centres

In the previous section basic properties of superconducting resonators were explained. In this section another resonant system, ensembles of nitrogen vacancy colour centres (NV^- centres) in a diamond crystal will be introduced so that in the following sections its coupling to a resonator can be discussed.

The coherence time of a system is basically determined by the degree of isolation from its environment. Therefore a trapped and well isolated single ion for example will in general have better coherence properties than a single spin inside a solid state system.

However, for NV^- centres in diamond surprisingly long coherence times were found, even at ambient temperatures. In addition to that, the NV^- centres provide transitions in the optical and microwave domain which make them an ideal candidate to study interaction between matter and radiation [Jel06].

Single NV^- centres have been studied with respect to fundamental physics as well as in relation to practical purposes as e.g. extreme sensitive detectors for individual charges under ambient conditions [Dol11]. Single NV^- centres have been coupled to each other [Dol13] and to electron or nuclear spins of other neighbouring defects in the diamond crystal [Han06].

Magnetically coupling of a single NV^- centres to macroscopic devices (e.g a superconducting resonators) is to weak to perform coherent exchange of quantum information. The necessary interaction strength can only be reached by coupling to an ensemble of NV^- centres. Therefore the kind of quantum systems, that are finally introduced in this section, are ensembles of NV^- centres that among other things are designated to perform the storage of quantum information within hybrid quantum circuits due to its long coherence time [Kub10].

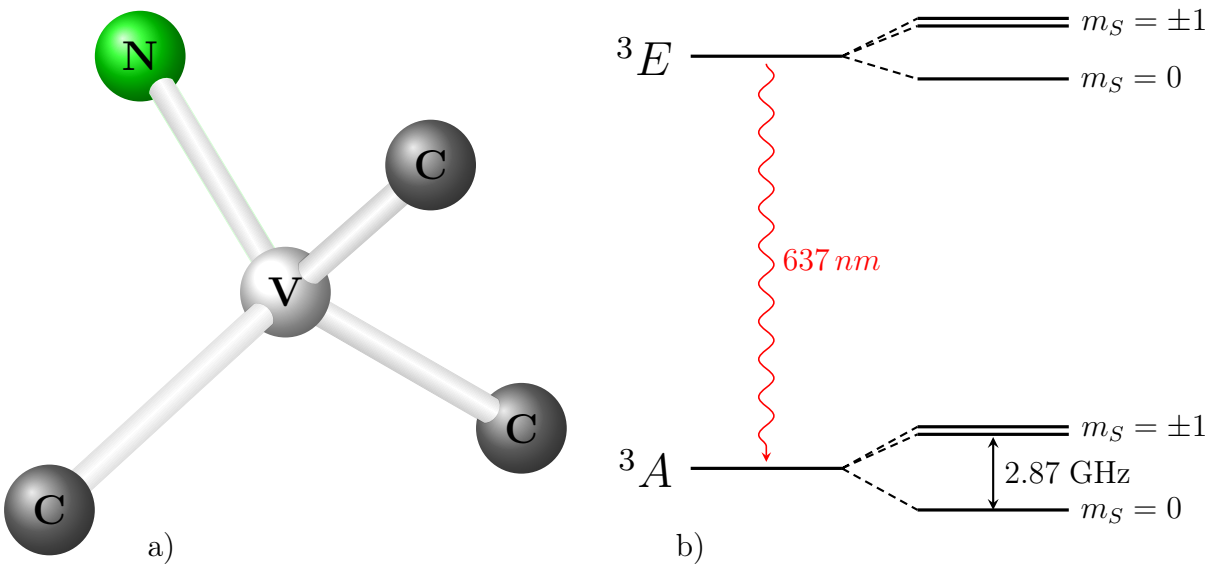

Figure 3.1.: (a) Shows a NV$^-$-centre and (b) its energy levels respectively the zero-field-splitting (ZFS).

3.1. Single NV$^-$ centre

In the following the physics of a single NV$^-$ centre will be outlined. NV$^-$ centres are point defects in the diamond lattice. They consist of a nitrogen atom substituting a carbon atom next to a lattice vacancy. A carbon atom has four valence electrons and in diamond each one is covalently bond to a next carbon atom-forming four single bonds. Therefore, a nitrogen atom with five valence electrons next to a vacancy in a diamond lattice provides a total of five unpaired electrons in a first step. In a second step four of them get covalently paired so that the NV centre finally ends up with one unpaired electron, thus a paramagnetic spin-half system. This is what is called a neutral NV centre or a NV^0 centre. If an additional electron is captured by the NV centre it becomes negatively charged, a so called NV$^-$ center (see Fig. 3.1). With the additional electron the NV$^-$ becomes a spin $S = 1$ system.

It was found that NV$^-$ centres possess a long coherence time (on the order of ms [Gop09]) compared to for example superconducting qubits (on the order of µs [Pai11]). This relatively long coherence time makes the NV$^-$ centre a candidate system for performing quantum memory tasks. Due to the rigid lattice of the diamond the spin dephasing time

is limited by residual paramagnetic impurity content and not by spin phonon coupling as often the case [Bat08]. Apart from the above mentioned advantages, NV^- feature other properties that allow their usage in circuit QED.

Even in the absence of an external magnetic field a zero-field splitting (ZFS) leads to a splitting of the three states $m_S = 0, \pm 1$ of the ground state spin triplet.

The ground state is split by an anisotropic dipolar interaction of the two unpaired electron spins, that can be described with a tensor of second rank. The tensor is traceless and can be transformed such that only two parameters (D and E) remain to describe the splitting of the NV^- ground state [Wra06]. The ZFS can be described with the following Hamiltonian:

$$H_{\text{zfs}} = \frac{1}{\hbar^2}(D(S_z^2 - \frac{1}{3}\mathbf{S^2}) + E(S_x^2 - S_y^2)) \tag{3.1}$$

with the fine structure constants D (spin-spin interaction) and E (strain) on the order of 2.87 GHz respectively a few MHz.

The electron spin resonance (ESR) frequency of the ZFS provides a microwave transitions in a range (GHz) that is suitable (see Fig. 3.1) to couple the NV^- centres with a microwave resonator. In addition to the ZFS the energy levels can be tuned via the Zeeman effect described by the following Hamiltonian

$$H_z = -\boldsymbol{\mu} \cdot \mathbf{B}_{\text{ext}} = -\frac{\mathrm{g}_e}{\hbar}\mu_B \mathbf{S} \cdot \mathbf{B}_{\text{ext}}, \tag{3.2}$$

with the electron Landé factor g_e for an electron, the Bohr magneton μ_B and the external magnetic field $\mathbf{B}_{\text{ext}}$.

The electron spin can also couple to surrounding nuclear spins. In diamond particularly the isotopes ^{14}N and ^{13}C possess non-vanishing nuclear magnetic dipole moments. The resulting hyperfine splitting due to the spin-one ^{14}N nucleus and the spin-half ^{13}C nucleus coupling is on the order of a few MHz and around 130 MHz, respectively. The according Hamiltonian for the hyperfine splitting is the following:

$$H_{\text{hf}} = \mathbf{S}^{\mathrm{T}} \cdot \bar{\bar{\mathbf{A}}} \cdot \mathbf{I} \tag{3.3}$$

with the nuclear spin $\mathbf{I}$ and the hyperfine coupling tensor $\bar{\bar{\mathbf{A}}}$. As the ^{14}N isotope is a constituent part of the NV^- center, hyperfine interaction always exists. As it is rather a weak interaction it is below our spectroscopic resolution. In [Fed11] e.g they show that

the hyperfine interaction with ^{14}N can be extracted from measurements in time domain. The hyperfine coupling with ^{13}C is much stronger but as the natural abundance in diamond is around 1.1 % [Wyk97] we still have to find out to what extend this interaction affects our experiments.

From the multiplet structure shown in Fig. 3.1 and from the Fig. 3.2 one can see that a single NV$^-$ center is a non-linear system. One of the ESR transitions from the $m_s = 0$ to the $m_s = \pm 1$ can act as an effective two-level system and can be chosen to function as a qubit [Web10].

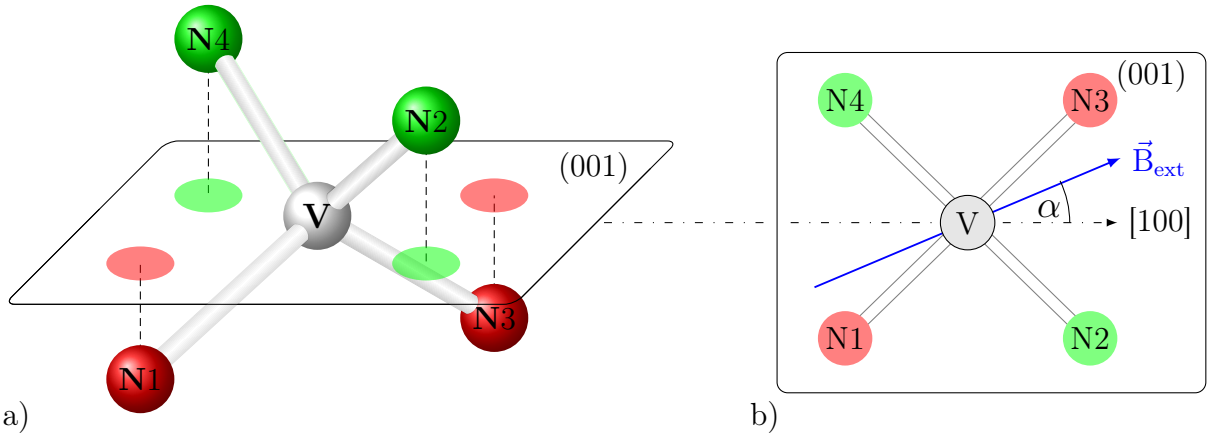

Figure 3.2.: (a) Mapping of the members of a NV$^-$ centre onto the (001) plane. (b) Forming two subensembles (red, green) with respect to the enclosing angle with an external magnetic field.

3.2. Ensembles of NV$^-$ centres in an external magnetic field

As one can see in Fig. 3.2a there are four different directions in which an axis between the vacancy V and one of the possible nitrogen lattice sites Ni (i = 1,2,3,4) can point and which can serve as a quantisation axis. In principle the NV$^-$ centre has eight different possibilities to be oriented since the vacancy and the nitrogen atom can exchange their position. But with respect to an external magnetic field B_{ext} this additional degree of

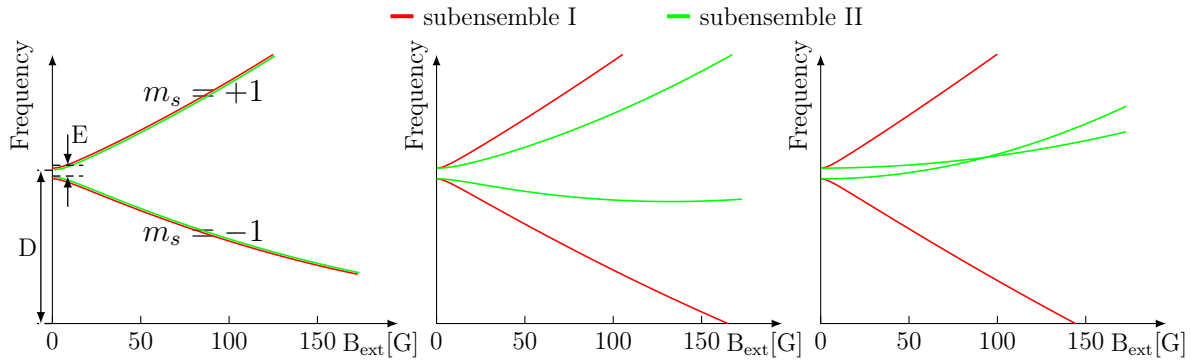

(a) $\alpha = 0°$ (b) $\alpha = 22.5°$ (c) $\alpha = 45°$

Figure 3.3.: The figures show the ESR transition frequencies from the $m_s = 0$ state to the $m_s = \pm 1$ states versus tuning external magnetic field B_{ext}. (a) D (≈ 2.87 GHz) and E (≈ 10 MHz) denote the ZFS. (b) $\alpha = 22.5°$ is a suitable angle if one wants to couple to a single (one out of two) subensemble. (c) As the $m_s = 0$ state also tunes with the magnetic field, the subensemble II (green) tunes even if $\alpha = 45° \Rightarrow \vec{B} \perp \vec{S}_{\text{II}}$.

freedom does not have any effect, therefore only four subensembles remain.

The number of NV$^-$ centres in a large ensemble is on the order of $10^{19}\,\text{cm}^{-3}$ so that one can assume that the four different orientations are uniformly distributed. The diamond we used was a (001) diamond, that means that it is cut such, that the (001) crystal plane coincides with the top and the bottom surface. Projecting these four different directions onto the (001) crystal plane (see Fig. 3.2)a it turns out that based on the symmetry of the diamond structure they enclose the same angle in pairs with any directions on the (001) plane (see Fig. 3.2)b. The Zeeman tuning is sensitive only to the projections of B_{ext} onto the quantisation axis. Therefore for any B_{ext} direction within the (001) crystal plane the subensembles N1 and N3 on the one hand and the subensembles N2 and N4 on the other hand will tune equally. Finally only two effective and distinguishable subensembles remain (marked with red and green in the Figs. 3.2,3.3). For certain angles ($\alpha = 0°, \pm 90°$) even the two remaining subensembles tune equally (see Fig. 3.3a).

3.3. Creation of NV^- centres

In order to create diamond samples with a high density of NV- centres we started out with buying a commercial artificial diamond. There are basically two different kinds of artificial diamonds: HPHT and CVD diamonds. HPHT refers to a high-pressure high-temperature (5 GPa, 1500 °C) process while CVD stands for chemical vapor deposition. The ones we used are HPHT type-Ib[1] diamonds. In order to achieve a maximum density of NV^- centres the main difficulty is the conversion of the substitutional nitrogen atoms into NV centres by the creation of vacancies. As mentioned at the beginning of this chapter there are mainly two steps that lead to a NV^- centre. In a first step the nitrogen atom has to meet a vacancy to create a spin $S = 1/2$ and neutral NV^0 centre. In a second step the NV^0 can convert to a spin $S = 1$ and negatively charged NV^- centre by capturing an additional electron. Any defect that is not converted into a NV^- centre causes additional interactions that lead to inhomogeneous broadening of the ESR frequency and thus reduce the coherence time.

The concentration of the nitrogen atoms in the single-crystal diamond ($4.5 \times 2.25 \times 0.5$ mm^3) as it was shipped by the company Element-6 was around 200 ppm. Vacancies can be created by irradiation of particles e.g neutrons or electrons. Unfortunately the particle irradiation causes besides the vacancies many other kinds of defects. Neutron irradiated diamonds for example lose their yellow shining colour and change to black, which indicates that the residual damage to the crystal lattice seems to be far more pronounced than with electron irradiation. For the coherence properties this means a considerable worsening. This step in the process is still an object of investigation in order to optimize it. The last step of the NV^- creation process is the annealing of the diamond at around 900 °C for several hours, on the one hand to increase the mobility of the vacancies in order to support the formation of NV centres and on the other hand to eliminate as much damage as possible caused by the irradiation process.
The diamonds we used for coupling to the resonator finally had a concentration of NV^-

[1] Nitrogen-contained diamonds are classified into the types 1a and 1b. The former contains nitrogen in aggregate form and the latter in singly substitutional form, respectively [Yos96]

centres of roughly 6 ppm. That means from the initial concentration of nitrogen atoms of 200 ppm around 3 % were converted into NV^- centres.

4. Coupling NV^- centres to a resonator

Two systems have been introduced so far, on the one hand a superconducting resonator and on the other hand an ensembles of NV^- centres.
The purpose of this chapter is to explain theoretically how one can understand the coupling of the magnetic dipole moments of the NV^- centres to the oscillating magnetic field of the resonator. With the idea of taking advantage of the relatively long coherence time of NV^- centres, the coupling between the two systems might be used for an information transfer. In order that information can be exchanged the two systems have to be brought into resonance. As the resonators we work with are not tunable, the ESR transition frequencies ω_s from the NV^- centres have to be tuned towards the resonator frequency ω_r.
In the following sections the behaviour of coupled oscillating systems is discussed once by a classical and once by quantum mechanical model.

4.1. Classical coupling

The physics of the following section is mainly taken from [Sch08]. A classical description of a mechanical analogue shows the coupling behaviour of two linear harmonic oscillators in a quite intuitive manner. Having a classical description of a coupled resonant system in mind may help also to recognise when and under what circumstances phenomena occur, that belongs only to the world of quantum mechanics.
Apart from this, under certain conditions both systems so far introduced can be described by a harmonic oscillator model. The requirements for a resonator to be described as a

harmonic oscillator have already been mentioned in Sec. 2.4. Under what circumstances the spin-system can be approximated as a harmonic oscillator is mentioned in Sec. 4.2.2. Let's consider two linear harmonic oscillators coupled via a spring that is attached to both oscillating objects, m_1 and m_2. To make the situation as simple as possible let us assume that the oscillators are lossless and have the same mass, $m_1 = m_2 = m$ and that the driving by an external force for the moment is switched off, thus $\omega_\mathrm{p} = 0$. A coupled system that is built up of two oscillating masses has basically two eigenfrequencies ω_s and ω_a.

Symmetric eigenfrequency ω_s If we choose the initial condition such that both masses are elongated in the same direction and the same distance x_0 it turns out that they oscillate in phase:

$$x_1(t) = x_2(t) = x_0 \cos(\omega_s t). \tag{4.1}$$

This motion is called a *symmetric normal oscillation* with the eigenfrequency $\omega_s = \sqrt{k/m}$. The masses move as if they weren't coupled, the length of the coupling spring remains constant.

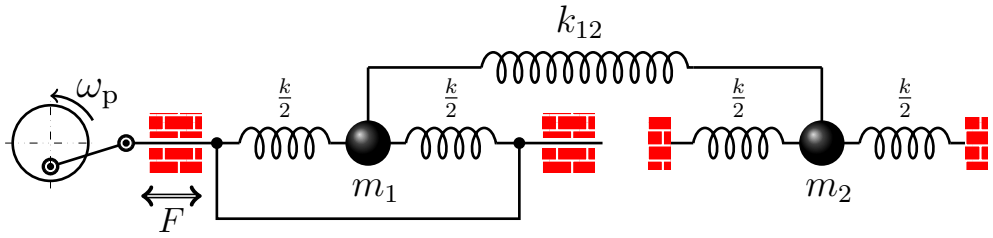

Figure 4.1.: A coupled system of two oscillators that is driven by an external force. This is already a mechanical analogue of the coupling experiment.

Antisymmetric eigenfrequency ω_a If we choose the initial condition so, that both masses are elongated in an opposite direction it turns out that they are in antiphase:

$$x_1(t) = -x_2(t) = -x_0 \cos(\omega_a t). \tag{4.2}$$

This motion is called an *antisymmetric normal oscillation* with the eigenfrequency

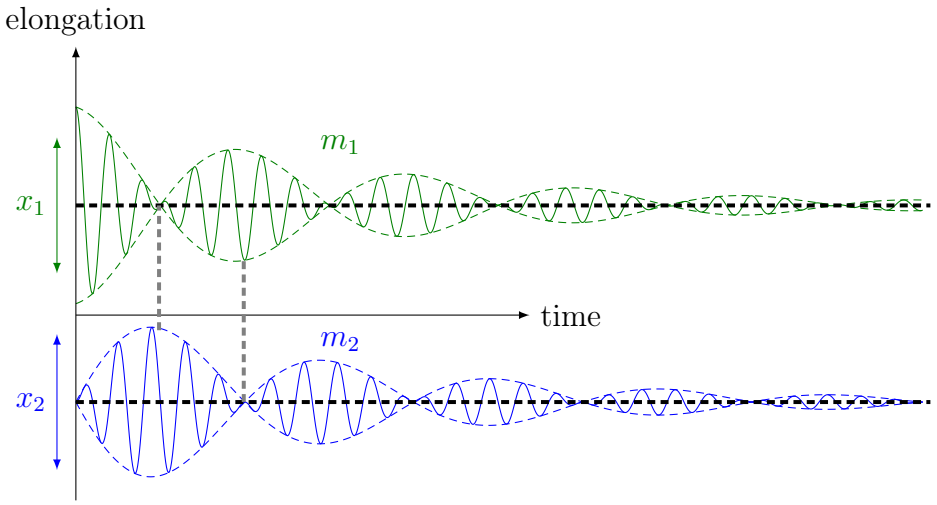

Figure 4.2.: The energy oscillates with the beat frequency till it is consumed completely by the damping.

$\omega_a = \sqrt{(k + k_{12})/m}$. The antisymmetric eigenfrequency ω_a is higher than the symmetric one and the coupling spring gets elongated and compressed maximum. As shown in the above special initial conditions the two eigenmodes of the system can be excited separately. If the conditions deviate from these special cases the motion is a composition of both eigenfrequencies. This results in an additional beat note with a period $T = 2\pi/(\omega_a - \omega_s)$ (see Fig. 4.2). The stronger the coupling (k_{12}) the greater the frequency ($\omega_a - \omega_s$) with which the excitation changes from one oscillator to the other.
If we switch on a driving frequency ω_p (see Fig. 4.1) scan it over a range that includes the eigenfrequencies one should see two resonances in the response of the system. The first when $\omega_\mathrm{p} = \omega_s$ and the second when $\omega_\mathrm{p} = \omega_a$. This behaviour is called a *normal mode splitting* and is shown in Fig. 4.3.

4.2. Quantum mechanical coupling

In the following section the characteristics of coupled systems will be discussed from a quantum mechanical point of view.
We will start with a simple model that describes the coupling of a single two-level system

(e.g a single NV$^-$ centre) to a single mode of an electromagnetic field (resonator). In a next step the model will be extended towards the coupling to an ensemble of two-level systems which results in an enhancement of the effective coupling strength. Once this has been worked out losses of the systems will be considered in order to define the different coupling regimes. In the last part coupling mechanisms in the time domain will be introduced.

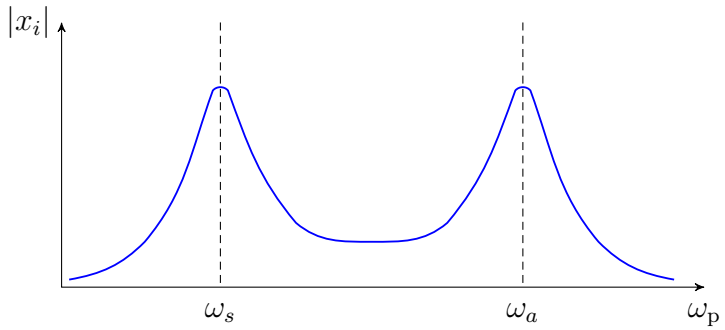

Figure 4.3.: Sweeping the driving frequency ω_p one will find a resonance for every eigenfrequency of the coupled system.

4.2.1. Jaynes-Cummings model: coupling to a single NV$^-$ centre

The first fully quantum-mechanical description of a two-level system interacting with a quantized mode of an electromagnetic field was given by E. Jaynes and F. Cummings in 1963 [Jay63]. In our case the part of the two-level atom is taken by the NV$^-$ centre. This two-level (atom-like) approximation is applicable when the resonance frequency of the resonator coincides with the microwave transition of the NV$^-$ centre [Fox07].
A Hamiltonian that describes a coupled system is:

$$H = H_0 + H_\mathrm{int} = H_\mathrm{field} + H_\mathrm{spins} + H_\mathrm{int}. \tag{4.3}$$

The first two contributions describe the uncoupled components of the system, thus the Hamiltonian of the quantized electromagnetic field H_field and the atomic Hamiltonian H_spin. The third contribution H_int finally covers the interaction.
Before taking a closer look at the individual parts of the Jaynes-Cummings model (JCM)

one should be aware of the approximations that are assumed. Important approximations, adapted to our experiments, are the following:

- lossless resonator and spin-system
- single electromagnetic field mode
- two accessible energy levels of the NV$^-$ center
- state of the NV$^-$ center oscillates between the two energy levels

To obtain the JCM the electromagnetic field of the resonator has to be quantized, the accessible energy levels of the spin-system have to be summed up and the magnetic dipole interaction has to be worked out.

In Sec. 2.4 we already derived the Hamiltonian for the electromagnetic field

$$H_{\text{field}} = \hbar\omega_{\text{r}} \left(a^\dagger a + \frac{1}{2} \right) \tag{4.4}$$

with $a^\dagger(a)$ denoting the bosonic creation (annihilation) operator of a photon.

Although the NV$^-$ centre is a $S = 1$ spin-system, we will restrict ourselves to only one of the transitions $m_s = 0 \rightarrow m_s = \pm 1$ and therefore approximate it as a $S = 1/2$ system. Limitation to two accessible states of the spin-system implies a two-dimensional basis $|e\rangle = (1\ 0)$ and $|g\rangle = (0\ 1)$ with their eigenenergies $E_\pm$. The Hamiltonian is a sum of all accessible energies, thus

$$H_{\text{spin}} = E_+|e\rangle\langle e| + E_-|g\rangle\langle g| = \begin{pmatrix} E_+ & 0 \\ 0 & E_- \end{pmatrix}. \tag{4.5}$$

If the energy difference $\Delta E = E_+ - E_- = \hbar\omega_{\text{s}}$ and the zero point energy is taken halfway between the ground $|g\rangle$ and the excited state $|e\rangle$ the corresponding energies become $E_\pm = \pm\frac{\hbar\omega_{\text{s}}}{2}$. Now, Eq. 4.5 can be reorganized in order to introduce the Pauli spin operators:

$$H_{\text{spin}} = \frac{1}{2} \begin{pmatrix} E_+ + E_- & 0 \\ 0 & E_+ + E_- \end{pmatrix} + \begin{pmatrix} \Delta E_- & 0 \\ 0 & -\Delta E = \end{pmatrix} = \frac{1}{2}(E_+ + E_-)\hat{\mathbf{1}} + \frac{1}{2}\Delta E\sigma_z \tag{4.6}$$

with $\sigma_z = |e\rangle\langle e| - |g\rangle\langle g|$. If one neglects the constant term $\frac{1}{2}(E_+ + E_-)\hat{\mathbf{1}}$ the spin-system Hamiltonian becomes [Ors07]

$$H_{\text{spin}} \approx \frac{\hbar}{2}\omega_{\text{s}}\sigma_z. \tag{4.7}$$

Finally, the third term H_{int} of the right side in Eq. 4.3 describes the interaction between the electromagnetic field and the spin-system. To work this out we will make use of several approximations. The first one is the dipole approximation. This holds if the wave length of the electromagnetic field is much larger then the dimension of the spin-system so that any variation of the electromagnetic field over the spin-system can be ignored. As we are operating in the microwave regime at a few GHz, the wavelength is on the order of several centimetres and this condition sufficiently met. A particle with a spin can possess a magnetic dipole moment. The electron spin magnetic dipole moment is

$$\boldsymbol{\mu}_s = -g_e \mu_B \frac{\mathbf{S}}{\hbar}, \tag{4.8}$$

with the electronic g-factor g_e, the Bohr magneton μ_B and the electron spin angular momentum $\mathbf{S}$. Coupling the spin momentum to the magnetic field $\mathbf{B}(\mathbf{r}, t)$ of the resonator a first draft of the corresponding Hamiltonian is

$$H_{\text{int}} = -\boldsymbol{\mu}_s \cdot \mathbf{B}(\mathbf{r}, t). \tag{4.9}$$

If we assume that the resonator only supports a single mode and furthermore to have a stationary rather than a travelling wave along the z-axis, the field can be written as [Ors07]

$$B(z, t) = \varepsilon_m (a + a^\dagger) \sin(kz) \tag{4.10}$$

with the magnetic field per photon ε_m. The complete interaction term finally becomes as follows:

$$H_{\text{int}} = \hbar \mathrm{g_s} (\sigma_+ + \sigma_-)(a^\dagger + a) \tag{4.11}$$

with σ_+ (σ_-) being the (de)excitation operator for the two-level system, the single coupling constant

$$\mathrm{g_s} = -\frac{\varepsilon_m M}{\hbar} \sin(kz) \tag{4.12}$$

with M being the matrix elements of the magnetic dipole operator and the magnetic field per photon

$$\varepsilon_m = \sqrt{\frac{\mu_0 \hbar \omega}{2 \mathrm{V_{mod}}}}. \tag{4.13}$$

As only transitions between two energy levels are allowed, the magnetic dipole has only off-diagonal elements. Expansion of the right-hand side of Eq. 4.11 produces terms that describe four different processes: $\hbar \mathrm{g_s}(a\sigma_+ + a^\dagger \sigma_- + a^\dagger \sigma_+ + a\sigma_-)$

- $a\sigma_+$ one photon is absorbed and the spin-system is excited from state $|g\rangle$ to $|e\rangle$
- $a^\dagger\sigma_-$ emission of a photon and de-excitation of the spin-system from state $|e\rangle$ to $|g\rangle$
- $a^\dagger\sigma_+$ one photon is emitted and the spin-system is excited
- $a\sigma_-$ one photon is absorbed and the spin-system gets de-excited

Only the first two processes are energy conserving. To find out more about the time dependence one can change from the Schrödinger picture to the interaction picture by the following action [Ors07]:

$$H_{\text{int}}^{(I)} = \mathrm{e}^{\frac{\mathrm{i}}{\hbar}H_0 t} H_{\text{int}} \mathrm{e}^{\frac{-\mathrm{i}}{\hbar}H_0 t} = \mathrm{e}^{\frac{\mathrm{i}}{\hbar}H_0 t} \hbar \mathrm{g_s}(\sigma_+ + \sigma_-)(a^\dagger + a) \mathrm{e}^{\frac{-\mathrm{i}}{\hbar}H_0 t}$$

with the unperturbed Hamiltonian $H_0 = H_{\text{field}} + H_{\text{spin}} = \hbar\omega_{\text{r}}\left(a^\dagger a + \frac{1}{2}\right) + \frac{\hbar}{2}\omega_{\text{s}}\sigma_z$. The operators in the interaction picture evolve in time according only to the unperturbed Hamiltonian while the time evolution of the state vectors depend only on the interaction term. The interaction Hamiltonian in the interaction picture finally becomes

$$H_{\text{int}}^{(I)} = \hbar \mathrm{g_s}\{\sigma_+ a\, \mathrm{e}^{[-\mathrm{i}(\omega_{\text{r}}-\omega_{\text{s}})t]} + \sigma_- a^\dagger \mathrm{e}^{[\mathrm{i}(\omega_{\text{r}}-\omega_{\text{s}})t]} \tag{4.14}$$

$$+\sigma_- a\, \mathrm{e}^{[-\mathrm{i}(\omega_{\text{r}}+\omega_{\text{s}})t]} + \sigma_+ a^\dagger \mathrm{e}^{[\mathrm{i}(\omega_{\text{r}}+\omega_{\text{s}})t]}\}. \tag{4.15}$$

In the expression above one can see that a resonant system ($\omega_{\text{r}} - \omega_{\text{s}} = 0$) removes any time dependency of the energy conserving processes. Unlike the non-resonant and non-energy conserving processes that oscillates quite fast with the sum of the frequencies $\omega_{\text{r}} + \omega_{\text{s}}$. As they average quickly to zero for any appreciable time scale, we can drop this non energy conserving terms. This is known as the *rotating wave approximation* (RWA). Going back to the Schrödinger picture the Hamiltonian in the dipole and rotating wave approximation becomes the above announced Jaynes-Cummings Hamiltonian

$$H_{\text{JC}} = \hbar\omega_{\text{r}} a^\dagger a + \frac{\hbar}{2}\omega_{\text{s}}\sigma_z + \hbar \mathrm{g_s}(\sigma_+ a + \sigma_- a^\dagger) \tag{4.16}$$

where the zero field energy $\frac{1}{2}\hbar\omega_{\text{r}}$ is set to zero.

Solutions of the JCM In the following section solutions of the JCM will be discussed and characteristic properties of coupling experiments like the *avoided crossing* of energy levels and the Rabi frequency Ω will be briefly introduced.

In the energy eigenstate representation the basis states of an em. field are the number states $|n\rangle$ with $n = 0, 1, 2, ...$ denoting the number of microwave photons in the respective modes. The eigenstates of the spin-system ($|g\rangle$,$|e\rangle$) have already been introduced. The complete state of the system should be specified via the states of both, the electromagnetic field and the spin-system. The unperturbed eigenstates, thus eigenstates of H_0, are $\{|g, n+1\rangle, |e, n\rangle$. The eigenvalues of H_0 are the following:

$$H_0|g, n+1\rangle = \hbar(\omega_\mathrm{r}(n+1) - \frac{\omega_\mathrm{s}}{2})|g, n+1\rangle \tag{4.17}$$

$$H_0|e, n\rangle = \hbar(\omega_\mathrm{r} n + \frac{\omega_\mathrm{s}}{2})|e, n\rangle. \tag{4.18}$$

For $\omega_\mathrm{r} = \omega_\mathrm{s}$ the eigenvalues are equal and the eigenstates of H_0 therefore degenerate. Including the interaction term H_int will lift the degeneracy. Since H_int couples only $|g, n+1\rangle$ to $|e, n\rangle$ the 4 matrix elements of H_JC can be written in the following form

$$H_\mathrm{JC} = \hbar\omega_\mathrm{r}(n + \frac{1}{2}) \begin{pmatrix} 1 & 0 \\ 0 & 1 \end{pmatrix} + \frac{\hbar}{2} \begin{pmatrix} \delta & 2\mathrm{g_s}\sqrt{n+1} \\ 2\mathrm{g_s}\sqrt{n+1} & -\delta \end{pmatrix}. \tag{4.19}$$

The eigenvalues of the above matrix are

$$E_\pm = \hbar\omega_\mathrm{r}(n + \frac{1}{2}) \pm \frac{\hbar}{2}\sqrt{\delta^2 + 4\mathrm{g_s}^2(n+1)} \tag{4.20}$$

with the detuning $\delta = \omega_\mathrm{s} - \omega_\mathrm{r}$. The corresponding eigenstates, called *dressed* states, are superpositions of the so-called *bare* states ($|g, n+1\rangle$,$|e, n\rangle$):

$$|+\rangle = \cos\theta|e, n\rangle + \sin\theta|g, n+1\rangle, \tag{4.21}$$

$$|-\rangle = -\sin\theta|e, n\rangle + \cos\theta|g, n+1\rangle, \tag{4.22}$$

with the mixing angle

$$\cos\theta = \frac{2\mathrm{g_s}\sqrt{n+1}}{\sqrt{(\sqrt{\delta^2 + 4\mathrm{g_s}^2(n+1)} - \delta)^2 + 4\mathrm{g_s}^2(n+1)}}. \tag{4.23}$$

The spectrum of the eigenstates $E_\pm$ (Eq. 4.20), as one can see also in Fig. 4.4, is caused

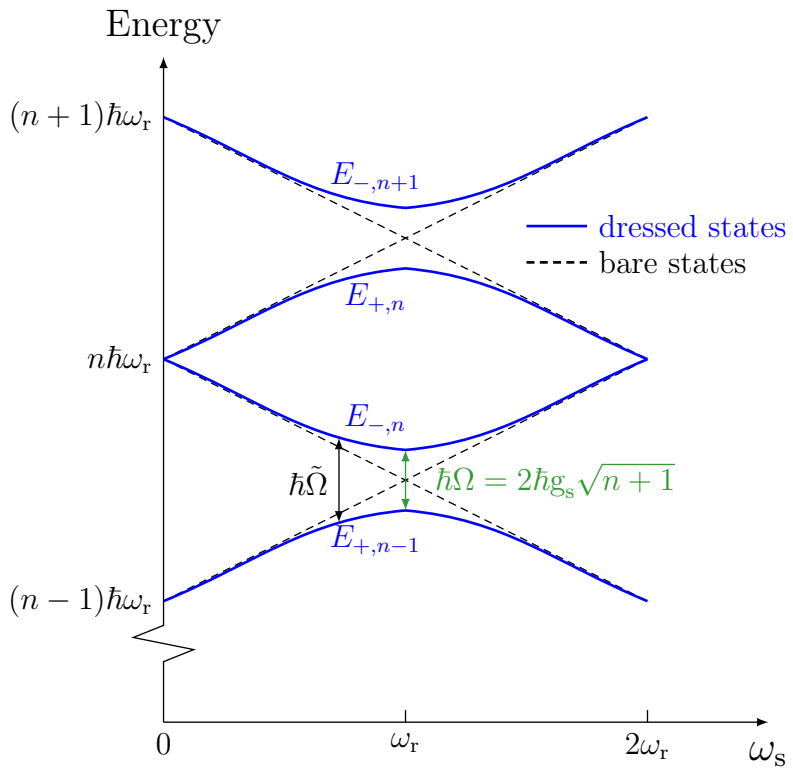

Figure 4.4.: Energy levels of the dressed (avoided crossing) and bare (no coupling) states versus ω_s for different n subspaces.

by the detuning δ of the spin-system from the resonator.

Without interaction the bare states cross at the condition $\omega_r = \omega_s$ (see black dashed lines in Fig. 4.4). The coupling lifts this degeneracy and leads to a phenomena that is commonly called *avoided crossing* or *normal mode splitting*, respectively (see Fig. 4.3, 4.5). The splitting $E_{+,n} - E_{-,n}$ scales with $\sqrt{n+1}$. Expressed in terms of frequency, the splitting for $\delta \neq 0$ is called the generalized Rabi frequency

$$\tilde{\Omega} = \sqrt{\delta^2 + 4g_s^2(n+1)}. \tag{4.24}$$

This term describes basically the exchange rate of excitation between the resonator and the spin-system. If the detuning becomes much bigger than the coupling, thus the ratio δ/g_s increases, the mixing angle $\theta \to 0$ and the system becomes decoupled and the eigenstates are again the bare states.

In the the case of $\delta = 0$ the resonator and the spin-system are tuned in resonance, thus

$\theta = \pi/4$ and therefore $\sin\theta = \cos\theta = \frac{1}{\sqrt{2}}$ and the eigenstates become

$$|\pm\rangle = \frac{1}{\sqrt{2}}[|e,n\rangle \pm |g,n+1\rangle] \tag{4.25}$$

and the eigenvalues

$$E_\pm = \hbar\omega_\mathrm{r}\frac{1}{2} \pm \hbar\mathrm{g_s}\sqrt{n+1}. \tag{4.26}$$

For this special case of zero detuning the degeneracy of the symmetric $|+\rangle$ and the antisymmetric eigenstates $|-\rangle$ is lifted by the factor $2\mathrm{g_s}\sqrt{n+1}$ and $\tilde{\Omega} \to \Omega$, reaching its minimum, with the Rabi frequency

$$\Omega = 2\mathrm{g_s}\sqrt{n+1}. \tag{4.27}$$

A crucial point with respect to quantum mechanics is the circumstance that there is a splitting even if the photon number $n = 0$ in the one excitation manifold. For $n = 0$ and $\delta = 0$ the splitting is called *vacuum Rabi splitting* and its magnitude is

$$E_{+,0} - E_{-,0} = 2\hbar\mathrm{g_s}. \tag{4.28}$$

There is no classical analogue for the vacuum Rabi splitting since the vacuum field is a purely quantum effect [**Fox06**].

4.2.2. Tavis-Cummings model: coupling to an ensemble of NV^- centres

The coupling strength of a single NV^- centre $\mathrm{g_s}$ to an electromagnetic mode is not strong enough to permit coherent exchange of excitations. In the following it will be shown that the coupling to an ensemble of N single NV^- centres is enhanced by the factor $\sqrt{N}$ resulting in a collective coupling strength $\mathrm{g_{col}}$ that originates from a coherent superposition of spin excitations [Wes09].

In the previous section we discussed the coupling of n photons to a single NV^- centre. This is basically the opposite of what we have in the experiment, namely NV^- centres on the order of 10^{12} and compared to it, a few microwave photons in the resonator. Given a ratio of n/N on the order of 10^{-8} we will set $n = 0$ in the further discussion and thereby

make a first approach towards the real conditions of the experiment. This step will be legitimated afterwards, when the critical photon number n_0 will be introduced. To do that, we have to consider losses of the systems that have not been included in the model so far. Indeed, the consideration of losses will be the second approach towards an almost realistic model of the experiment.

Coupling to an ensemble of two-level systems is described by the Tavis-Cummings Model (TCM):

$$H_{\mathrm{TC}} = \hbar\omega_{\mathrm{r}} a^\dagger a + \frac{\hbar}{2}\omega_{\mathrm{s}} \sum_j \sigma_z^j + \hbar \sum_j \mathrm{g}_{\mathrm{s},j}(\sigma_+^j a + \sigma_-^j a^\dagger). \tag{4.29}$$

The coupling term already indicates that a single excitation in the resonator is coupled to a coherent superposition of spin excitations (a spin wave) [Kub10]. For an ensemble of two-level spin-systems the ground state is

$$|\Psi_g\rangle = |g, g, g, ...\rangle \tag{4.30}$$

whereupon the first excited state is a superposition of N states each with one excitation:

$$|\Psi_e\rangle = \frac{1}{\sqrt{N}} \left(|e, g, g, \dots\rangle + |g, e, g, \dots\rangle + \cdots + |g, g, \dots, e\rangle\right) \tag{4.31}$$

The Hamiltonian H_{TC} couples only the states $|\Psi_e\rangle|0\rangle$ with the $|\Psi_g\rangle|1\rangle$, therefore the transition matrix element is

$$\begin{aligned}
&\langle 1|\langle\Psi_g|H_{\mathrm{TC}}|\Psi_e\rangle|0\rangle = \langle 1|\langle\Psi_g|\hbar\sum_{j=1}^{N} \mathrm{g}_{\mathrm{s},j}\sigma_-^j a^\dagger|\Psi_e\rangle|0\rangle \\
&= \langle 1|\langle g, g, g, \dots|\hbar\sum_{j=1}^{N} \mathrm{g}_{\mathrm{s},j}\sigma_-^j a^\dagger \frac{1}{\sqrt{N}} \left(|e, g, g, \dots\rangle + |g, e, g, \dots\rangle + \cdots + |g, g, \dots, e\rangle\right)|0\rangle \\
&= \hbar\frac{1}{\sqrt{N}}\sum_{j=1}^{N} \mathrm{g}_{\mathrm{s},j}.
\end{aligned} \tag{4.32}$$

If we assume that all spins of the ensemble couple with the same individual coupling strength $\mathrm{g_s}$, thus $\mathrm{g}_{\mathrm{s},j} = \mathrm{g_s}\forall j$ the expression $\sum_{j=1}^{N} \mathrm{g}_{\mathrm{s},j} \to N\mathrm{g_s}$. With this approach the matrix transition element described in Eq. 4.32 becomes

$$\langle 1|\langle\Psi_g|H_{\mathrm{TC}}|\Psi_e\rangle|0\rangle = \hbar\sqrt{N}\mathrm{g_s}. \tag{4.33}$$

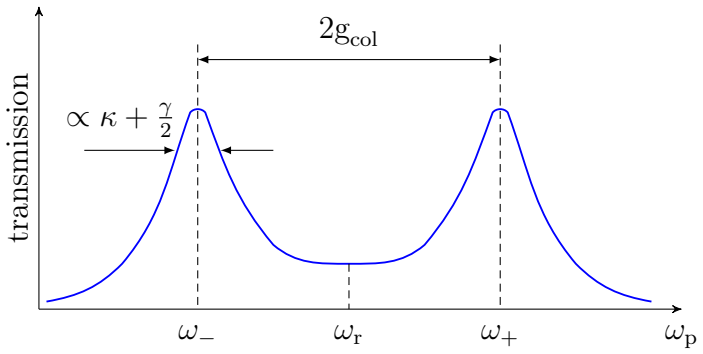

Figure 4.5.: Transmission for $\omega_r = \omega_s$ (degeneracy point) is plotted. The width of the resonances are determined/broadened by the losses of the two coupled oscillators κ and γ. The coupling strength g_{col} determines the distance between the two peaks.

If we compare this expression with the transition matrix element from Eq. 4.19 (with $n = 0$) we could introduce an effective collective coupling constant

$$g_{col} = g_s\sqrt{N} \tag{4.34}$$

and get similar expression for the eigenenergies compared to the JCM (see Eq. 4.20):

$$E_\pm = \frac{\hbar\omega_r}{2} \pm \frac{\hbar}{2}\sqrt{\delta^2 + 4g_{col}^2}. \tag{4.35}$$

With collective coupling we mean that all NV$^-$ centres interact constructively with the magnetic field mode $\mathbf{B}(\mathbf{r}, t)$ of the resonator. Furthermore we assume that the NV$^-$ centres do not couple to each other.
If we insert the relation $g_s \propto \sqrt{\frac{1}{V_{mod}}}$ in Eq. 4.34, another insight is gained:

$$g_{col} \propto \sqrt{\frac{1}{V_{mod}}}\sqrt{N} = \sqrt{\rho} \tag{4.36}$$

with the NV$^-$ density ρ. Hence shrinking the mode volume increases the individual coupling strength but does not effect the collective coupling strength. It might have different advantages to couple to less spins but individually stronger than to more spins and individually weaker, particularly with respect to loss mechanisms and the effect of inhomogeneous broadening.

Holstein-Primakoff approximation A single NV$^-$ centres as it was introduced in Sec. 3.1 can be used as an effective two-level system. An ensemble of such systems

on the contrary behave as a collection of harmonic oscillators under the assumption of high polarisation [Kur11], that in our case is achieved by thermal equilibration at a cryogenic operating temperature. In other words, if the number of excitations (a spin wave) is small compared to the number of single two-level systems N, this spin wave behaves as a harmonic oscillator [Kub10]. This kind of bosonization that can be achieved by a mapping from the angular momentum operator σ_z of a two-level system to boson creation and annihilation operators is conveniently described in the Holstein-Primakoff approximation. As an important consequence the excitations become independent (non-interacting) quasi particles. This implies that the dynamics of a single excitation provides the general solution, even if the total number of excitations is actually much larger than unity but still much smaller than N [Kur11].

4.2.3. Coupling regimes

Coupling between the NV$^-$ ensemble and the resonator basically always takes place. Above all with respect to the exchange of excitations, there are two regimes defined, a weak coupling and a strong coupling.

In this section the conditions that determine whether a system is in the strong or the weak coupling regime will be launched. In the quantum mechanical description no losses of the systems have been considered so far therefore the exchange of excitations would not be time-limited.

Consideration of losses in principle will limit temporally the exchange of excitations or even prevent it.

The losses of the resonator can be described via κ (see Eq. 2.8) and the losses of the spin-system preliminary by the parameter γ. The loss described by γ mainly refers to the decay of the spin excitations in modes other than the resonator mode and refers to the width of the spin resonance curve (experimentally we only have access to the resonator transmission, therefore it is not possible for us to measure γ directly). γ in the models we use in Chap. 6 consists of two parts, the homogeneous broadening γ_0 and the inhomogeneous broadening γ_{inh}. The homogeneous broadening refers basically to the decay rate of a single NV$^-$ centre which is mainly influenced by electron paramagnetic impurities in

the lattice [Jel06]. The inhomogeneous broadening refers to the decay rate of an ensemble of NV^-. This additional broadening is due to the fact, that the ESR of the single NV^- centre are not identical but spread around a centre frequency. The spontaneous decay (population reducing de-phasing processes) time T_1 of the diamond we used in the experiments was on the order of $\approx 44\,s$ [Ams11]. In our case losses on this time scale are negligible since γ in our diamond sample is on the order of several MHz (see Chap. 6). The coherence time therefore is limited by population conserving de-phasing processes. Note also that γ unlike κ is mostly related to the FWHM.
Depending on the ratio of the coupling strength g_{col} and the losses γ and κ there are two different coupling regimes.
$\mathbf{g_{col} < [\gamma/2, \kappa]}$ **weak coupling:** losses are bigger than the coupling strength, the spin excitation is lost even before an exchange could have happened.
$\mathbf{g_{col} > [\gamma/2, \kappa]}$ **strong coupling:** photon can at least hop a few times between the spin-system and the resonator.

As already mentioned, γ in our case refers to the width of an inhomogeneously broadened spin distribution. However, this means that in the above given definition of the coupling regimes only the width γ of such a distribution is considered. There are several publications about theoretical investigations on the influence of the width and the shape of such a distribution with respect to the dynamics of the coupling. They emphasize that apart from the width, the coherence depends crucially on the shape of the distribution, in particular on decay of its tails ([Din11],[San12],[Kur11]).
So far various *couplings* have been introduced. To prevent any upcoming confusion:
over-, under- and critically-coupled refers to the coupling of a resonant structure to a feed line while strong and weak coupling characterises the two possible coupling regimes of two resonant systems, respectively.

Critical numbers and cooperativity In addition to the above given definitions of strong and weak coupling regimes there are the dimensionless critical atom and photon numbers N_0 and n_0 that allow a characterisation of the coupling regimes:

the critical photon number [Kim98]

$$n_0 = \frac{\gamma^2}{8g_{col}^2} \tag{4.37}$$

and the critical atom number

$$N_0 = \frac{\gamma\kappa}{g_{col}^2}. \tag{4.38}$$

Both parameters are a measure of the impact that a single photon and a single atom have on the interaction. For instance for $(n_0, N_0 \gg 1)$ one photon or atom more or less is of no consequence since the coupling is weak. Whereas $(n_0, N_0 \ll 1)$ indicates the strong coupling regime. The critical numbers of the experiments described in Chap. 5 are well below one. As a consequence the photon number n can be set to zero as it was done at the beginning of Sec. 4.2.2 since we are in the regime were single photons play an essential role.

The cooperativity [Kim98]

$$C = N_0^{-1} = \frac{g_{col}^2}{\gamma\kappa} \tag{4.39}$$

finally indicates the coupling regimes by $C > 1$ (strong coupling) and $C < 1$ (weak coupling).

4.2.4. Coupling in time domain

In the following expressions will be introduced that can be used to describe the dynamics of the resonator transmission in the time domain.

An indication for a strong coupling regime in spectroscopy is the appearance of two peaks in the transmission of the resonator (Fig. 4.5) whereas this kind of splitting of the resonance curve for a system in the weak coupling regime does not occur. These phenomenon correspond to oscillations (strong coupling, see Fig. 5.15b) and a decay (weak coupling, see Fig. 5.13a) of the resonator transmission in time domain. The oscillations with the period π/g_{col} are due to the coherent exchange of excitations between the resonator and the spin ensemble.

From the Heisenberg equations of motion in the frame rotating with the probe frequency

ω_p one can yield the following expression for the time derivation of the annihilation operators a and σ_- [San12]:

$$\langle \dot{a} \rangle = -(\kappa + \mathrm{i}\Delta_\mathrm{r})\langle a \rangle - \mathrm{i}g_\mathrm{s} N \langle \sigma_- \rangle + \eta, \tag{4.40}$$

$$\langle \dot{\sigma}_- \rangle = -(\frac{\gamma}{2} + \mathrm{i}\Delta_\mathrm{s})\langle \sigma_- \rangle - \mathrm{i}g_\mathrm{s}\langle a \rangle \tag{4.41}$$

with $\Delta_\mathrm{r} = \omega_\mathrm{r} - \omega_\mathrm{p}$ and $\Delta_\mathrm{r} = \omega_\mathrm{s} - \omega_\mathrm{p}$ and η accounting for the drive of the resonator. A simplified expression for the steady state can be obtained from the Eqs. 4.40 and 4.41 by solving $\langle \dot{a} \rangle = \langle \dot{\sigma}_- \rangle = 0$:

$$\langle a \rangle_\mathrm{st} = \frac{\eta}{\kappa + \mathrm{i}\Delta_\mathrm{r} + \frac{g_\mathrm{s}^2 N}{\frac{\gamma}{2} + \mathrm{i}\Delta_\mathrm{s}}}. \tag{4.42}$$

$\langle a \rangle$ is proportional to the transmission $t(\omega_\mathrm{p})$ which is plotted in Fig. 4.5 for the degenerated case of $\omega_\mathrm{r} = \omega_\mathrm{s}$. One can see that κ and γ determine the broadening of the peaks and the coupling strength $g_\mathrm{s}^2 N = g_\mathrm{col}^2$ the distance between the two peaks.

4.3. Coupling NV$^-$ centres to a resonator: realisation

The NV$^-$ centres can be coupled to the resonator mode via their magnetic dipole moments. The diamond that contains the NV$^-$ centres therefore has to be placed within the reach of the magnetic field of the resonator mode. For a half wave resonator with the corresponding boundary conditions $Z_\mathrm{L} = \infty$ the electromagnetic field along the resonator is distributed such that the maximum of the magnetic field is located in the middle whereas the electric field is maximum at the ends. As a consequence the most promising place for the diamond is in the middle of the resonator (see Fig. 3.2). The diamond was such positioned that its (001) crystallographic plane was facing the resonator surface. The resulting influences on the resonator properties are very different. First of all there is a small shift of the resonance frequency due to the deviation of the diamonds dielectric constant ϵ_r from 1. From Eqs. 2.10, 2.11 one can see that an increasing effective dielectric constant ϵ_eff leads to a decreasing resonance frequency. ϵ_eff depends on the geometry of the resonant structure and on the relative permittivities of the surrounding materials.

Without diamond there is vacuum above the resonant structure and sapphire substrate below. The diamond on top increases ϵ_{eff} and shifts the resonance frequency a few MHz downwards. But this does not have any effect on the experiment provided that the resonator and the NV$^-$ ESR frequency become resonant.

A rather dramatic change happens to the Q-factor of the resonator since the diamond

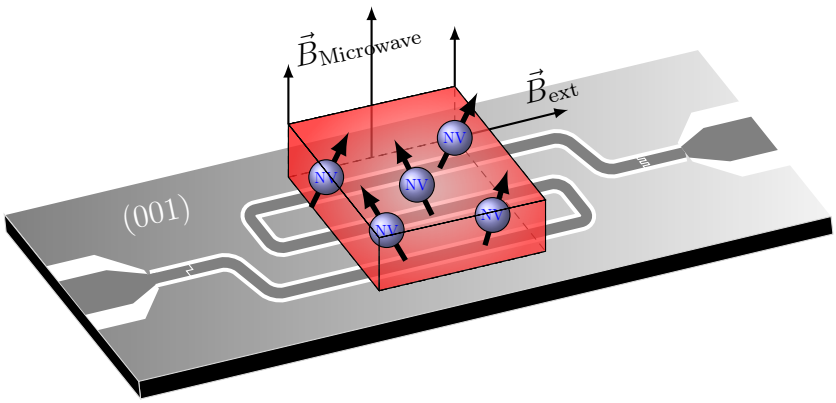

Figure 4.6.: For the coupling experiment the diamond is put on top of the resonator and as accurately as possible (with visual judgement) in the centre, where the magnetic field of the microwave is maximum. The figure shows basically the content of the sample box. Not drawn are the Helmholtz coils that surround the sample box.

provides apparently new loss channels. The pure resonators (without diamond on top) we use for the coupling have a rather high Q_{int}, thus they are over coupled since they are limited by the external coupling factor Q_{ext}. As the diamond lowers Q_{int} dramatically, the resonator becomes under coupled.

For the half wave resonator and the diamond we used so far, the number N of single NV$^-$ centres we couple to, is on the order of 10^{12}. The measured collective coupling strength $g_{\text{col}}/(2\pi) = g_s\sqrt{N}/(2\pi)$ is around 12 MHz. This results in a single coupling strength $g_s/(2\pi)$ of approximately 12 Hz.

To have well defined boundary conditions the resonator with the diamond on top (shown in Fig. 4.6) is put in a sample box (see picture in App. B). The diamond becomes fixed by a pogo pin (see Fig. 5.2) that is mounted on the lid of the sample box.

5. Experimental setups and results

When I joined the experiment there was already a working setup to carry out spectroscopic measurements (Fig. 5.2). This setup permitted to characterise new resonator designs and furthermore allowed to couple a spin-system to the electromagnetic field of a resonator. Over time, a second setup in paralell was installed that opened a new door towards measurements in the time domain (Fig. 5.10). The following chapter that covers parts of the experimental work during my time as diploma student is divided into two sections, one that includes the spectroscopic and one that contains the time domain measurements.

5.1. Spectroscopic measurements

In spectroscopy the frequency response of the experiment in its steady state which is reached after a very short transient time (few ns, see Fig. 5.15) is measured. Basically the probe frequency is swept over the frequency range of interest and the transmission parameter S_{12} (see App. A) through the coupled spin ensemble-resonator system is measured.

5.1.1. Experimental setup

In Fig. 5.2 a simplified experimental setup is drawn. In the following the main components of the setup will be briefly introduced. Furthermore the results of a measurement are shown, that was carried out to investigate the temporal stability of the magnetic fields that were used to tune the ESR of the NV^- centres.

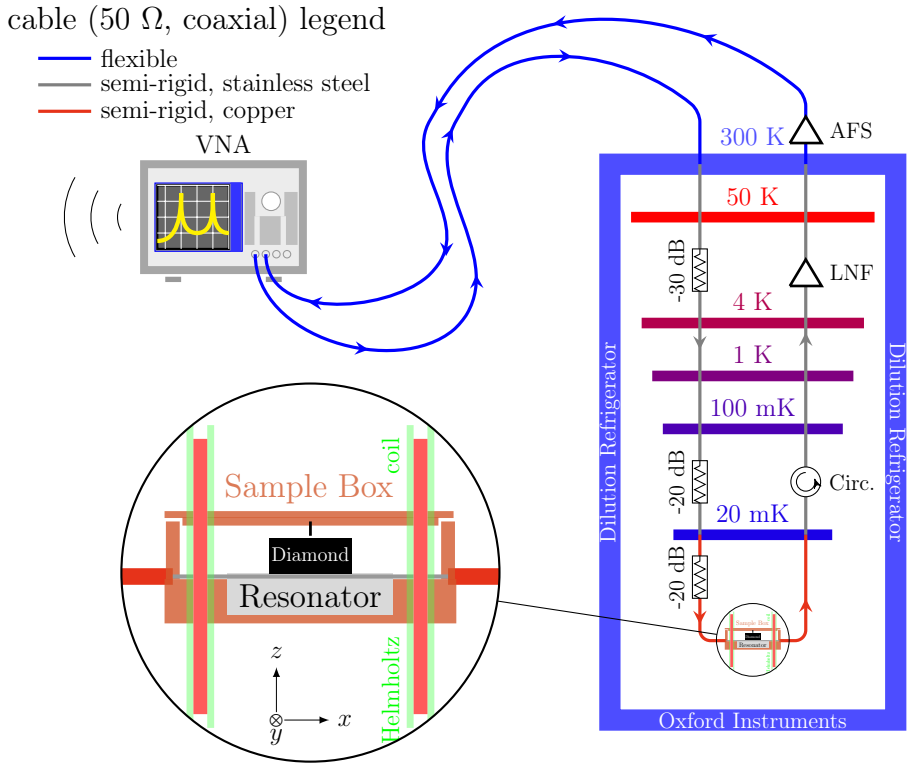

Figure 5.1.: Schematic scheme of the experimental setup used in a spectroscopy measurement

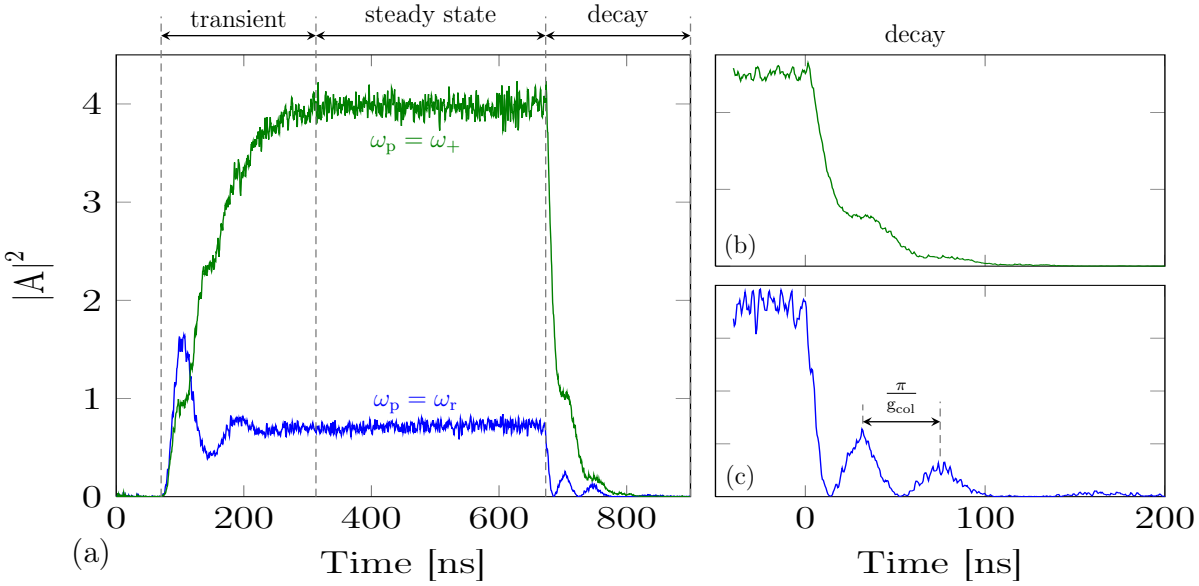

Figure 5.2.: Schematic scheme of the experimental setup used in a spectroscopy measurement

Dilution refrigerator One of the many hearts of the experimental setup was a dilution refrigerator (DR) from Oxford instruments, a cryogenic device that provided the low temperatures we needed for the experiment ($< 100\,\mathrm{mK}$). With respect to the superconducting resonators the operating temperature T has to meet the following relations: $k_B T \ll \hbar\omega_\mathrm{r} \ll \Delta$, with the Boltzmann constant k_B, the reduced Planck constant $\hbar$ and the energy gap of the superconducting material Δ [Dev04]. The condition $k_B T \ll \hbar\omega_\mathrm{r}$ is necessary to keep the population of thermal photons in the resonator as low as possible. The requirement $\hbar\omega_\mathrm{r} \ll \Delta$ is important to keep dissipative losses as low as possible.
Very low temperature are also necessary to initialize the spin-system or rather to polarize the NV^- centres into their ground state ($m_s = 0$).
The DR we used was pre-cooled by an integrated pulse tube refrigerator to around 4 K. As one can see in Fig. 5.2, there are several different temperature stages inside the DR, each one with a radiation shield (not shown in Fig. 5.2). The microwave cables and wires had to be anchored properly at each of the different temperature platforms in order to get cooled.
The cryogenic fluid in a DR is a mixture of the two helium isotopes ^{4}He and ^{3}He. Below 867 mK the mixture undergoes a phase separation to form a ^{3}He-rich phase (concentrated phase) and a ^{3}He-poor phase (the dilute phase). ^{3}He atoms in the dilute phase act as a gas: forcing a flux of ^{3}He atoms from the concentrated phase to the dilute one, a process analogous to the evaporation of a liquid is obtained [Ven08]. This process basically cools the resonator and the diamond down to around 20 mK (see Fig. B.2).
The big advantage of using a DR is that it can continuously maintain temperatures as low as a few mK which has to be compared with *one shot* refrigerators as e.g. adiabatic demagnetisation refrigerators.
The cool down process from ambient temperature to around 20 mK took around 28 hours.

Vector network analyzer (VNA) Network analyzers are used to measure the S-parameters, thus reflection and transmission of an electrical network. A VNA is both a signal generator that provides the test signal and receivers to collect the measurement data. The receiver measures complex amplitudes thus the magnitude and the phase of a signal. The one we used for spectroscopy measurement is a E5071c from Agilent Technologies with a

frequency range from 300 kHz to 20 GHz. The ports of the VNA have an impedance of 50 Ω to avoid any reflections. Therefore the transmission parameter $S_{21} = |V_2/V_1|^2$ where V_2 is the voltage measured at the input port of the VNA and V_1 the voltage applied at the output port of the VNA.

Microwave cables The microwave line consisted of different shielded coaxial cables. Outside the DR we employed flexible cables from Mini Circuits. Inside the DR we used semi rigid cables that were bent between the different temperature stages in order to avoid mechanical stress on the connectors. Furthermore stainless steel microwave cables were installed to the lowest temperature stage (20 mK) to suppress as much heat transfer as possible between the different temperature stages. Since the sample box (see Fig. 5.2) that contained the resonator and the diamond was cooled by the lowest temperature stage via the microwave line and additional braces, we used copper cables in order to support any heat transfer.

The pure coaxial cables as we bought them had an impedance of 50 Ω. In order to get them ready for use in the experiment they had to be cut into length, equipped with connectors and bent. These steps of the cable preparation process had to be carried out very carefully, since any deviations from the 50 Ω lead to reflections of the signal.

Attenuators, circulators, amplifiers The power of the signal from the VNA can be varied from 10 dBm to -85 dBm whereupon 0 dBm refers to the power of 1 mW. If one varies the power of the output, one changes the amplitude of the signal but does not lower the noise level. In order to get a low power signal to the experiment it is not enough to lower the output of the VNA signal. Attenuations within the cryostat are necessary in order to achieve an attenuation of the signal parallel to the lowering of the noise floor by the decreasing temperature.

After the signal has left the experiment it has to pass a circulator on the way out. The circulator does not effect the signal but redirects any reflections into a port terminated with 50 Ω.

The first amplification of the signal after it passed the sample box is a very crucial point. An amplification right after the output of the sample box would be ideal with respect to

the signal to noise ratio (SNR). Due to the heat load of the amplifier and the lower cooling power of the lower temperature stages the first amplifier (LNF)[1] is mounted on the 4 K stage (see Fig. 5.2). What could help to increase the SNR is to replace the stainless steel coaxial cable till the LNF amplifier with superconducting coaxial cables. This is actually planned to happen in the near future. On top of the DR the signal is again amplified (AFS)[2] at room temperature. In total, the amount of signal attenuation (-60 dB from attenuators plus ≈ -9 dB from cable losses) on the way down is comparable to the total amplification on the way out.

Helmholtz pair The superconducting Helmholtz pairs are necessary in order to apply nearly uniform magnetic fields on the diamond. With these pairs of coils one can produce the external magnetic fields that are necessary to tune the ESR frequency of the NV^- centres via the Zeeman effect. Apart from the ESR tuning, the Helmholtz coils can be used to study the influence of external magnetic fields on the resonator properties (see Sec. 5.1.2.1)

We had three measurement stations cooled by the lowest temperature stage of the DR. One station were we could install a Helmholtz pair on demand to produce a magnetic field in z-direction, a second station with a two-dimensional coil set for magnetic fields in the xy-plane (parallel to the (001) crystal plane of the diamond) and a third station with a new three-dimensional coil set to apply magnetic fields in any arbitrary direction (see Fig. B.3).

The superconducting wire we used for the coils was basically a copper matrix with NbTi filaments. The idea of the new set of Helmholtz pair (see Fig. B.4) was not only to have it in three-dimensions but also to have more windings and to solder it to the normal conducting feed line already at the 4 K stage of the DR in order to be able to run the coils with higher currents or rather to apply higher magnetic fields on the experiment. The conversion factor Ampere/Gauss was different for each pair of coils but roughly on the order of $5 \times 10^{-3}\,\mathrm{A\,G^{-1}}$.

The diameter of the wire was only 79 µm and the number of windings of a single coil was

[1] LNF-LNC1.8-2.8 Low noise factory

[2] AFS3-02000400-08-CR-4, Miteq

800. One can imagine that the manual coil winding process and the installation of the three-dimensional construction in the DR was a quite delicate work.

5.1.1.1. Temporal stability of the magnetic fields

Magnetic coils in general are high inductive loads for the current drive source and might compromise the temporal stability of the magnetic fields. However, the stability of the magnetic fields is of high importance, since fluctuations or a drift detunes the NV^- centres from the resonator frequency and causes new loss mechanisms.

We found that the temporal stability of the driving current (magnetic field) primarily depended on the power supply itself and secondly on the operation mode (constant current (CC), constant voltage (CV)). Manufacturers of power supplies recommend the use of the

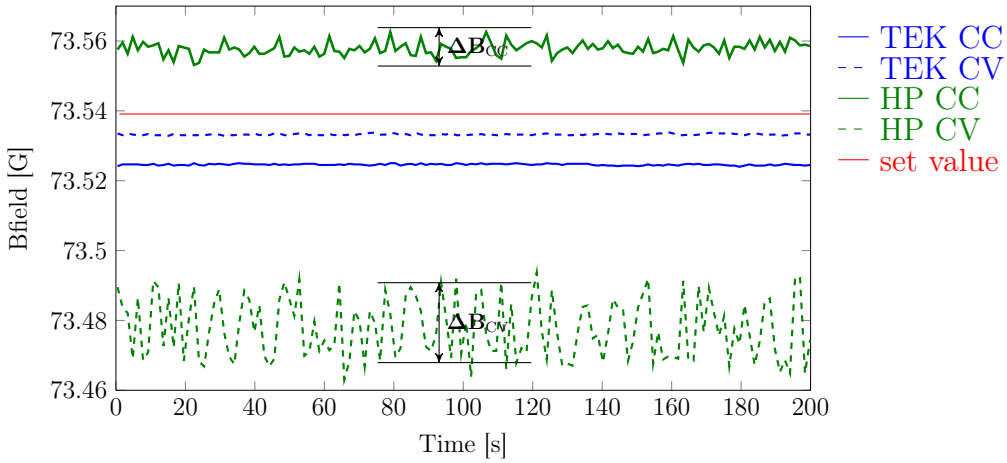

Figure 5.3.: The figure shows a measurement that was carried out to investigate the temporal stability of different power supplies with superconducting Helmholtz coils as load.

CV mode when controlling inductive loads. However, the output voltage of a power supply for magnetic fields in the range of 200 G is only around 0.1 V. This voltage drop is due to the normal conducting supply lines of the coils. To obtain better conditions for the level control the output voltage can be shifted towards a more balanced region, e.g. to the middle of the voltage modulation range of the power supply. This can be achieved by putting a resistor in the normal conducting supply lines to create an additional voltage drop.

In order to shift the voltage for different amperages to a balanced range we mounted four different power resistors (6 Ω, 20 Ω, 100 Ω, 120 Ω) on top of a heat sink.

Fig. 5.3 shows the temporal magnetic field stability of two different power supplies. The stability is shown for a value (around 73 G) that is representative for the magnitude of the magnetic field that is necessary to tune the NV^- into resonance with the resonator frequency. Furthermore, the time scale is comparable with the duration of a typical spectroscopic measurement (1601 frequency points and a band width of 10 Hz).

The two power supplies that have been compared were on the one hand a PWS4205 (5 A, 20 V) from Tektronix and on the other hand a 6611C (5 A, 8 V) from Hewlett Packard. Measurements in CV mode were carried out with an additional power resistor in the line. Since the voltage range of the two power supply is different, we used different resistors. That means we did not test them under the exact same conditions, however, under those conditions under which we would use them in the experiment.

The results clearly demonstrated that the Tektronix (TEK) power supply was preferable in any point. In CV mode the accuracy of the TEK power supply was better compared to the CC mode (closer to the red line in Fig. 5.3 that depicts the set value), however, a very small and negligible drift of the magnetic field was observable. Possibly due to increasing resistance which in CV mode is compensated by a decreasing current that finally would lead to a drift of the magnetic field. The fluctuations of the magnetic field were almost in the same order of magnitude for both the CC and CV mode and clearly negligible for our purposes.

The Hewlett Packard (HP) power supply behaved more or less the opposite. Higher accuracy in CC mode and higher fluctuations in CV mode. Since the HP was the power supply used so far in the experiment we wanted to estimate the effect on the ESR of NV^- centres caused by the fluctuations of the magnetic field (ΔB in Fig. 5.3). To conclude, ΔB_{CC} as well as ΔB_{CV} lead to changes of the ESR on the order of a few kHz and therefore are negligible compared to the inhomogeneous broadening in the range of 15 MHz (see Sec. 6.0.4.3). Nevertheless, we exchanged the HP for the TEK power supply since it showed a much better performance with respect to temporal stability.

5.1.2. Results of spectroscopic measurements

Spectroscopic measurements were carried out with a VNA, basically according to the setup that is shown in Fig. 5.2. The measurements that are going to be discussed in the following cover the response of a resonator to a perpendicular magnetic field (z-direction), strong coupling of an ensemble of NV^- centres to different resonator types and a measurement that shows the power dependence of the coupling strength.

5.1.2.1. Resonators in an external magnetic field

Important parameters of a superconducting resonator like the quality factor Q and the resonance frequency ω_r are sensitive among other things to the temperature and to external magnetic fields [Fru05][Hea08]. The tuning of the NV^- centres leads to the fact that, not only the diamond is located in an external magnetic field, but the resonator too. The so far installed Helmholtz coils only allowed to apply magnetic fields parallel to the resonator chip surface (xy-plane, see Fig. 5.4).
With the new installed three-dimensional Helmholtz coil set it became possible to investigate also the effect of perpendicular magnetic fields (z-direction) on the resonator.
The crucial parameter in the study of the resonator response to a magnetic field is the kinetic inductance L_k. The crucial effect, however, is the magnetic flux focusing in the gaps between the ground planes and the central conductor that leads to effective local fields that are much larger than the applied field. This focusing of the field is based on the Meissner effect (expulsion of a magnetic field from a superconductor). Since the resonator chip area perpendicular to the z-direction is much larger than the area perpendicular to the xy-plane, the focusing effect on a magnetic field that points in z-direction is supposed to be much larger.
Indeed, any effects caused by fields parallel to the resonator chip surface are very small which was pointed out in [Kol12]. That this is not the case if the field is perpendicular to the resonator chip surface will be shown in what follows.
In general the inductance has two contributions: a geometric (temperature independent) inductance L_m and a kinetic (temperature dependent) inductance L_k.
An external magnetic field B_{ext} at the surface of a superconductor decays exponentially

with the London penetration depth λ_L, which depends on the density of the superconducting charge carriers n_s. They, in turn, depend on the temperature.
The shielding supercurrent that flows in an area that is characterized by λ_L carries a significant amount of kinetic energy of the superconducting charge carriers. This generates the kinetic contribution L_k to the total inductance L. In order to find a magnetic field

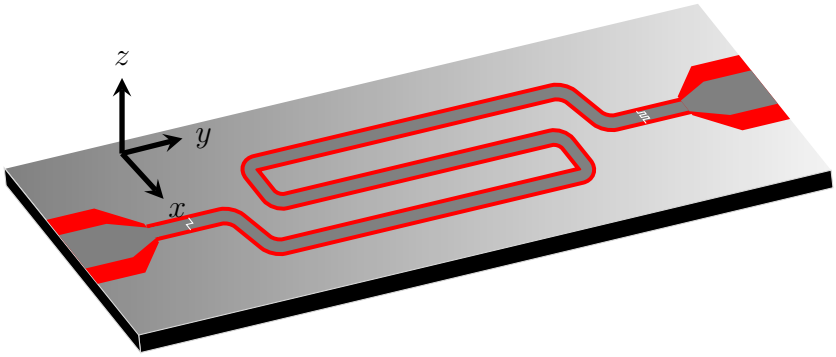

Figure 5.4.: The red marked areas in the figure indicate the gaps between the center conductor and the ground plane. If the magnetic field points into the z-direction, the flux, expelled from the superconducting parts (gray) gets focused in the red marked gaps.

dependency of the penetration depth λ_L one has to consider non-linear London equations. In [Yip92] they derived an expression for non-linear effects and showed that the dependency of the effective penetration depth λ_{eff} with respect to temperature and magnetic field can be sketched as follows:

$$\lambda_{\text{eff}}(T, B_{\text{ext}})^{-1} = \lambda_{\text{L}}(T)^{-1}\Big\{1 - \frac{1}{3}\alpha(T)\Big[\frac{B_{\text{ext}}}{B_0(T)}\Big]^2\Big\}. \tag{5.1}$$

Here, $B_0 \sim B_c$ was assumed with B_c being the critical magnetic field of the superconductor and α some material specific parameter. One can see that λ_{eff} increases with increasing B_{ext}. In [Goe08] the kinetic inductance L_k scales with λ_{L}^2, therefore the same relation should hold also for the effective penetration depth λ_{eff} and the kinetic inductance of a superconducting layer with thickness h and $h > \lambda_{\text{eff}}$:

$$L_k \propto \lambda_{\text{eff}}^2. \tag{5.2}$$

To find out the effect on the resonance frequency ω_{r} we can make use of Eq. 2.5:

$$\omega_{\text{r}} = \frac{1}{\sqrt{LC}} = \frac{1}{\sqrt{(L_m + L_k)C}}. \tag{5.3}$$

From this equation one expects a quadratic decrease of the resonance frequency with increasing external magnetic field B_{ext}. For the measurements that are described in the following we used an under-coupled ($Q_{\mathrm{L}} = 813\,000$) half wave resonator with a resonance frequency $\omega_{\mathrm{r}}/(2\pi)$ of 6.846 GHz.

Reversible regime Fig 5.5a shows a measurement in which we applied the field perpendicular to the resonator chip surface. The magnetic field was increased slowly and in small steps (up to 2.5 G). Slowly, because too fast ramping of the magnetic field causes vortices being trapped in the resonator film. Actually a similar effect to what we expect once the irreversible hysteretic regime is reached.
Increasing the magnetic field, indeed, we observed a non-linear shift of ω_{r} towards lower frequencies. However, the best fit of the data was not achieved with a 2nd but with a 4th order polynomial function. This was probably due to correction terms of higher order that were not considered in Eq. 5.1. Within the range of ± 2.5 G no hysteretic effects appeared as one can see in Fig. 5.5a. This was also confirmed by a constant quality factor Q_{L}.

Irreversible regime As niobium is a typ II superconductor first hysteretic effects are expected when the effective magnetic field becomes equal to the first critical field B_{c_1}, which is around 1000 G for bulk niobium [Hea08]. In order to study hysteretic effects B_{ext} was increased until we entered the irreversible regime (see Fig. 5.5b). At an external magnetic field B_{ext} of around 3.4 G irreversible hysteretic effects start to play a role. The enhanced field in the gaps B_{gap} is then on the order of B_{c_1} and finally flux starts to enter the superconducting material. This leads to additional vortices and thereby to increasing spots of normal conductivity. As a consequence the quality factor decreases strongly, which is qualitatively shown in the red inset in Fig. 5.5b.
To conclude, a field B_{ext} of only 3.4 G leads already to an enhanced field in the gaps on the order of B_{c_1} of the thin (200 nm) niobium layer.
Despite the fact that in principle one could use external fields for tuning superconducting half wave resonators it was of no importance for our purposes.

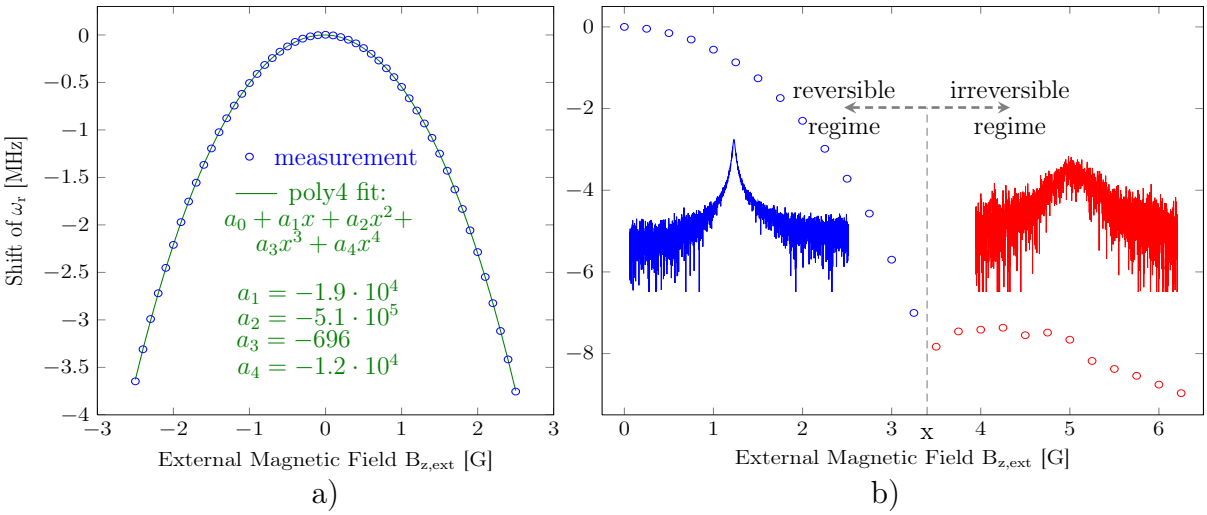

Figure 5.5.: The figures show the response of a half wave resonator to a perpendicular magnetic field. (a) Shift of ω_r towards lower frequencies for increasing $|B_{ext}|$. The fit model consisted of a polynomial of the 4th order. (b) In order to study hysteretic effects B_{ext} was increased until we entered the irreversible regime. From the value of the magnetic field at x one can estimate the flux focusing factor in the gaps between ground planes and conductor.

LER in a perpendicular magnetic field We also measured the effect of an applied perpendicular field on a LER resonator. Due to the much smaller spatial dimension of a LER compared to the half wave resonator, we expected a much weaker effect. Although we measured a slight frequency shift, the frequency resolution in the measurement was badly chosen and a repetition of the experiment not immediately possible. Thermal cycling of the resonator is necessary in order to remove the vortices from the resonator film. Although this measurement would be worth trying, we already saw, that the effect is negligible for our purposes.

5.1.2.2. Coupling ensemble of NV^- centres to a half wave resonator

The following section concerns the strong coupling of an ensemble of NV^- centres to the electromagnetic field of a half wave resonator. This kind of experiment was already presented in [Ams11]. The same experiment but carried out in a slightly different way was reported in [Kub10].

The NV^- centres containing diamond crystal was put on top of the resonator (for a schematic scheme see Fig. 4.6, for a picture see Fig. B.1). Since the coupling is magnetically the diamond is placed in the middle of the resonator length where the magnetic field of the resonator is maximum. The resonance frequency of the resonator ω_r was $2\pi \times 2.753\,\mathrm{GHz}$ and the quality factor Q_L with the diamond on top was around 2300. From this follows a resonator loss rate κ of $2\pi \times 0.598\,\mathrm{MHz}$ according to Eq. 2.8.
Note that the quality factor Q_L of the pure resonator was on the order of 40 000. The additional internal losses due to the diamond changed the resonator from an under-coupled to an over-coupled one. Since the resonators we work with are not tunable we have to apply magnetic fields on the diamond in order to tune the NV^- centres via the Zeeman effect towards the resonance frequency of the resonator (unlike in [Kub10] where they used a tunable resonator to get into resonance with the NV^- centres).
Due to the zero-field splitting the excited states ($|m_s = \pm 1\rangle$) of the NV^- centre are separated from the ground state ($|m_s = 0\rangle$) by around 2.87 GHz (see Fig. 3.1b). That implies that the resonator frequency at zero magnetic field was around 117 MHz smaller than the transition frequencies $|m_s = 0\rangle \rightarrow |m_s = \pm\rangle$. This frequency gap must be overcome in order to bring them into resonance. An applied external magnetic field shifts the energy levels of all three states according to the Zeeman effect (Eq. 3.2). How these shifts influences the ESR frequencies between the ground and the excited states of the two sub ensembles is shown in Fig. 3.2. The figures indicate that the direction of the magnetic field with respect to the crystallographic orientations of the sub ensembles determines the behaviour of the ESR. The angle α between the direction of the magnetic field and the crystallographic [100] axes was chosen to be 22.5° for the measurement.
Fig. 5.6a shows the result of the measurement in which we scanned the external magnetic field over a range, where a sub ensemble of NV^- centre became resonant with the resonator on the one hand and probed at each magnetic field the transmission spectrum of the resonator on the other hand. According to Fig. 3.2b and the fact that the resonator was designed to have a frequency less than the ESR of the NV^- centre at zero magnetic field one can conclude that the resonator is coupled to the $|m_s = -1\rangle$ state of the sub ensemble I. They become resonant at a magnetic field of around 63.5 G which implies

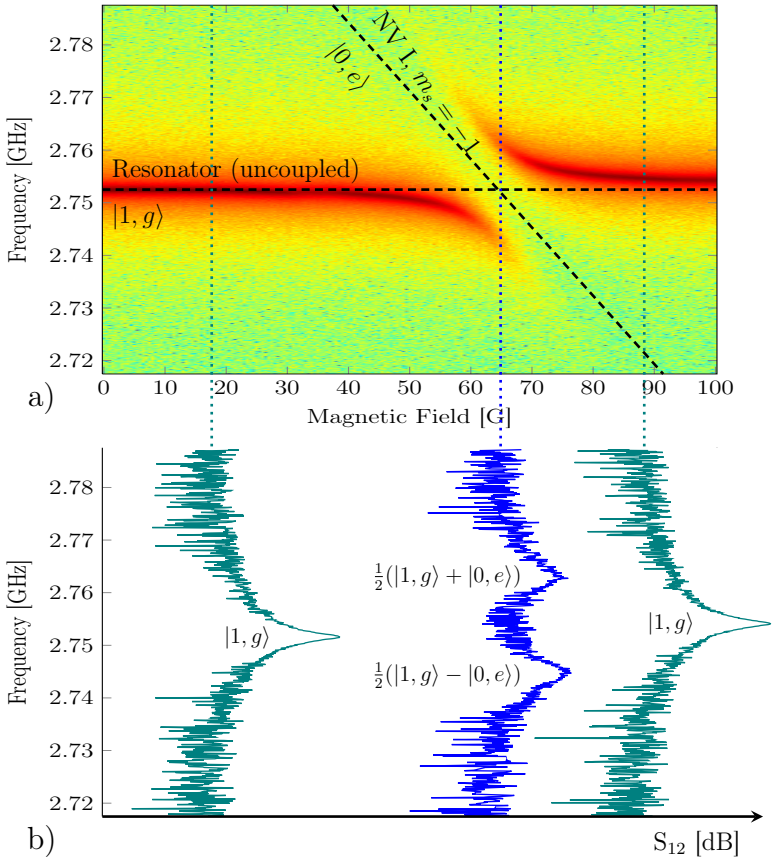

Figure 5.6.: (a) The colors represent the heights of a half wave resonator transmission amplitude. With increasing magnetic field in $\alpha = 22.5°$ direction (see Fig. 3.3b), the NV^- are tuned towards the resonator frequency - get coupled - and decouple again when the magnetic field as tuned them off-resonant enough. (b) One can see single traces taken from (a) for the 3 stages: towards coupling - coupling - after coupling. The resonances are labelled with their eigenstates.

that tuning is quite efficient and on the order of 2 MHz per Gauss. Fig. 5.6a shows experimentally what was schematically drawn in Fig. 4.4, the phenomena of the so called *avoided crossing*.

In Fig. 5.6b the transmission spectrum for certain values of the tuning magnetic field are shown: the left and the right traces (green) indicate the resonator transmission before and after the strong coupling regime was reached while the middle trace (blue) shows the point in which the ESR frequency has reached the resonator frequency ($\omega_\mathrm{r} = \omega_\mathrm{s}$). The transmission of the resonator shows a characteristics of a strong coupled system, namely two resonance, one when the probing frequency is near the symmetric (ω_+) and another one when near the antisymmetric (ω_-) eigenfrequency. This behaviour corresponds to the plot in Fig. 4.5. This implies that on the one hand the distance of the two peaks is directly proportional to the collective coupling strength $\mathrm{g_{col}}$ and on the other hand that the widths of the resonances or rather the total loss rate correlates with the arithmetic mean of the two involved loss rates, κ and γ.

A fit of each resonance in the trace at the degeneracy point (blue trace in Fig. 5.6b) with a Lorentzian line shape allowed a rough estimation of the essential parameters. The collective coupling strength $\mathrm{g_{col}}$ resulted to be around $2\pi \times 9.2\,\mathrm{MHz}$ while the FWHM of the peaks were on the order of $2\pi \times 3.8\,\mathrm{MHz}$. Finally, the loss rate of the spin ensemble γ turned out to be approximately $2\pi \times 6.5\,\mathrm{MHz}$.

Making use of Eq. 4.37 and Eq. 4.39 the calculation of the critical photon number and the cooperativity results in $n_0 = 0.061$ and $C = 19$. This implies that the formal criteria of strong coupling was well met.

5.1.2.3. Coupling ensemble of NV^- centres to a LER

Superconducting LERs have been proposed to be used as ultra sensitive photon detectors the so-called *lumped kinetic inductance detectors* (LKIDs) in the field of astronomy [Doy08],[Gao08]. The detection of a photon is based on a change in the kinetic inductance that as a consequence shifts the resonance frequency, as already briefly outlined in Sec. 5.1.2.1. However, the change in the kinetic inductance is not caused by an external magnetic but by incoming photons that break Cooper pairs. An important aspect is

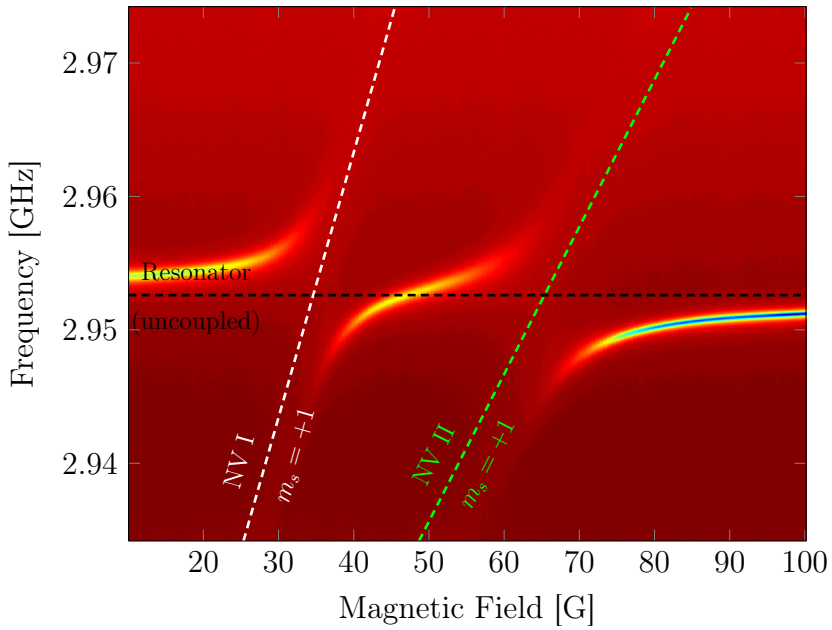

Figure 5.7.: The figure shows two avoided crossings between different subensembles of NV^- centres and a LER resonator. The resonator frequency ω_r at 0 Gauss is above the ZFS, therefore the NV^- ensembles tune from below towards the crossings (see Fig. 3.3b).

their small dimensions compared to half wave resonators, that makes LER a promising candidate to improve the spatial resolution of these kind of detectors.

In the field of circuit QED the use of LERs have not yet been tested to any great extent. Especially in the context of hybrid quantum system that is accompanied by the problem of inhomogeneous broadening of ensembles of microscopic quantum entities it is worth investigating how far LERs can contribute to the solution. A possible contribution might come from the fact that the mode volume of a LER can be made much smaller compared to half wave resonators. A reduced mode volume should not effect the collective coupling strength, however, might lead to less inhomogeneous broadening simply due to the fact that less NV^- centres are involved in the coupling process.

The experiment that is presented in this section shows an ensemble of NV^- centres that is strongly coupled to a LER (see Fig. 5.7). To our knowledge, it is the first time that this has been realised. The performance was basically the same as the one described in the previous section.

We used a LER that was capacitively coupled to a feed line and with a resonance fre-

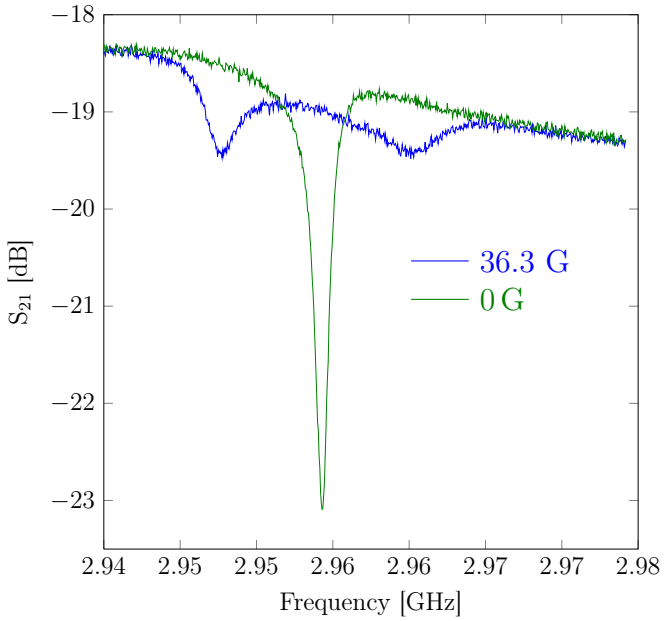

Figure 5.8.: The figure shows on the one hand the skewed background of the transmission level and on the other hand the transmission spectrum of the resonator far detuned (0 G) and in resonance (36.3 G) with the spin-ensemble, respectively.

quency ω_r of $2\pi \times 2.964$ GHz. Q_L without diamond on top was 5664 and with diamond around 4641, respectively. Therefore the LER was over-coupled even without diamond on top.

According to [Kol12] the mode volume V_{mod} was by a factor of 10 smaller compared to the half wave resonator.

The measurement that is shown in Fig. 5.7 indicates strong coupling with two different subensembles. As ω_r is larger than ω_s at zero magnetic field the LER couples to the $m_s = +1$ subensembles that tune from below towards ω_r. The angle of the magnetic field with respect to the crystallographic [100] direction of the diamond was again 22.5°. The values of the magnetic fields of the two degeneracy points (36.3 G and 67 G) are in good agreement with theoretical predictions. In Fig. 5.8 one can see the resonator transmission for the case that ω_s is far detuned from ω_r and once for when they are in resonance (blue, 36.3 G). The traces show that the background or rather the level of the transmission decays for around -1 dB within the plotted frequency range (note that this problem does not occur when using half wave resonators since they behave the opposite thus trans-

mission at resonance). The decay shows the roughness iof the amplifiers bandwidth that leads to deformations of the transmitted signal.
However, the splitting of the transmission spectrum into two resonance that correspond to the eigenfrequencies of the coupled system can clearly be seen. The coupling strength g_{col} roughly estimated was on the order of $2\pi \times 12\,\mathrm{MHz}$. (note that g_{col} can not be compared with the coupling strength of the previous section since two different diamonds were used). This single measurement does not allow a conclusion whether the size of the mode volume V_{mod} indeed is a parameter that can be used to gain control on the inhomogeneous broadening of the spin-ensemble. However, it is a first important step that shows that the strong coupling regime can be reached with LERs too.

5.1.2.4. Probing power dependency of the coupling process

In the previous sections it was shown how a resonator has been coupled to a spin-system by tuning them into resonance. In this section it will be shown that the coupling can also bee controlled by the power of the probe tone. In Fig. 5.9 one can see a scan of the probing power at the degeneracy point ($\omega_r = \omega_s$). The figure indicates the dependence of the coupling strength or rather the Rabi splitting on the probing power. It shows that below a certain measurement power threshold (in this case of around - 20 dBm but note, that the absolute values of the probe power in the figure do not matter since the probe tone gets strongly attenuated on the way to the resonator) the splitting becomes independent from the probing power. This behaviour characterises the low excitation regime where the coupling is maximum.
A rather different effect can be seen if the probing power is increased above the threshold. The two peaks shifts and merge into a single peak that approaches the empty resonator resonance, characterising the high excitation regime.
In the low excitation regime the NV^- centres can be approximated by harmonic oscillators, as already mentioned in Sec. 4.2.2 within the context of the range of validity of the Holstein-Primakoff approximation. In [Gri97] they show that in the high excitation regime the cooperant fashion of spins get more and more lost with increasing power. As a consequence the NV^- centres behave more and more as single entities which gives rise

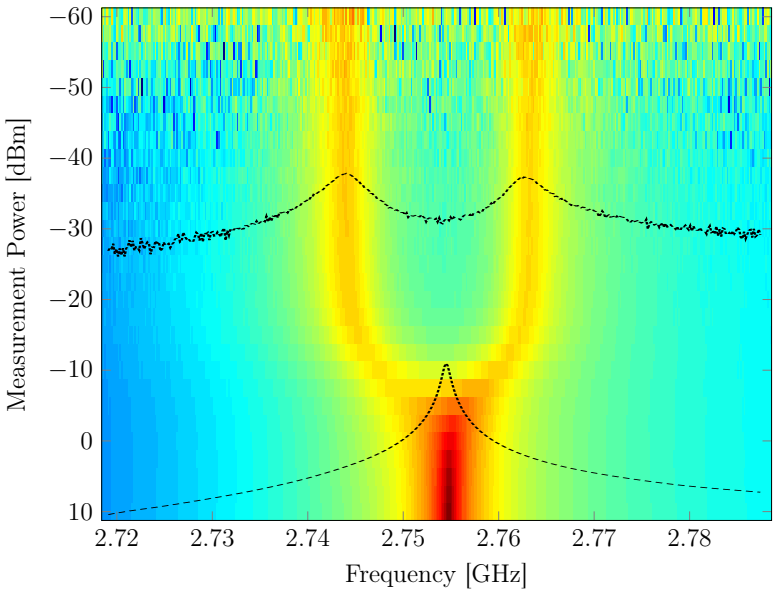

Figure 5.9.: The Figure shows a probing power scan from the low (double peak) to the high excitation (single peak) regime. In the low excitation regime coupling is maximum unlike in the high excitation regime that finally ends in a decoupled system.

to non-linear effects resulting from anharmonic oscillators.

Finally all the spins are saturated and do no longer play a role in the spin-resonator system. In principle, Fig. 5.9 shows the results of a routine measurement that allows us to determine the power threshold of the probe tone for a maximum coupling strength.

The measurement was carried out with 10 averages that lead to the fact at probe tone power at the VNA output of around -60 dBm the signal of the two peaks begin to disappear more and more below the noise floor.

Between the VNA output and the resonator input the signal gets attenuated by around -69 dB. With the following equation the number of photons in the cavity can be estimated [Fin10]:

$$P_{\mathrm{in}} \approx n\hbar\omega_{\mathrm{r}} 2\kappa. \tag{5.4}$$

For an output power of -60 dBm, a resonator decay rate $\kappa \approx 2\pi \times 0.4\,\mathrm{MHz}$ and a resonance frequency $\omega_{\mathrm{r}} \approx 2\pi \times 2.755\,\mathrm{GHz}$ the number of photons in the resonator n is around 15, already quite close to the single photon level.

5.2. Time domain measurements

Measurements in the time domain in principle offer access to a lot of interesting physics, e.g. pulsed measurements.

The experiments so far were carried out in the frequency domain. That basically means the measure of the response of a system with respect to a certain frequency by applying a drive tone. If the time that the system is driven by the probe tone is long enough, it will end in a mixed state. It is then the steady state of a system that is generally measured by doing spectroscopy.

But if one is interested in very fast proceeding time depend processes it is necessary to make time dependent measurements. This basically means measuring the signal (e.g. transmission) with a certain rate, the so called sample rate. The sample rat of the data acquisition is an important parameter since it defines the temporal resolution. Apart from this, averaging is a very crucial aspect. In spectroscopy a signal can be averaged quite easily since the state that is measured is a steady one, such that one can collect data over a certain time and then calculate the mean of the acquired data points. Averaging in time domain means repeating the time dependent measurement as often as necessary, summing them up and getting the mean out of it.

In the following sections the set-up for time domain measurements will be introduced followed by the presentation of two experimental results. In a first step the cavity decay (ringdown) will be shown and in a second step the spectroscopically measured coupling experiment from Sec. 5.1.2.2 will be studied in the time domain.

5.2.1. Experimental setup

A schematic drawing of the set-up that was used for the time domain measurements is shown in Fig. 5.10. A comparison with Fig. 5.2 indicates that in our case the measurement in time domain were more difficult to perform than spectroscopy with a VNA. To allow further signal processing is has to be shifted to a lower frequency range. How this can be achieved will be shortly outlined in the next paragraph followed by a description of the individual components used in the set-up.

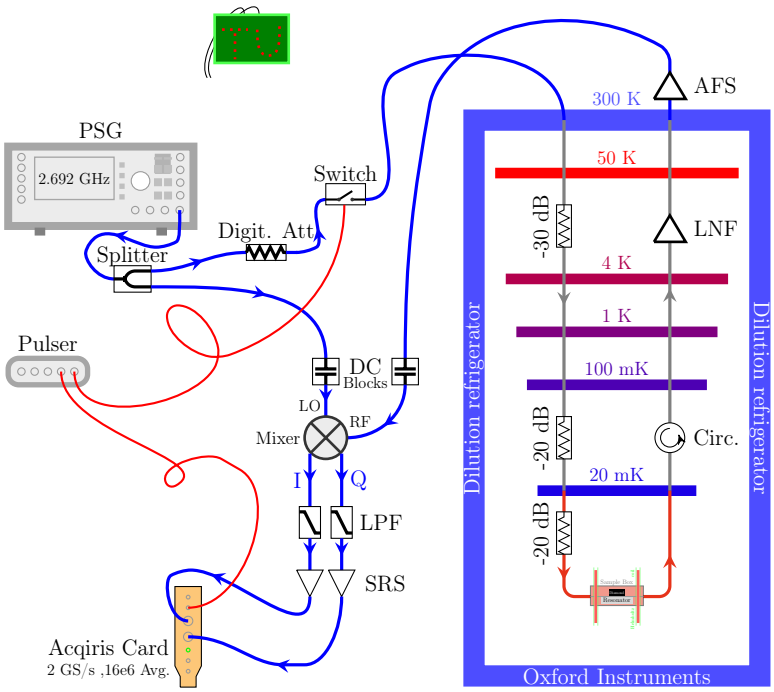

Figure 5.10.: Measurement setup to realize time domain measurements of the coupled resonator NV ensemble system. The FPGA pulse generator controls the sequence of the measurement. Wit the IQ mixer a homodyne measurement is realized and the Acqiris digitizer card records the fast quadrature signals.

Analog down conversion According to the Nyquist sampling theorem one needs basically at least a sample rate of $2f_0$ to be able to reconstruct a signal of frequency f_0 completely. If the maximum sample rate of a device is e.g 0.5 ns, the maximum frequency of a signal that can be measured is 1 GHz. If the frequency of the signal is higher than 1 GHz it can be *down converted* in order to digitally record signals that exceed the sample rates of the fastest available digitizer cards. How this down conversion can be achieved will be roughly outlined in what follows.

From the trigonometric identities it is known that

$$\cos(\alpha) \cdot \cos(\beta) = \frac{\cos(\alpha - \beta) + \cos(\alpha + \beta)}{2}. \tag{5.5}$$

Hence, multiplication (mixing) of two sinusoidal signals with frequencies ω_α and ω_β leads to two output signals, a very high frequency ($\omega_\alpha + \omega_\beta$) and the other with a lower frequency ($|\omega_\alpha - \omega_\beta|$). This is in principle what a multiplying electronic mixer does. In order to achieve a complex amplitude we use an IQ-mixer, sketched in Fig. 5.11a.

The IQ-mixer is a four port device with two input and two output ports. The RF (radio frequency) input port is for the information carrier signal ($v_{\mathrm{RF}}(t) = A_{\mathrm{RF}}(t)\cos(\omega_{\mathrm{RF}}t + \alpha(t))$), thus the one that comes from the experiment. The other input, labelled with LO (local oscillator) does not contain any information ($v_{\mathrm{LO}}(t) = A_{\mathrm{LO}}\cos(\omega_{\mathrm{LO}}t)$), thus remains stable in phase and amplitude and is needed for the act of down conversion.

Mixing of these two signals according to Eq. 5.5 leads to the following result:

$$v_{\mathrm{out}}(t) = v_{\mathrm{LO}}(t) \times v_{\mathrm{RF}}(t) = \frac{A_{\mathrm{LO}}A_{\mathrm{RF}}(t)}{2}\left\{\cos((\omega_{\mathrm{LO}} + \omega_{\mathrm{RF}})t + \alpha(t)) + \cos((\omega_{\mathrm{LO}} - \omega_{\mathrm{RF}})t + \alpha(t)\right\}. \tag{5.6}$$

One can see that the modulation is indeed translated to two new frequencies, the sum (LO + RF) and the difference (LO − RF). Usually either the upper or lower *sideband* is selected by filtering the output of the mixer.

As one can see in Fig. 5.11a the IQ mixer consists basically of two mixers ($\bigotimes$). Both, the RF and the LO input are split whereupon the LO branch that goes to the Q-quadrature mixer is shifted by $\pi/2$ which means that the Q-quadrature is shifted by $\pi/2$ from the I-quadrature. Because of $\sin(\delta + \pi/2) = cos(\delta)$ the I-quadrature and the Q-quadrature

interpreted as the real and imaginary part of a complex amplitude A (Fig. 5.11b). Finally the phase and amplitude information that the RF signal carries are transmitted to the I and Q output of the mixer. If the RF and the LO share the same microwave

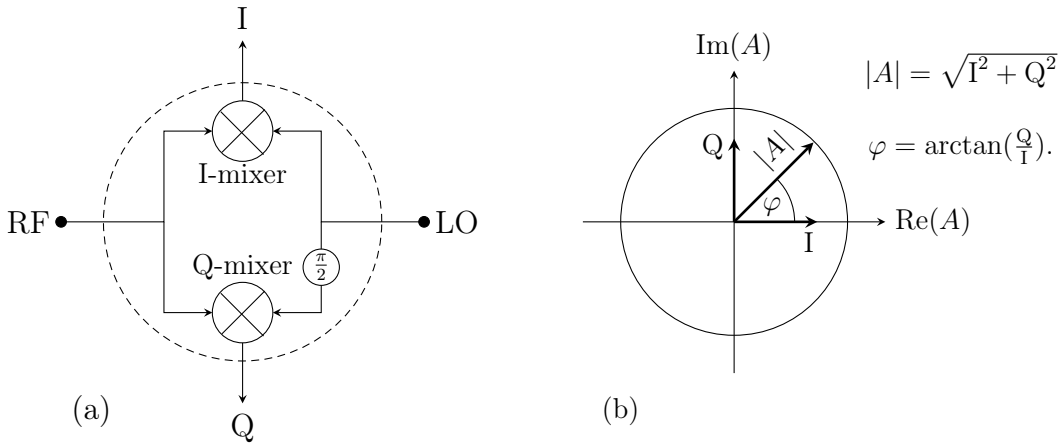

Figure 5.11.: (a) Shows the four ports of an IQ-mixer and the data processing inside. (b) Shows how the magnitude $|A|$ and the phase φ can be reconstructed from I and Q.

source or rather $\omega_{\mathrm{RF}} = \omega_{\mathrm{LO}}$ which finally leads to the fact that the intermediate frequency of I and Q is zero. This kind of down conversion to DC is called *autodyne*.

Measuring procedure Fig. 5.10 shows a set-up that performs an autodyne downconversion of the signal since there is only a single microwave source, a **PSG**[3] signal generator. In order to get two microwave lines, one for the LO line and another for the RF line the beam is divided by a **splitter**[4]. The power of the signal in the RF line can be varied by a **digital attenuator**[5]. This is necessary since the power of the signal that arrives in the sample box shall not be to high (see Sec. 5.1.2.4). Attenuating only the RF line keeps the power in the LO line high which finally determines the magnitude of the signal after the downconversion, according to Eq. 5.6. After the signal has been attenuated it a arrives at a **switch**[6]. The timing of the switch, thus the length of the pulse, is controlled by a **pulser**[7] (note that the LO line is not switched since the down conversion process has to

[3] 1E8257C PSG, option 1EA and 520 (250 kHz-20 GHz), Agilent
[4] 2ZAPD-4+, Mini Circuits (2-4.2 GHz)
[5] ZX76-15R5-SP+ Mini-Circuits
[6] 4ZASWA-2-50DR+, Mini-Circuits
[7] home-built FPGA based pulser card

be maintained even if the RF signal is off). The RF signal after it has passed the switch enters into a **Dilution refrigerator** (DR). The set-up inside the DR including the amplification by an **AFS** after leaving was the same as for the spectroscopic measurements (for details see Sec. 5.1.1). Before the LO line and the RF line are down converted they have to pass **DC blocks**[8] in order to filter noise in the range of 50 Hz caused by possible ground loops. The down conversion finally was done by an IQ-**mixer**[9]. To select the low sideband of the mixer outputs the I and Q channels were filtered by a **LPF**[10] and preamplified by a **SRS**[11] before the I and Q signals in the range of milliVolts or below were saved and processed in a **Acqiris card**[12] that comes with a dual channel ADC use with 2GS/s, on-board FPGA for real-time data processing, a maximum of $16 \cdot 10^6$ averages and a vertical resolution of 8 bit.

5.2.2. Results of time domain measurements

The measurements in the time domain were carried out with a spectroscopic well known combination of half wave resonator and diamond. We started with measurements of the resonator decay, thus the resonator with the diamond on top but the spins far detuned (170 MHz). Since we knew what results we had to expect we were able to test the set-up and to gain confidence in the new technique. In a next step we tuned the spins into resonance with the cavity and observed the changing time behaviour.

5.2.2.1. Cavity decay

Close to the resonance frequency ω_r the resonator transmission as a function of the probe frequency ω_p is a Lorentzian curve. The transfer function that relates the input with the output signal written in terms of the resonator loss rate κ is

$$S(\omega_\mathrm{p}) = \frac{-i\kappa}{-i\kappa + \omega_\mathrm{p} - \omega_\mathrm{r}}. \tag{5.7}$$

[8] SD3258 DC BLOCK (0.01 GHz-18 GHz) Fairview Microwave Inc.
[9] IQ-0255LMP (LO/RF 2.0 to 5.5 GHz IF DC to 500 MHz), Marki microwave
[10] VLFX -300 (0-300 MHz), Mini-Circuits
[11] SR445A 350 MHz preamplifier Standard Research Systems
[12] 5U1084A, Acqiris card, Agilent

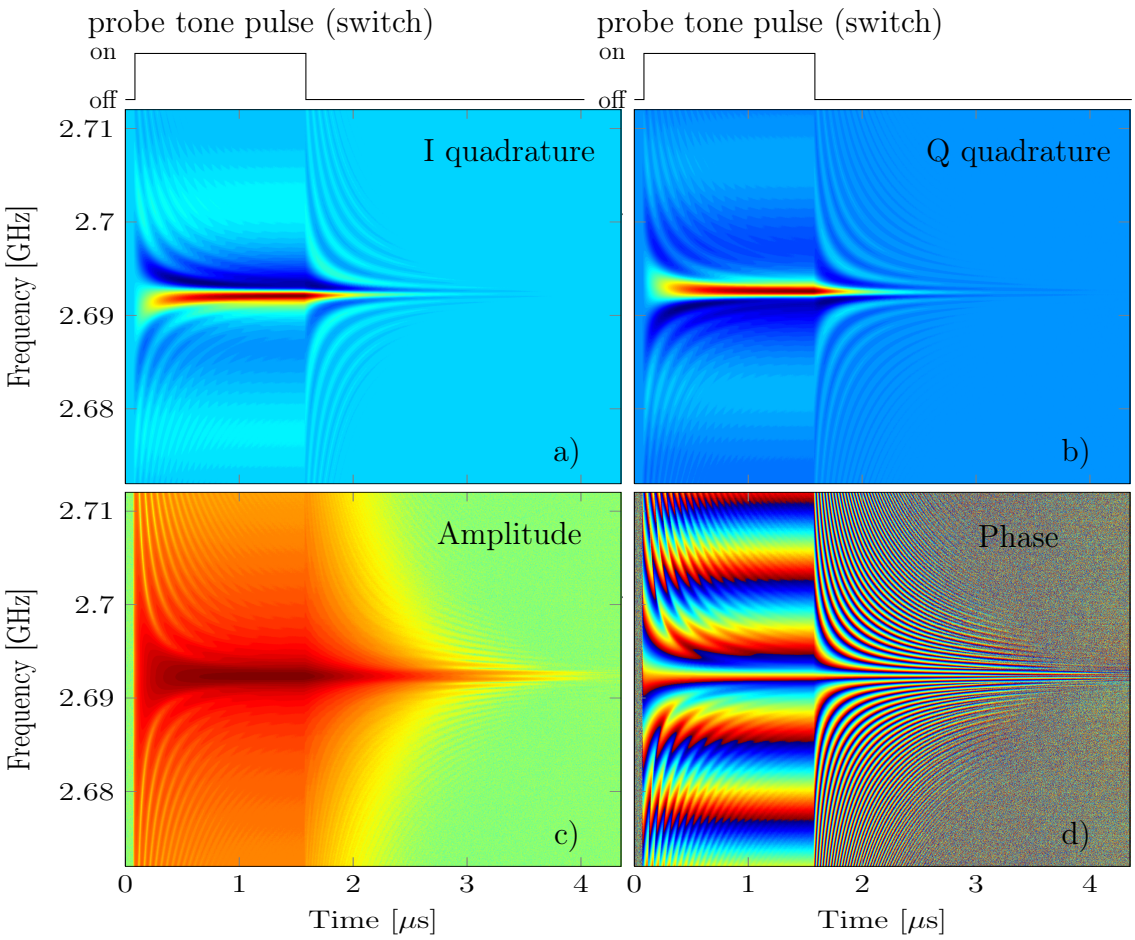

Figure 5.12.: The figures show the results of measurement where a pulse of 1.5 µs was applied on an over-coupled resonator with a Q-factor of ≈ 3500 and a resonance frequency ω_r of around 2.693 GHz.

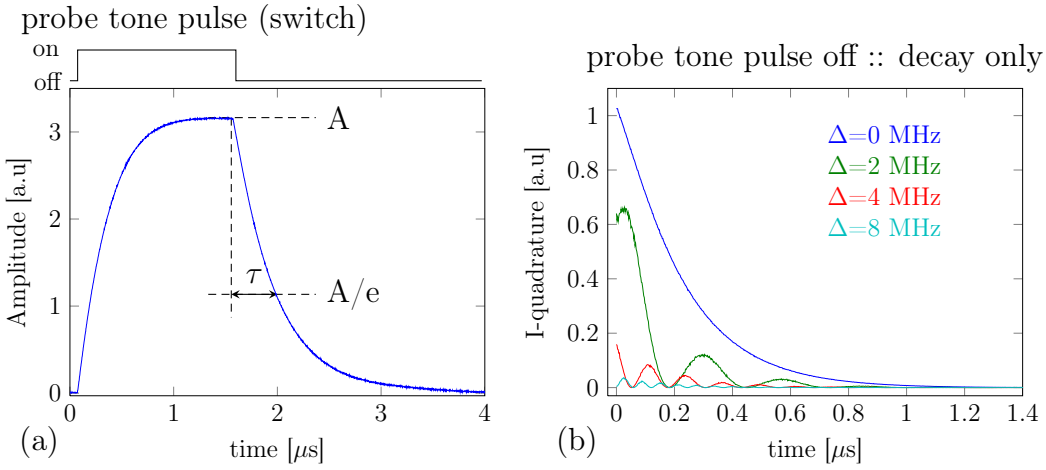

Figure 5.13.: (a) The decay of a Lorentzian is exponential. (b) The decay of I and Q is dominated by the term $\exp[\mathrm{i}\Delta t]$, with the detuning $\Delta = |\omega_\mathrm{r} - \omega_\mathrm{p}|$.

In the time domain the output signal in principle is a convolution of the input signal ($\propto A_{RF}\mathrm{e}^{i\omega_p t}$) with the Fourier transformed transfer function $\mathcal{F}_{\omega_\mathrm{p}}[S(\omega_\mathrm{p})](t) \propto \mathrm{e}^{i\omega_\mathrm{r} t}e^{-\kappa t}$.
At the IQ-mixer the signal in autodyne down conversion mode is multiplied with LO line $\propto A_{LO}\mathrm{e}^{i\omega_\mathrm{p} t}$ so that the complex signal after the down conversion

$$A_\mathrm{IQ}(t) \propto A_\mathrm{st}\mathrm{e}^{i(\omega_\mathrm{r}-\omega_\mathrm{p})t}e^{-\kappa t} \tag{5.8}$$

with $A_\mathrm{st} = A_\mathrm{LO}A_\mathrm{RF}$.
Thus the signal on channel $\mathrm{I}(t) = \mathrm{Re}[A_\mathrm{IQ}(t)] \propto A_\mathrm{st}\cos(\omega_\mathrm{r}-\omega_\mathrm{p})\mathrm{e}^{-\kappa t}$ and $\mathrm{Q}(t) = \mathrm{Im}[A_\mathrm{IQ}(t)] \propto A_\mathrm{st}\sin(\omega_\mathrm{r}-\omega_\mathrm{p})\mathrm{e}^{-\kappa t}$ and the magnitude of the amplitude $|A_\mathrm{IQ}|(t) \propto A_\mathrm{st}\mathrm{e}^{-\kappa t}$.
The decay of the amplitude $|A_\mathrm{IQ}|$ is exponential also for $\omega_\mathrm{p} \neq \omega_\mathrm{r}$. Fitting the decay shown in Fig. 5.13a with $\mathrm{e}^{-t\kappa}$ we get the value $\kappa = 2.46$ MHz respectively $\kappa/(2\pi) = 392$ kHz which is in good agreement with the values that we obtain from fitting spectroscopic measurements. As already mentioned in Sec. 2.1, we have defined κ such that it is directly related to the mean live time τ of the resonator: $\kappa = 1/\tau$, thus $\tau = 405$ ns.
In contrast to the amplitude the deccay of I and Q depend very much on the detuning $\Delta = |\omega_\mathrm{r} - \omega_\mathrm{p}|$. The oscillation actually should scale with $\cos(2\pi\Delta)$. This behaviour can be seen in Fig. 5.13b, where several traces of the decay of the I-quadrature are plotted for different Δ's.

5.2.2.2. Decay of a coupled system

The idea of the measurement that is presented in this section was to measure the dynamics of a resonator coupled to a spin-system. That means to study how such a strong coupled system, that spectroscopically shows two peaks, builts-up and decays. In [Kub12] they report the storage and retrieval of microwave photons from a resonator into an ensemble of NV^- centres. They show that the dynamics are limited by inhomogeneous broadening of the spin ensemble. In this sense, we expected that the results from time dependent measurements might allow us to characterise the inhomogeneous broadening of our diamond sample easier than it was performed in [San12] based on spectroscopic measurements.

To investigate this we used the same half wave resonator and diamond as we have employed for the measurement in Sec. 5.1.2.2, tuned them into resonance and scanned with the probe frequency over the range of interest. Fig. 5.14 shows overview plots of such a scan. In the amplitude plot in Fig. 5.14(c) one can see from the colors that the magnitude of the signal is maximum at the symmetric and the antisymmetric eigenmodes (labelled in white). This characteristics corresponds to the two peaks that were shown in the Secs. 5.1.2.3 and 5.1.2.2. Additionally one can see that the oscillations that occur after the pulse has been switched off are strongest in the middle of the frequency range, thus when $\omega_\mathrm{p} = \omega_\mathrm{s} = \omega_\mathrm{r}$ (labelled in black).

However, this can be seen better in Fig. 5.15 that shows the traces of two specific probe frequencies. The fact that the green trace (labelled with $\omega_\mathrm{p} = \omega_+$) indicates the response of a coupled system that is probed at one of its eigenfrequencies explains on the one hand the higher amplitude (since it shows the top of a peak) and on the other hand the approximately exponential decay (for decay of a Lorentzian see Sec. 5.2.2.1). On the contrary, the blue trace in Fig. 5.15 indicates the response for a system that is driven off resonance. The decay shows the coherent exchange of excitation or rather energy.

The resonator decays very fast (around 15 ns). In the previous section it was shown that the rate with which the photons leak out of the resonator is on a different time scale, namely on the order of 400 ns. This gives rise to the assumption that the photons mainly moved into a collective spin excitation in the diamond. In turn, when the spin excitation

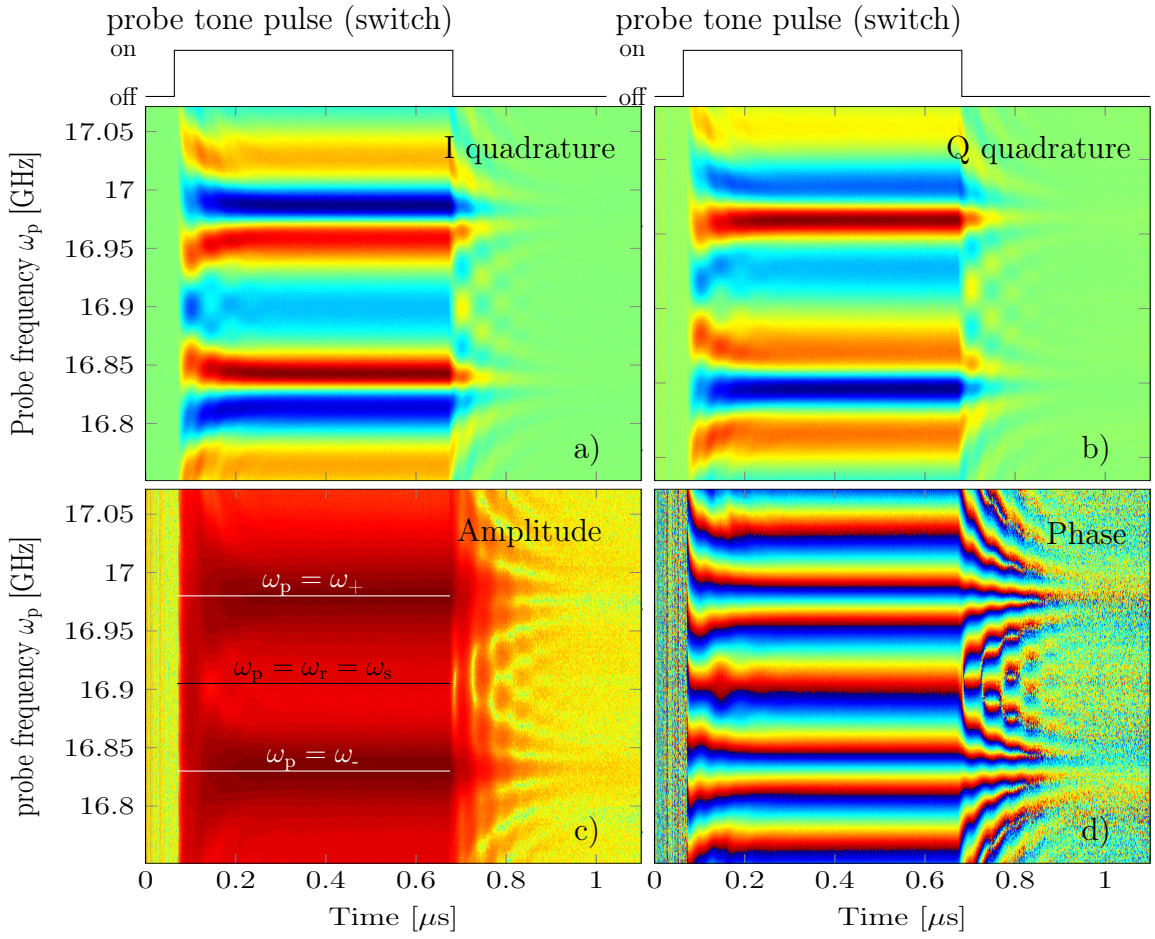

Figure 5.14.: The figures show the results of a pulsed measurement of a resonator that was coupled strongly to an ensemble of NV^- centres.

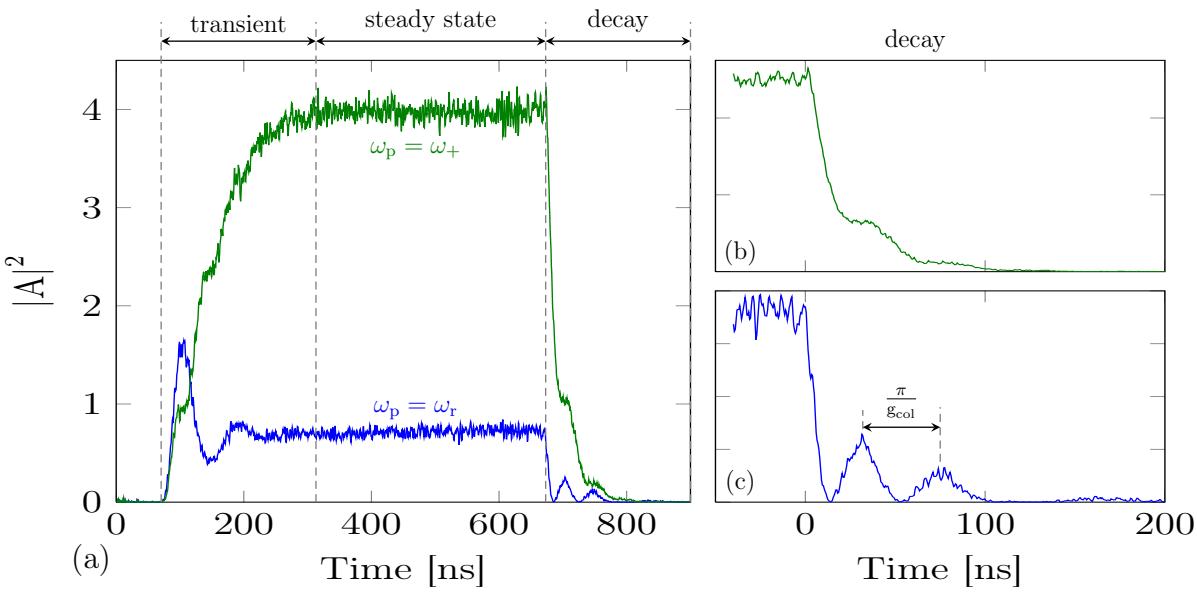

Figure 5.15.: The figure shows the traces from the scan in Fig. 5.14(c) for two specific conditions of the probe frequency.

decays the resonator again gets populated by some of the photons. This kind of cycling happens only a few times since the losses, above all caused by dephasing processes in the spin-ensemble, are quite big.

The period T with which the excitations are coherently exchanged is on the order of 40 ns. This is in good agreement with the value of the coupling strength g_{col} on the order of $2\pi \times 11\,\mathrm{MHz}$ that was estimated from spectroscopic measurements. A more specific analysis of the time domain measurements are given in Chap. 6.

The angle α of the magnetic field with respect to the crystallographic [100] direction of the NV^- centre was 0°. From the Figs. 3.2 and 3.3(a) one can see that for this case both subensembles tune equally. This implies that probably twice as many NV^- centres were involved in the coupling process compared to the spectroscopic measurement from the previous sections ($\alpha = 22.5°$). Furthermore the measurement was carried out with $2 \cdot 10^6$ averages.

Single photon level According to the critical photon number n_0 we formally operate already on the single photon level although the effective number of photons is on the order of 10^4. That means that no new physics is to be expected if the single photon level is reached experimentally too. But if the excitation of the resonator consists of a single photon that finally is exchanged coherently between the resonator and the NV^- ensemble the quantum mechanical regime indeed reached. However, to approach experimentally the single photon level is a big challenge. The mean occupation number of thermal photons $\langle n_{th} \rangle = (e^{\frac{h\nu}{k_B T}} - 1)^{-1}$ for resonators that are designed to get resonant at frequencies of several GHz is around 10^{-4} at an operating temperature of 20 mK. Therefore the main obstacle for the tiny signal of a single photon to be measured are probably the noise pick up between the resonator output and the first amplification on the one hand and the noise floor of the amplifier itself on the other hand.

By means of sufficient averaging in principal it should be possible to recover a signal or rather to achieve an adequate signal to noise ratio (SNR).

Since we had a very capable data acquisition card that provided a performance of 16 million averages we tested to see how close we can get to the single photon level.

Surprisingly, the single photon level with 16 million averages remained clearly out of

reach. For the lowest probing power that still resulted in a recognisable output signal the corresponding mean photon number $\langle n \rangle$ in the resonator from a rough estimation on the basis of Eq. 5.4 turned out to be around $5 \cdot 10^3$.

6. Modelling and analysis of the time domain measurements

In this chapter different approaches will be introduced that were used in order to gain an understanding of the measurements of the previous chapter.
A first step will be an exponential fit to the envelopes to determine the damping of the traces. Since inhomogeneous broadening is the limiting factor for the dynamic of the coupled system a proper parametrisation of the spin distribution is important. There are two parameters that are important for the characterisation of the spin-distribution, one that accounts for the width γ_{inh} and one that accounts for the shape. This, amongst others, will be done in further steps were theoretical models will be introduced that allow to reconstruct the traces.

Inhomogeneous broadening: width and shape The spectral linewidth of a single, isolated NV^- centre is its natural linewidth which is expected to have a Lorentzian profile. In our case we have a resonator that is coupled to an ensemble of NV^- centre which implicates homogeneous and inhomogeneous broadening effects on the linewidth. Homogeneous broadening effects are equal for all single NV^- centres whereas inhomogeneous effects are different for each NV^- centre. That means that the homogeneous broadening is the lower limit of the inhomogeneous broadening. For example slightly varying ESR frequencies due to several reasons results in an inhomogeneously broadened spectral linewidth of the ensemble.
The interactions of the NV^- centres with their environment determines the shape of the spectral distribution. Dipolar interactions for example lead to Lorentzian spin distributions [Hon69] whereas hyperfine interaction results in a Gaussian spin distribution. It

is to be expected that both the dipolar and the hyperfine interaction play a role which would imply that the distribution is whether a Lorentzian nor a Gaussian but a mixture of both.

In principle, once the shape of the distribution has been determined conclusions with respect to the interactions might be possible. But apart from this, particularly the shape of the wings of the distribution can have a crucial impact on the dynamic properties. The support is not bounded for both distributions, the Lorentzian and the Gaussian, whereas the former falls of $\propto 1/\omega^2$ the latter decays faster, namely $\propto \exp[-\omega^2]$. In [Kur11] [Din11] they studied the influence of the shape of the distribution on the width of the two resonances at the two eigenmodes (polaritonic peaks) of a coupled system.

They have found out that increasing the collective coupling strength g_{col} may lead to a narrowing of the polaritonic peaks provided a spectral density that in the wings of the distribution decays faster than ω^{-2} (Lorentzian). This phenomenon was termed *cavity protection*.

That implies that for a Gaussian the effect of cavity protection should in principle be usable whereas for a Lorentzian, since it is the limiting case, the polaritonic peak width tends towards a constant. A consequence of cavity protection in the time domain would be significant more cycles of excitation exchange between resonator and spin ensemble due to reduced damping or rather reduced losses.

6.0.3. Exponential decay

In Sec. 5.2.2.1 it was shown that the decay of a Lorentzian is exponential. The idea of what follows is to find out to what extend this holds for the decay of the peaks of the Rabi splitting and the damping of the Rabi oscillations. The results are shown in Fig. 6.1(b)(c) and indicate that the damping indeed seem to be exponential. Furthermore one can see that the decay of the resonance peak at $\omega_p = \omega_+$ is clearly faster than the damping off resonance ($\omega_p = \omega_r$). In Fig. 6.1(b), that shows both traces scaled to the same initial value in one plot, one can see that indications of excitation exchange are clearly visible even for $\omega_p = \omega_+$. The decay of the resonance peak seems to be nearly interrupted within the yellow marked periods.

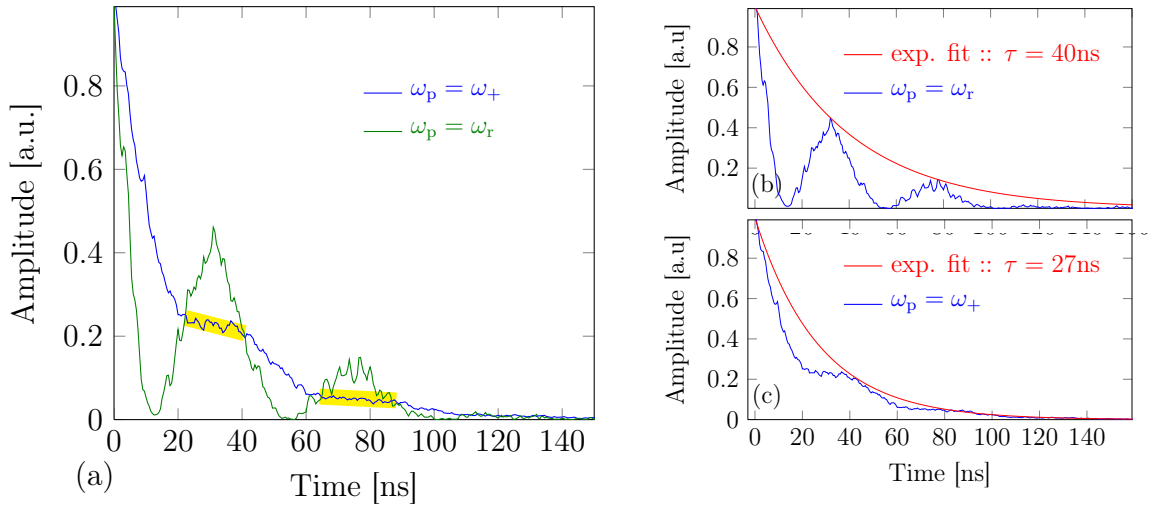

Figure 6.1.: (a) Shows the traces from Fig. 5.15(a) and (b) with a normalised initial value. The yellow markers indicate the periods in which the decay of the resonance peak at ω_+ is strongly slowed down due to excitation exchange. (b) Exponential fit of the damping.

6.0.4. Trace modelling

In what follows three models will be introduced that allowed a modelling of the traces assuming different approximations.

The first model assumes a Lorentzian distribution where the inhomogeneity was implement by replacing the homogeneous simply by inhomogeneous width.

The second model is an extension of the first model, that allows basically to distinguish between a discrete Lorentzian and a Gaussian distribution. The third model in principle determines all the essential parameters, including the parametrisation of the shape of the spin distribution.

6.0.4.1. Quasi inhomogeneous modelling

The set of linear differential Eqs. 4.40 and 4.41 can be combined in a matrix equation of the form

$$\frac{\mathrm{d}}{\mathrm{d}t}\begin{bmatrix}\langle a\rangle\\ \langle\sigma^-\rangle\end{bmatrix} = \begin{bmatrix}-(\kappa+\mathrm{i}(\omega_r-\omega_p)) & -\mathrm{i}g_{col}\\ -\mathrm{i}g_{col} & (-\frac{\gamma_{inh}}{2}+\mathrm{i}(\omega_s-\omega_p))\end{bmatrix}\begin{bmatrix}\langle a\rangle\\ \langle\sigma^-\rangle\end{bmatrix}. \tag{6.1}$$

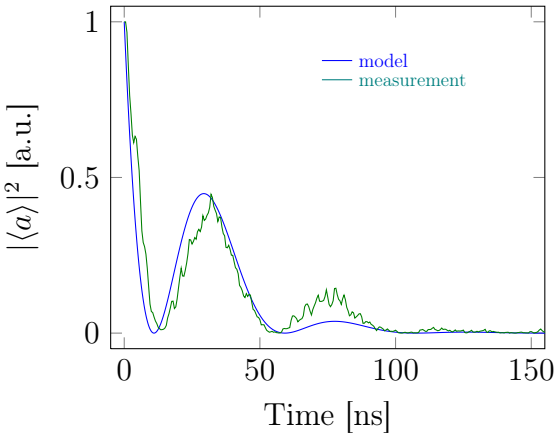

Parameters [MHz]

$\gamma_{\mathrm{inh}}/2\pi$	15.5
$\kappa/2\pi$	0.4
$\mathrm{g}_{\mathrm{col}}/2\pi$	11

Figure 6.2.: The Fig. shows the best approximation of the experiment based on the model described in Eq. 6.1. The parameters were manually optimised.

where the drive term η was dropped since we were interested in the decay of the system. Furthermore the width γ was replaced by the FWHM of the inhomogeneous broadening γ_{inh}. So to say it describes a homogeneous Lorentzian broadening with a width of the extend of the inhomogeneity. Along the diagonal of the non-hermitian coefficient matrix in Eq. 6.1 the losses and the resonance frequencies appear whereas the coupling is described by the off-diagonal terms.

The initial values or rather the steady state values $\langle a \rangle_{\mathrm{st}}$ and $\langle \sigma_- \rangle_{\mathrm{st}}$ that are needed to solve the matrix equation can be obtained by solving the equation under the conditions $\langle \dot{a} \rangle = 0$ and $\langle \dot{\sigma}_- \rangle = 0$.

Fig. 6.2 shows the best result in accordance with the measurement which was found by manual optimisation of the parameters. It was only possible to get the model in relative agreement with one of the two revival peaks. In other words, the damping of the model deviates quite strongly from an exponential decay. This is somehow remarkable since the model describes a system with two Lorentzian-like resonances that has been driven off-resonantly before the driving tone was switched off.

However, the simplicity of this model makes it useful for extracting rough estimates for the parameters $\mathrm{g}_{\mathrm{col}}$, κ and γ_{inh}. The results for κ and $\mathrm{g}_{\mathrm{col}}$ are in the range of expectations unlike γ_{inh} that tends to be larger than expected.

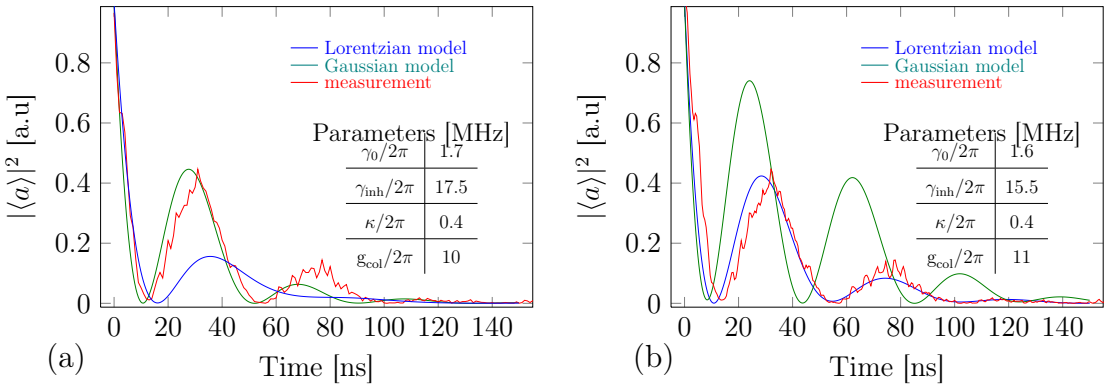

Figure 6.3.: The Figs. show the best approximations of the experiment based on the model described in Eq. 6.2 once with respect to (a) Gaussian and once to a (b) Lorentzian distribution. The parameter were manually optimised.

6.0.4.2. Discrete inhomogeneous modelling

The next step was to extend the model of the previous section towards the implementation of discrete inhomogeneous spin distributions. This was basically achieved by extending the matrix equation 6.1 and distributing the ω_{is} $(i = 1 \ldots N)$ along the diagonal axes according to a Lorentzian or a Gaussian distribution. This looks then like this:

$$\frac{\mathrm{d}}{\mathrm{d}t}\begin{bmatrix} \langle a\rangle \\ \langle {\sigma_1}^-\rangle \\ \vdots \\ \langle {\sigma_N}^-\rangle \end{bmatrix} = \begin{bmatrix} -\kappa + \mathrm{i}(\omega_\mathrm{r} - \omega_\mathrm{p})) & -\mathrm{i}\frac{g_\mathrm{col}}{\sqrt{N}} & \ldots & -\mathrm{i}\frac{g_\mathrm{col}}{\sqrt{N}} \\ -\mathrm{i}\frac{g_\mathrm{col}}{\sqrt{N}} & (-\frac{\gamma_0}{2} + \mathrm{i}(\omega_{s1} - \omega_\mathrm{p})) & 0 & 0 \\ \vdots & 0 & \ddots & 0 \\ -\mathrm{i}\frac{g_\mathrm{col}}{\sqrt{N}} & 0 & 0 & (-\frac{\gamma_0}{2} + \mathrm{i}(\omega_{sN} - \omega_\mathrm{p})) \end{bmatrix} \begin{bmatrix} \langle a\rangle \\ \langle {\sigma_1}^-\rangle \\ \vdots \\ \langle {\sigma_N}^-\rangle \end{bmatrix}. \tag{6.2}$$

This model only accounts for both the homogeneous broadening via γ_0 and inhomogeneous broadening via the distribution of the ω_{is}.

The routine we wrote was able to create two different distribution, a Lorentzian and a Gaussian. They were generated by randomly choosing transition frequencies ω_{is} with a Lorentzian or Gaussian shape. Since the tails of a Lorentzian distribution drop off quite slowly $(\propto \omega^{-2})$, a large number of spins N is needed to come close to a continuous distribution. Moreover, the equations quickly become computationally intensive since the matrix scales as $(N + 1 \times N + 1)$.

Nevertheless, the results in Fig. 6.3a,b for $N = 1000$ show already a significant difference

between a Gaussian and a Lorentzian distribution. The parameter values are manually optimized and one can see that due to the much wider tails of the Lorentzian γ_{inh} has to be chosen smaller compared to the Gaussian in order to roughly reproduce the measurement. The value of the other two parameters, κ and g_{col} are again in accordance with the values spectroscopically determined.

Furthermore it is remarkable how the kind of distribution effects the Rabi oscillations, which indicates already the mechanism of cavity protection. Although this model only allowed to compare general differences between a Lorentzian and Gaussian distribution the strong influence of the shape in the dynamics became clearly visible. Since the real distribution is expected to be between a Lorentzian and a Gaussian a model was necessary that allows the parametrisation of the shape.

6.0.4.3. Continous inhomogeneous modelling

The work that will be briefly outlined in the following was done in collaboration with theoreticians [1]. In [Din11] a similar expression for the transmission compared to Eq. 4.42 but with a continuous distribution of the ω_s was derived. If we adapt the used parameters to our convention the following expression can be obtained:

$$\langle a_c \rangle_{\mathrm{st}} = \frac{\mathrm{i}\eta}{\omega_{\mathrm{r}} - \omega_{\mathrm{p}} - \mathrm{i}\kappa - g_{\mathrm{col}}^2 \int \mathrm{d}\omega \frac{\rho(\omega;\omega_{\mathrm{s}},\gamma_{\mathrm{inh}})}{\omega - \omega_{\mathrm{p}} - \mathrm{i}\frac{\gamma_0}{2}}}. \tag{6.3}$$

Now the crucial point is to find the distribution $\rho(\omega;\omega_{\mathrm{s}},\gamma_{\mathrm{inh}})$.

A suitable distribution is the q-Gaussian

$$\rho_q(\omega) = A\left[1 - (1-q)\frac{(\omega-\omega_s)^2}{\Delta^2}\right]^{\frac{1}{1-q}}. \tag{6.4}$$

A is the normalisation factor, Δ is related to the width (FWHM) $\gamma_q = 2\Delta\sqrt{\frac{2^q-2}{2q-2}}$ and q is a Parameter ranging from 0 to 2 which describes the shape of the distribution. For $q \to 1$ the q-Gaussian distribution becomes a pure Gaussian whereas for $q = 2$ the distribution is a pure Lorentzian. Thus the q defines how fast the tails of the distribution fall off.

Finally the problem was described with the help of the Voltera integral equation:

$$\tilde{A}(t) = \int_0^t \mathrm{d}\tau \mathcal{K}(t-\tau)\tilde{A}(\tau) + \mathcal{F}(t). \tag{6.5}$$

[1] Dmitry Krimer and Stefan Rotter from the Institute for Theoretical Physics, TU Wien

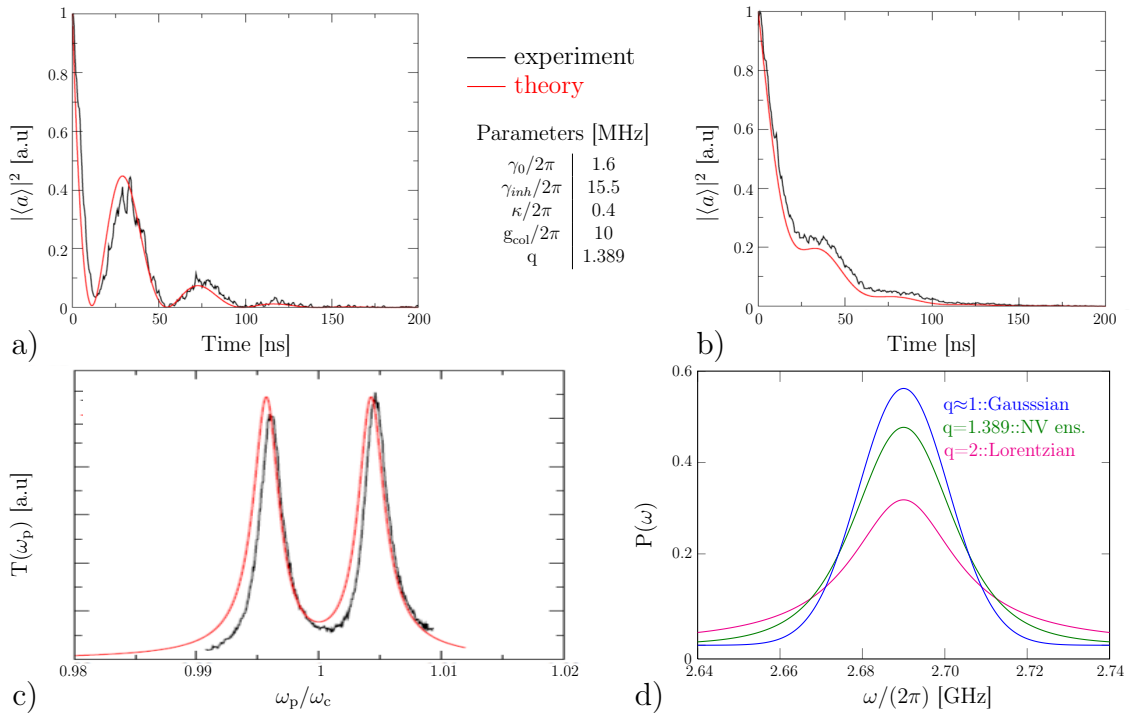

Figure 6.4.: The Figs. show that the approach based on Eq. 6.5 allowed to reproduce the main features of the traces quite well. (a) $\omega_p = \omega_r$. (b) $\omega_p = \omega_+$. (c) Shows the Rabi peaks by a scan of ω_p. (d) Compares the shape that corresponds to the spin distribution according to the results of the fit ($q = 1.39$) with a Lorentzian and a Gaussian.

In a lengthy derivation one can find the Kernel function $\mathcal{K}(t)$ and the initial conditions $\mathcal{F}(t)$. With that Eq. 6.5 can be solved numerically.

The crucial parameters as q, $\gamma_q(\gamma_{\text{inh}})$, γ_0, κ, g_{col} where chosen within a „hybrid“ ansatz, using both spectroscopic and time dependent measurements. From the results shown in Fig. 6.4 one can see the characteristics of both the time domain data and the frequency domain data are well reproduced. It has to be clarified up to what extent the deviations are due to not considered physics (e.g coupling to surrounding nuclei ...) or just due to finite but improvable accuracy of the measurement conditions. The large inhomogeneous broadening $\gamma_{\text{inh}} = 2\pi \times 15.0\,\text{MHz}$ has already emerged from the previous models. κ remained equal while g_{col} slightly decreased. With a q-factor of 1.389 the decay of the spin

distribution is clearly faster than ω^{-2} which implies that the effect of cavity protection could in principle be used.

Finally parametrisation of the results lead to a critical photon number $n_0 = 0.3$ and a cooperativity $C = 16.1$. To conclude, the strong coupling regime was reached primarily due to the relative small loss rate of the resonator compared to the NV^- ensemble.

7. Conclusion

From an experimental point of view this thesis covers the resonator response to a perpendicular magnetic field on the one hand and phenomena related to the strong coupling of a spin-system to an electromagnetic field of a resonator on the other hand. The analysis in turn is focused mainly on the linewidth and lineshape of the inhomogeneously broadened spin distribution.
In the following a short conclusion with respect to these issues will be given.

Perpendicular external magnetic fields The main task of the external magnetic fields in our experimental set-up was the tuning of the ESR frequency of the NV^- ensemble, in short: They controlled the detuning between the resonator and the NV^- ensemble. In this thesis it is shown that perpendicular external magnetic fields in particular, not only effects the ESR frequency of the NV^- ensemble, but also some properties of the resonators. It was found that half wave resonators are very sensitive with respect to perpendicular magnetic fields. In contrast it turned out that LER are quite robust in this regard or rather that any effects caused by external magnetic fields are negligible for our purposes.
This means that a LER is a suitable resonator type for experiments where the direction of the magnetic field contains perpendicular components with respect to the resonator chip surface. On the contrary, this has to be avoided in experiments that include the usage of half wave resonators which implies an adequate alignment between the resonator and the magnetic coils.

Strong coupling regime With both resonator types, a half wave and a LER the strong coupling regime was reached. In the case of a LER it was the first time at all that an

experiment in the strong coupling regime was carried out. This was an important step, since a LER provides in principle the possibility to reduce inhomogeneous broadening of the NV^- ensemble simply by coupling to less spins due to a reducible mode volume.
The strong coupling of a LER to a NV^- ensemble was measured so far only spectroscopically. Systematic measurements with different mode volumes and the same diamond have not yet been carried out so that the effect of reduced inhomogeneous broadening due to a reduced resonator mode volume experimentally remains unconfirmed.
Measuring strong coupling phenomena in the time domain opened up the field of pulsed measurements. For the first time domain experiments, that are shown in this thesis, a well proven combination of resonator (half wave) and diamond were used. It turned out that the inhomogeneous broadening is limiting the coherent exchange of excitations to just a few cycles.
To tackle this problem one either can use diamonds with NV^- ensembles that are less broadened or (and) use resonators that allow to couple to a reduced ensemble. Alternatively, one could make use of microwave techniques to pump parts of the broadened spin ensemble into long-living excited states in order to prevent their availability for the real experiment.
Finally, it will be interesting to find out to what extend a LER can solve the problem of too large losses. So far, time domain measurements with a LER remains to be carried out.

Inhomogeneous broadening In [San12] an analysis of data from previous spectroscopic measurements with the same combination of resonator and diamond was carried out. In this paper they found amongst others a value for the linewidth of the inhomogeneous broadened spin ensemble $\gamma_{\mathrm{inh}}/2\pi$ in the order of 12.5 MHz. With the first time domain measurements a new set of data became available that allowed to analyse both, the steady state of the coupled resonator-spin system and its dynamics. With respect to the q-factor that describes the shape of the spin distribution the recent „two channel“ analysis and the spectroscopically based analysis in [San12] show the same value, namely $q = 1.389$. Both analysis are in good agreement with respect to the collective coupling strength g_{col}, however, they diverge considerably with regard to γ_{inh}. The value for γ_{inh} that results

from the analysis in Chap. 6 is in the order of 15.5 MHz. The reason for this may be the fact that in the measurement analysed in this thesis theoretically twice as much single NV^- centres were coupled to the resonator. This in principle may result in a larger inhomogeneous broadening but at the same time also should lead to an enhancement of the collective coupling strength by a factor of $\sqrt{2}$.

An interesting question in the context of good agreement of the q-factors is, to what extend the shape of the distribution depends on the number of spins in the ensemble? In principle, dipolar interaction with neighbouring spins are the origin of inhomogeneous broadening of NV^- centres ensembles and should lead to a Lorentzian lineshape [Dob08] with a cutoff [Kub12] or rather to a q-factor of 2. A q-factor of 1.389 therefore raises questions concerning contributions to the inhomogeneous broadening apart from dipolar interaction. In [Kub12] a misalignment of the external magnetic field with the crystalline axis and spatial inhomogeneity of the NV^- centres are mentioned as possible origins that can cause contributions to the inhomogeneous broadening. As in our case the resonator is not frequency tunable rather high magnetic fields have to be applied on the diamond in order to couple them resonantly. Instabilities of the external magnetic field that controls the ESR of the NV^- centres could enhances inhomogeneous broadening. Since a spectroscopic measurement for a fixed magnetic field can take up to 153 s or even much longer in time domain measurements with a large number of averages, it was important to investigate the stability of the magnetic field within this time-scale. We found out that neither a drift nor fluctuations of the magnetic field were in a range that could have been a considerably origin of the large decay rate of the spin ensemble.

To conclude, even though values are found that can describe the shape of the inhomogeneously broadened distribution a qualitative understanding is not yet reached.

For a successful implementation of a hybrid based quantum circuit a superconducting qubit is missing (already arrived and is waiting to be incorporated) and the obstacle of inhomogeneous broadening has to be reduced at all to an acceptable level.

A. Matrix description of a network

The characteristics of an electrical circuit can be described by means of the scattering matrix **S**. The advantage of the scattering matrix is the direct combination of the incoming with the out-coming amplitudes of a device. The indices of the elements of the

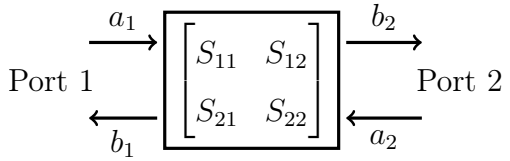

$$\begin{bmatrix} b_1 \\ b_2 \end{bmatrix} = \begin{bmatrix} S_{11} & S_{12} \\ S_{21} & S_{22} \end{bmatrix} \begin{bmatrix} a_1 \\ a_2 \end{bmatrix}$$

Figure A.1.: Figure shows how the amplitudes of a two port device are related to the elements of the scattering matrix.

scattering matrix S_{ij} are consistent with the ports of a measurement device e.g. a Vector Network Analyzer (VNA), where the first index refers to the port where the signal is detected whereas the second index refers to the port where the signal is leaving the device. Working with a two-port device, reflexivity is described by the diagonal elements S_{11} and S_{22} and transmission by the off-diagonal elements S_{12} and S_{21}. S_{11} for example describes that the stimulus port as well as the detection port are taken to be port 1. We are mostly interested in the transmission that is described by the S_{21} matrix element.
If $a_2 = 0$, which also assumes a Z_0 terminated source, the forward transmission ratio becomes $S_{21} = b_2/a_1$. A more general relation is the following [Poz05]

$$S_{ij} = \frac{b_i}{a_j}\Big|_{a_i=0,\, i\neq j}. \tag{A.1}$$

If a network consists of a cascade of electrical circuits then the scattering matrix approach to analyze the network is less convenient. To calculate such an electrical network one usually makes use of the so called ABCD-matrix. Note that A and D are unitless coeffi-

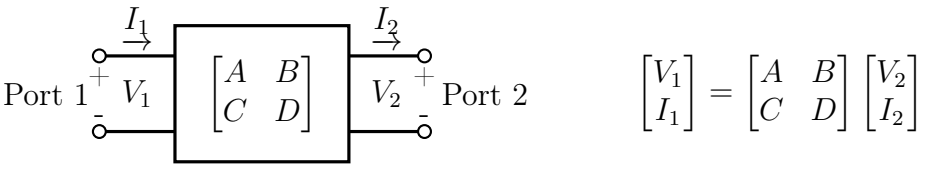

Figure A.2.: Figure shows how the measures of a two port device are related to the elements of the ABCD matrix.

cients, while parameter B has units of impedance and parameter C units of admittance. The ABCD-matrix, unlike the **S** matrix is therefore limited to two port devices.
The main advantage of the transmission matrix is that for N cascaded networks, the total ABCD matrix can be determined as the product of all N networks. Once the total ABCD

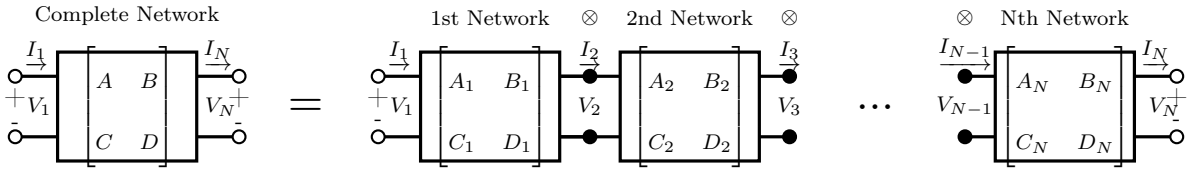

Figure A.3.: Calculation of a network with ABCD matrices.

matrix is calculated the elements of the scattering matrix **S** can be expressed in terms of the elements of the ABCD-matrix. The forward transmission parameter S_{21} from the scattering matrix for example is given by the following expression [Poz05]:

$$S_{21} = \frac{2}{A + B/Z_0 + CZ_0 + D}. \tag{A.2}$$

B. Gallery

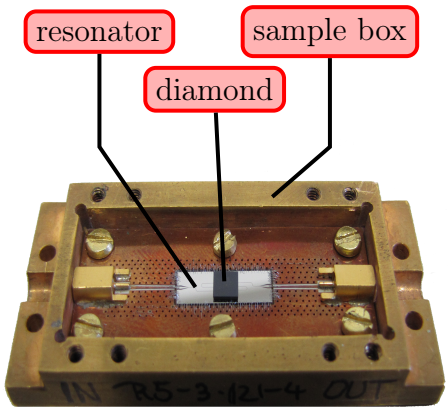

Figure B.1.: The figure shows an opened sample box that contains a resonator with a diamond on top.

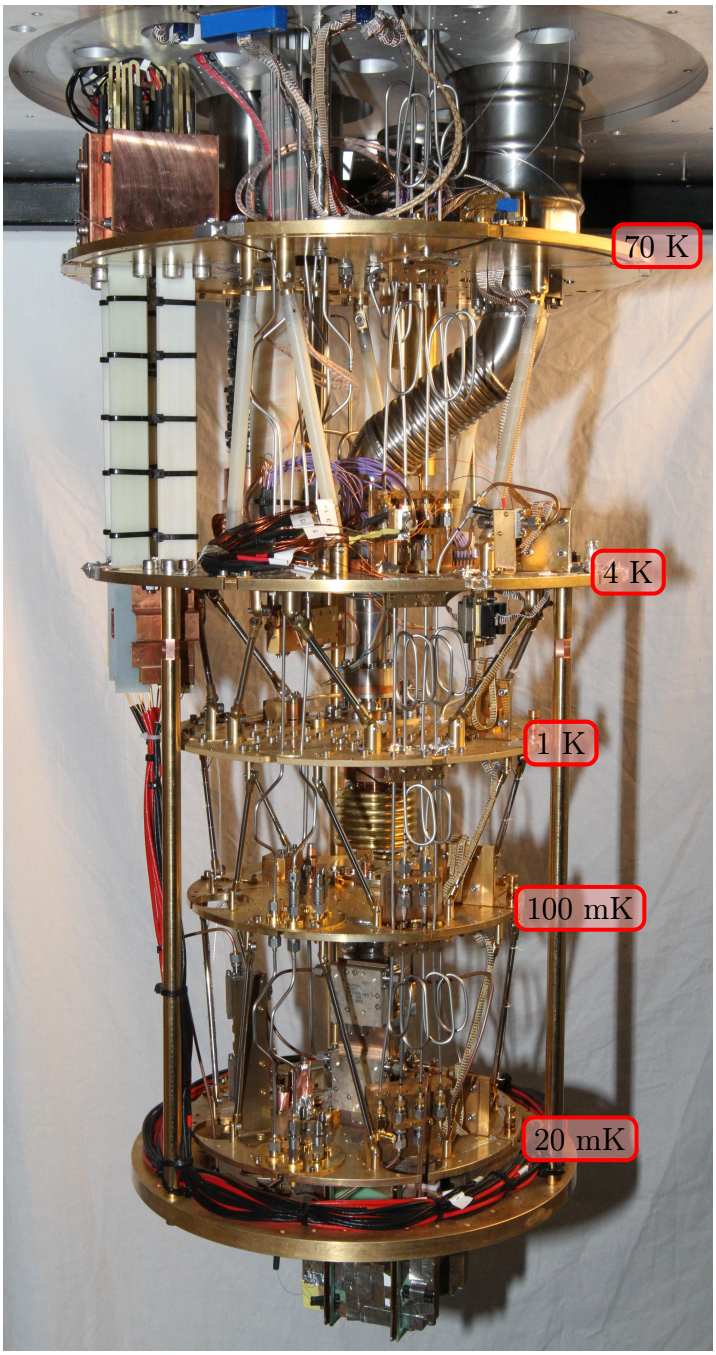

Figure B.2.: The figure shows the five temperature stages of a dilution refrigerator.

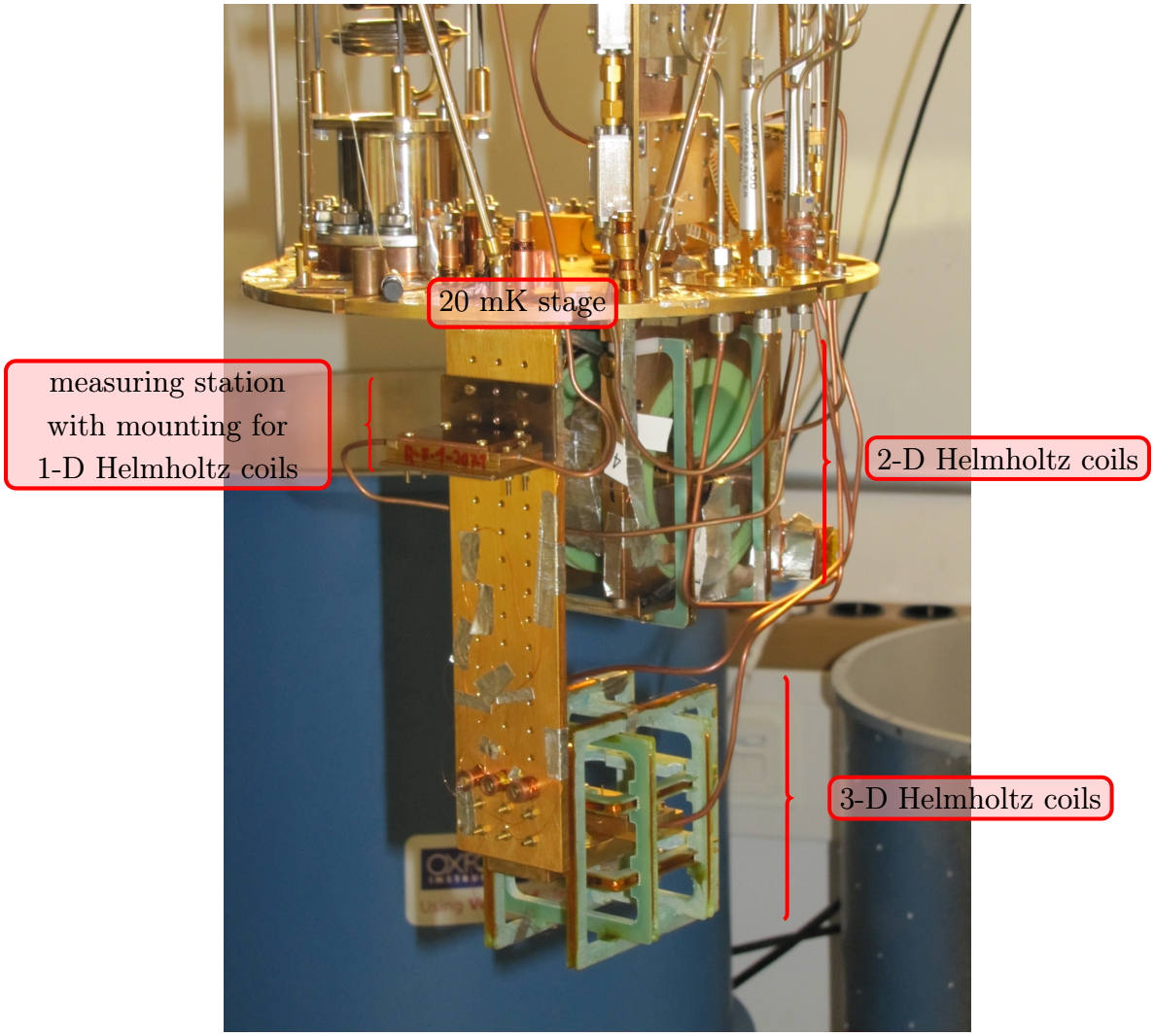

Figure B.3.: The figure shows the three measurement stations that are mounted on the lowest temperature stage of the DR and that allow to apply 1-D, 2-D and 3-D magnetic fields. The 1-D coils were not mounted at the moment when the picture was taken

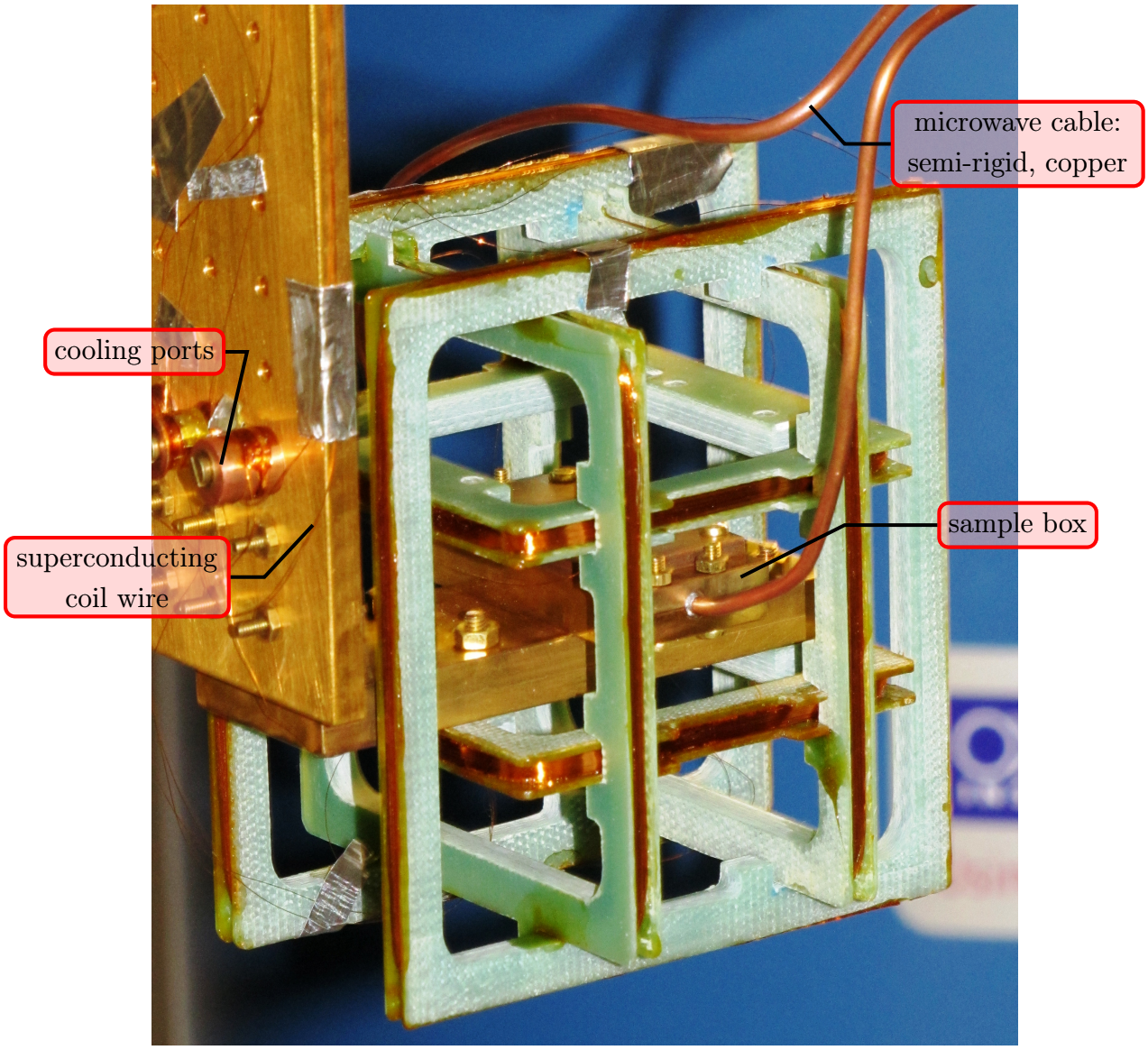

Figure B.4.: The figure shows a closer look at the 3-D Helmholtz coils. In order to cool the superconducting wire of the coils it is wound several times around a port at each temperature stage. In the centre of the 3-D rectangular coils construction one can indicate the sample box that contains the resonator chip on the diamond (see Fig. B.1).

Acknowledgements

„There are men who struggle for a day, and they are good. There are others who struggle for a year, and they are better. There are some who struggle many years, and they are better still. But there are those who struggle all their lives, and these are the indispensable ones.“
-Bertold Brecht
"In Praise of the Fighters", song from the play "The Mother", 1930

In this sense I would like to express my gratitude to the key *quantum fighters* who afford me a very enriching time as a diploma student.
Many thanks to Jörg Schmiedmayer for providing great *quantum schwuantum* in general and for the possibility to have carried out the diploma thesis at hand in particular.
The experiments that are covered by this thesis were based on the hard work of several *heroes next door*:
First of all I would like to thank (Jo)Hannes for introducing me into the/his *world of 50* Ω and for supervising my work in the laboratory.
The operator on site or rather in the laboratory was Robert, a man who does not hesitate to become one with the measurement apparatus and whom I owe a lot or rather to be more precise, almost everything.
Christian, *le créateur* of a vast number of excellent microwave resonators was ready at any time to share his far reaching experiences that helped a lot to gain an overview of the subject matter.
Stefan's recommendations with respect to the documentation tools have made my life much more easier.
Many special thanks to Stefan Rotter and Dmitry Krimer who really helped us a lot to analyse our measurement results and to get the best out of the data.

Bibliography

[Ber07] B. et al Bertaina. „Rare-earth solid-state qubits“. In: *Nature Nanotechnology 2* (2007). DOI: 10.1038/nnano.2006.174 (cit. on p. 3).

[Ams11] Amsuess, R. and Koller, Ch. et al. „Cavity QED with magnetically Coupled Collective Spin States“. In: *PRL* (2011). DOI: {10.1103/PhysRevLett.107.060502} (cit. on pp. 44, 58).

[Bat08] Batalov, A. and Zierl, C. and F. Jelezko and J. Wrachtrup. „Temporal Coherence of Photons Emitted by Single Nitrogen-Vacancy Defect Centers in Diamond Using Optical Rabi-Oscillations“. In: *PRL* (2008). DOI: 10.1103/PhysRevLett.100.077401 (cit. on p. 26).

[Ber82] Berestetskii, B. and Lifshitz, E. and Pitaevskii, P. *Quantum Electrodynamics.* Oxford:Pergamon, 1982 (cit. on p. 3).

[Bla04] Blais, Alexandre and Huang, Ren-Shou and Wallraff, Andreas and Girvin, S. and Schoelkopf, R. „Cavity quantum electrodynamics for superconducting electrical circuits: An architecture for quantum computation“. In: *Physical Review A* (2004). DOI: 10.1103/PhysRevA.69.062320 (cit. on p. 4).

[Che97] Chen, E. and Chou, S. „Characteristics of coplanar transmission lines on multilayer substrates: Modeling and experiments“. In: *Microwave Theory and Techniques, IEEE Transactions on 45* (1997) (cit. on p. 14).

[Cor00] Cory, D. and Zurek, W. et al. „NMR Based Quantum Information Processing: Achievements and Prospects“. In: (2000) (cit. on p. 3).

[Deu85] Deutsch, David. „Quantum theory, the Church-Turing principle and the universal quantum computer“. In: *Proceedings of the Royal Society of London A 400, pp. 97-117 (1985)* (1985) (cit. on p. 1).

[Deu92] Deutsch, D. and Josza, R. „Rapid Solutions of problems by quantum computation“. In: *Proceedings: Mathematical and Physical Sciences* (1992) (cit. on p. 2).

[Dev04] Devoret, M. and Wallraff, A. and Martinis, J. „Superconducting Qubits: A Short Review“. In: (2004). DOI: {arXiv:cond-mat/0411174} (cit. on pp. 4 sq., 50).

[DiV96] DiVincenzo, David. „Topics in Quantum Computers“. In: (1996) (cit. on p. 2).

[Din11] Diniz, I. and Portolan, S. and Ferreira, R. and Gérard, J. M. and Bertet, P. and Auffèves, A. „Strongly coupling a cavity to inhomogeneous ensembles of emitters: Potential for long-lived solid-state quantum memories“. In: *Phys. Rev. A* (2011). DOI: 10.1103/PhysRevA.84.063810 (cit. on pp. 44, 79, 83).

[Dob08] Dobrovitski, V. V. and Feiguin, A. E. and Awschalom, D. D. and Hanson, R. „Decoherence dynamics of a single spin versus spin ensemble“. In: *Phys. Rev. B* 77 (2008). DOI: 10.1103/PhysRevB.77.245212 (cit. on p. 88).

[Dol11] Dolde, F. and Jelezko, F. and Wrachtrup, J. „Electric-field sensing using single diamond spins“. In: *Nature Physics 7 459–463* (2011). DOI: 10.1038/nphys1969 (cit. on p. 24).

[Dol13] Dolde, F. and and Wrachtrup, J. et al. „Room-temperature entanglement between single defect spins in diamond“. In: *Nature Physics 9,* (2013). DOI: 10.1038/nphys2545 (cit. on p. 24).

[Doy08] Doyle, S. and Duncombe, C. et al. „Lumped Element Kinetic Inductance Detectors“. In: *J Low Temp Phys* (2008). DOI: 10.1007/s10909-007-9685-2 (cit. on pp. 18, 61).

[Fed11] Fedder, H. and Dolde, F. and Jelezko, F. and Wrachtrup, J. „ Towards T1-limited magnetic resonance imaging using Rabi beats“. In: *Applied Physics B* (2011). DOI: 10.1007/s00340-011-4408-4 (cit. on p. 26).

[Fey82] Feynman, Richard. „Simulating Physics with Computers“. In: *International Journal of Theoretical Physics, VoL 21* (1982) (cit. on p. 1).

[Fin10] Fink, Johannes M. „Quantum Nonlinearities in Strong Coupling Circuit QED“. phdthesis. 2010 (cit. on pp. 20, 65).

[Fox07] Fox, M. *Quantum Optics : An Introduction. 2rd.* Oxford University Press, 2007 (cit. on p. 34).

[Fru05] Frunzio, L. and Wallraff, A. and Schuster, D. and Majer, J. and Schoelkopf, R. „Fabrication and Characterization of Superconducting Circuit QED Devices for Quantum Computation“. In: *IEEE Transactions on Appiled Superconductivity* (2005). DOI: 10.1109/TASC.2005.850084 (cit. on p. 55).

[Gao08] Gao, Jiansong. „The Physics of Superconducting Microwave Resonators“. phdthesis. 2008 (cit. on p. 61).

[Goe08] Goeppl, M. and Fragner, A. and Wallraff, A. et al. „Coplanar Waveguide Resonators for Circuit Quantum Electrodynamics“. In: *Arxiv preprint cond-mat/0* (2008). arXiv:arXiv:0807.4094v1 (cit. on pp. 11, 16, 23, 56).

[Gop09] Gopalakrishnan, B. and Neumann, P. and Fedor Jelezko and Jörg Wrachtrup. „Ultralong spin coherence time in isotopically engineered diamond“. In: *Nature Materials 8, 383 - 387* (2009). DOI: 10.1038/nmat2420 (cit. on p. 25).

[Gri97] Gripp, J. and Mielke, L. and Orozco, L. „Evolution of the vacuum Rabi peaks in a detuned atom-cavity system“. In: *Phys Rev A 56* (1997). DOI: 10.1103/PhysRevA.56.3262. (cit. on p. 64).

[Han06] Hanson, R. and Mendoza, F. M. and Epstein, R. J. and Awschalom, D. D. „Polarization and Readout of Coupled Single Spins in Diamond“. In: *Phys. Rev. Lett.* (2006). DOI: 10.1103/PhysRevLett.97.087601 (cit. on p. 24).

[Han08] Hanson, R. and Awschalom, D. „Coherent manipulation of single spins in semiconductors“. In: *Nature* (2008). DOI: 10.1038/nature07129 (cit. on p. 3).

[Hea08] Healey, J. et al. „Magnetic field tuning of coplanar waveguide resonators “. In: *AIP* (2008). DOI: {10.1063/1.2959824} (cit. on pp. 55, 57).

[Hon69] Hone, D. and Jaccarino, V. and Ngwe, Tin and Pincus, P. „Microscopic Inhomogeneous Broadening and Nuclear Spin-Spin Interactions“. In: *Phys. Rev.* 186 (1969). DOI: 10.1103/PhysRev.186.291 (cit. on p. 78).

[Jay63] Jaynes, E.T. and Cummings F. W. „Comparison of quantum and semiclassical radiation theories with application to the beam maser“. In: *Proc. IEEE 51* (1963). DOI: 10.1109/PROC.1963.1664. (cit. on p. 34).

[Jel06] Jelezko, F. and Wrachtrup,J. „Single defect in diamond: A review“. In: (2006). DOI: 10.1002/pssa.200671403 (cit. on pp. 24, 44).

[Kim98] Kimble, H.J. „ Strong interactions of single atoms and photons in cavity QED “. In: *Physics Scripta T76* (1998). DOI: doi:10.1238/Physica.Topical.076a00127 (cit. on p. 45).

[Kol12] Koller, Christian. „Towards the experimental realization of Hybrid Quantum Systems“. phdthesis. 2012 (cit. on pp. 18, 22 sq., 55, 63).

[Kub10] Kubo, Y. and Ong, F. R. and Esteve, D. „Strong Coupling of a Spin Ensemble to a Superconducting Resonator“. In: *Phys. Rev. Lett.* (2010). DOI: {10.1103/PhysRevLett.105.140502} (cit. on pp. 24, 41, 43, 58 sq.).

[Kub12] Kubo, Y. and Diniz, I. and Esteve, D. and Bertet, P. „Storage and retrieval of a microwave field in a spin ensemble“. In: *Phys. Rev. A* (2012). DOI: 10.1103/PhysRevA.85.012333 (cit. on pp. 73, 88).

[Kur11] Kurucz, Z. and Wesenberg, J.H. and Mølmer, K. „Spectroscopic properties of inhomogeneously broadened spin ensembles in a cavity“. In: *Physical Review A* (2011) (cit. on pp. 43 sq., 79).

[Los98] Loss, D. and DiVincenzo, D. „Quantum computation with quantum dots“. In: *Phys. Rev. A* (1998). DOI: 10.1103/PhysRevA.57.120 (cit. on p. 3).

[Mab02] Mabuchi, H. and Doherty, A. „Cavity Quantum Electrodynamics: Coherence in Context“. In: *Science* (2002). DOI: 10.1126/science.1078446 (cit. on p. 3).

[Maj07] Majer, J. and Chow, J. M. and Devoret, M. H. and Girvin, S. M. and Schoelkopf, R. J. et al. „Coupling Superconducting Qubits via a Cavity Bus“. In: *Nature 449* (2007). DOI: 10.1038/nature06184 (cit. on p. 7).

[Mar04] Martinis, J. and Devoret, M. „Implementing Qubits with Superconducting Integrated Circuits“. In: *Quantum Information Processing* (2004). DOI: 10.1007/s11128-004-3101-5 (cit. on p. 3).

[Mil05] Miller, R. and Kimble, H. et al. „Trapped atoms in cavity QED: coupling quantized light and matter“. In: *J. Phys. B:At.Mol.Opt.Phys. 38* (2005). DOI: 10.1088/0953-4075/38/9/007 (cit. on pp. 4, 7).

[Mon02] Monroe, C. „Quantum information processing with atoms and photons“. In: *Nature, Vol 416* (2002) (cit. on p. 3).

[Moo65] Moore, G. „Cramming more components onto integrated circuits“. In: *Electronics, Volume 38* (1965) (cit. on p. 1).

[Nie07] Nielsen, M. and Chuang, I. *Quantum Computation and Quantum Information.* Cambrindge University Press, 2007 (cit. on pp. 1 sq.).

[Ors07] Orszag, Miguel. *Quantum Optics,2nd Edition.* Springer, 2007 (cit. on pp. 21 sq., 35 sqq.).

[Pai11] Paik, H. and Schuster, D. I. and Devoret, M. H. and Schoelkopf, R. J. „Observation of High Coherence in Josephson Junction Qubits Measured in a Three-Dimensional Circuit QED Architecture“. In: *Phys. Rev. Lett.* (2011). DOI: 10.1103/PhysRevLett.107.240501 (cit. on pp. 4, 25).

[Poz05] Pozar, David. *Microwave Engineering. 3rd.* Wiley, 2005 (cit. on pp. 8, 14 sqq., 89 sq.).

[Rab06] Rabl, P and Schoelkopf, R. and Zoller, P. „Hybrid Quantum Processors: Molecular Ensembles as QuantumMemory for Solid State Circuits“. In: *Phys. Rev. Lett. 97* (2006). DOI: 10.1103/PhysRevLett.97.033003 (cit. on p. 5).

[Roo04] Roos, F. and Blatt, R. et al. „Bell States of Atoms with Ultralong Lifetimes and Their Tomographic State Analysis“. In: *Phys. Rev. Lett. 92* (2004). DOI: 10.1103/PhysRevLett.92.220402 (cit. on p. 5).

[San12] Sandner, K. and Ritsch, H. and Amsüss, R. and Koller, Ch. and Nöbauer, T. and Putz, S. and Schmiedmayer, J. and Majer, J. „Strong magnetic coupling of an inhomogeneous nitrogen-vacancy ensemble to a cavity“. In: *Phys. Rev. A* (2012). DOI: 10.1103/PhysRevA.85.053806 (cit. on pp. 44, 46, 73, 87).

[Sch07] Schuster, David Isaac. „Circuit Quantum Electrodynamics“. phdthesis. 2007 (cit. on p. 3).

[Sch08] Schaefer, Clemens and Bergman, Ludwig. *Mechanik, Akustik, Wärme.* Walter De Gruyter, 2008 (cit. on p. 31).

[Ven08] Ventura, Guglielmo and Risegari, Lara. *The Art of Cryogenics.* Elsevier, 2008 (cit. on p. 50).

[Wal04] Wallraff, A. and Schuster, J. and Schoelkopf, R. et al. „Strong coupling of a single photon to a superconducting qubit using circuit quantum electrodynamics“. In: *Nature* (2004). DOI: 10.1038/nature02831.1. (cit. on p. 5).

[Web10] Weber, J.R. and Awschalom, D.D. „Quantum computing with defects“. In: *PNAS* 107 (2010). DOI: 10.1073/pnas.1004033107 (cit. on p. 27).

[Wes09] Wesenberg, J. H. and Ardavan, A. and Briggs, G. A. D. and Morton, J. and Schoelkopf, R. J. and Schuster, D. I. and Mølmer, K. „Quantum Computing with an Electron Spin Ensemble“. In: *Phys. Rev. Lett.* 103 (2009). DOI: 10.1103/PhysRevLett.103.070502 (cit. on p. 40).

[Wra06] Wrachtrup,.J. and Jelezko, F. „Processing quantum information in diamond“. In: *J. Phys.: Condens. Matter 18 (2006) S807–S824* (2006). DOI: 10.1088/0953-8984/18/21/S08 (cit. on p. 26).

[Wyk97] Wyk van, J. et al. „The dependences of ESR line widths and spin - spin relaxation times of single nitrogen defects on the concentration of nitrogen defects in diamond“. In: *J.Phys D, 30* (1997). DOI: 10.1088/0022-3727/30/12/016 (cit. on p. 27).

[Yip92] Yip, S. K. and Sauls, J. A. „Nonlinear Meissner effect in CuO superconductors“. In: *Phys. Rev. Lett.* (1992). DOI: 10.1103/PhysRevLett.69.2264 (cit. on p. 56).

[Yos96] Yoshimi Mita. „Change of absorption spectra in type-1b diamond with heavy neutron irradiation“. In: *Physical Review B* (1996) (cit. on p. 29).